Air Force Institute of Technology
AFIT Scholar

3-22-2012

LADAR Performance Simulations with a High Spectral Resolution Atmospheric Transmittance and Radiance Model- LEEDR

Benjamin D. Roth

Follow this and additional works at: https://scholar.afit.edu/etd

Part of the Atmospheric Sciences Commons, and the Electromagnetics and Photonics Commons

Recommended Citation

LADAR PERFORMANCE SIMULATIONS WITH A HIGH SPECTRAL

RESOLUTION ATMOSPHERIC TRANSMITTANCE AND RADIANCE

MODEL- LEEDR

THESIS

Benjamin D. Roth, Captain, USAF

AFIT/APPLPHY/ENP/12-M09

DEPARTMENT OF THE AIR FORCE
AIR UNIVERSITY

AIR FORCE INSTITUTE OF TECHNOLOGY

Wright-Patterson Air Force Base, Ohio

AFIT/APPLPHYS/ENP/12-M09

LADAR PERFORMANCE SIMULATIONS WITH A HIGH SPECTRAL

RESOLUTION ATMOSPHERIC TRANSMITTANCE AND RADIANCE

MODEL- LEEDR

THESIS

Presented to the Faculty

Department of Engineering Physics

Graduate School of Engineering and Management

Air Force Institute of Technology

Air University

Air Education and Training Command

In Partial Fulfillment of the Requirements for the

Degree of Master of Science in Applied Physics

Benjamin D. Roth, BS

Captain, USAF

March 2012

AFIT/ APPLPHYS /ENP/12-M09

LADAR PERFORMANCE SIMULATIONS WITH A HIGH SPECTRAL

RESOLUTION ATMOSPHERIC TRANSMITTANCE AND RADIANCE

MODEL- LEEDR

Benjamin D. Roth, BS
Captain, USAF

Approved:

_____   _____
Steven T. Fiorino, PhD (Chairman)   Date

_____   _____
Michael A. Marciniak, PhD (Member)   Date

_____   _____
Kevin C. Gross, PhD (Member)   Date

_____   _____
Paul F. McManamon, PhD (Member)   Date

Abstract

In this study of atmospheric effects on Geiger Mode laser ranging and detection (LADAR), the parameter space is explored primarily using the Air Force Institute of Technology Center for Directed Energy's (AFIT/CDE) Laser Environmental Effects Definition and Reference (LEEDR) code. The expected performance of LADAR systems is assessed at operationally representative wavelengths of 1.064, 1.56 and 2.039 µm at a number of locations worldwide. Signal attenuation and background noise are characterized using LEEDR. These results are compared to standard atmosphere and Fast Atmospheric Signature Code (FASCODE) assessments. Scenarios evaluated are based on air-to-ground engagements including both down looking oblique and vertical geometries in which anticipated clear air aerosols are expected to occur. Engagement geometry variations are considered to determine optimum employment techniques to exploit or defeat the environmental conditions. Results, presented primarily in the form of worldwide plots of notional signal to noise ratios, show a significant climate dependence, but large variances between climatological and standard atmosphere assessments. An overall average absolute mean difference ratio of 1.03 is found when climatological signal-to-noise ratios at 40 locations are compared to their equivalent standard atmosphere assessment. Atmospheric transmission is shown to not always correlate with signal-to-noise ratios between different atmosphere profiles. Allowing aerosols to swell with relative humidity proves to be significant especially for up looking geometries reducing the signal-to-noise ratio several orders of magnitude. Turbulence blurring effects that impact tracking and imaging show that the LADAR system has little capability at a 50km range yet the turbulence has little impact at a 3km range.

Acknowledgments

I would like to express my appreciation to my faculty advisor, Dr. Steven Fiorino, for his guidance, support and enthusiasm. He provided guidance at crucial periods during this effort. I would also like to thank my committee members Dr. Michael Marciniak, Dr. Kevin Gross, and Dr. Paul McManamon who provided invaluable feedback. A non-committee advisor, Dr. Jack McCrae joined AFIT and began to assist me at the most critical point in my thesis effort. His invaluable knowledge and expertise in atmospheric science and LADAR technologies was greatly appreciated. I am grateful for the help received from my fellow physics peers. I would also like to thank Mr. Robin Ritter from Tau Technologies, and Mr. Douglas Jameson from the Air Force Research Laboratory for answering my myriad of emails.

I am grateful to my father for teaching me the importance of an enduring work ethic. His faith in me has instilled a knowledge that I can accomplish anything I set my mind to. I am indebted to my mother, whose endless love and service has made my life possible. Most of all, I am especially grateful for the love and patience of my wife who sustained me with a positive attitude through the late nights and stressful moments. May every moment together be cherished as we experience life together as a family.

Benjamin D. Roth

Table of Contents

List of Figures

List of Tables

LADAR PERFORMANCE SIMULATIONS WITH A HIGH SPECTRAL

RESOLUTION ATMOSPHERIC TRANSMITTANCE AND RADIANCE

MODEL- LEEDR

I   Introduction

1.1   Background

LADAR (Laser Detection and Ranging) systems use the same basic principle of
transmitting and receiving electromagnetic energy of that of RADAR (Radio Detection
and Ranging). The major difference between these systems is that they operate at
different wavelengths. While LADAR is unable to provide the wide area surveillance
which RADAR offers, LADAR signals return much more information because of their
small wavelengths. Radar image resolution is proportional to the frequency and in fact,
3D images can be produced at LADAR wavelengths. The application of LADAR
systems is a growing area of research with current and proposed uses ranging from
robotic vehicle maneuvering to identifying re-entry vehicles for missile defense (Kenyon
2002). The Air Force has a vested interest in this technology because of LADAR's
unique capabilities and implications for Information Surveillance and Reconnaissance
(ISR) missions.

Every system has capabilities and limitations; exploiting those capabilities while
minimizing the limitations is the primary goal of current LADAR system performance
computer modeling efforts. Operational capability of these systems is largely dependent

upon propagation through the atmosphere and atmospheric noise sources. Being able to accurately model atmospheric effects and the resulting signal-to-noise ratio is paramount in understanding LADAR capabilities as well as identifying areas of further research.

Atmosphere Transmittance studies have routinely been done using Fast Atmospheric Signature Code (FASCODE) which can incorporate standard and homogeneous atmosphere profiles. A unique atmosphere propagation and characterization package called the Laser Environmental Effects Definition and Reference (LEEDR) has been developed by the Air Force Institute of Technology, Center for Directed Energy (AFIT/CDE) as part of the High Energy Laser End-to-End Operational Simulation (HELEEOS) model. LEEDR is a more up-to-date line-by-line simulation with more realistic atmosphere profiles. The uniqueness of the LEEDR model is that it incorporates a correlated, probabilistic climatological database that creates realistic atmosphere profiles (Fiorino *et al.* 2008). Throughout this study, "LEEDR profiles" refers to atmospheric profiles created within LEEDR at the Extreme and Percentile Environmental Reference Tables (ExPERT) sites. Historical weather data from these locations are used to build the unique atmosphere profiles in LEEDR.

Accurately characterizing conditions within the atmosphere and the effects on electromagnetic radiation is a very difficult and complex problem. Within the atmosphere, aerosols, molecular composition, hydrometeors, and optical turbulence all cause a reduction in LADAR performance. The absorption and scattering due to molecules and particulates, also known as extinction, causes a reduction in transmittance. Because of the importance in maintaining wave geometry to receive high resolution

2

information on LADAR systems, optical turbulence is also of great concern. Turbulence often distorts a propagating wave and causes signal processing problems.

Over simplifying the dynamical atmosphere environment when trying to model its effects on signal propagation will lead to incorrect solutions. Accurately modeling LADAR atmospheric propagation and the resulting signal-to-noise allows researchers and developers to establish future program requirements and ultimately produce systems that pass testing and evaluation standards.

1.2 Problem Statement

If the current developers of LADAR systems do not accurately model atmospheric effects on signal propagation, future advances of this technology will be greatly hindered if not all together halted. Atmospheric properties that correlate to attenuation of electromagnetic waves include temperature, pressure, water vapor, optical turbulence, aerosols, and hydrometeors. Atmosphere conditions can sometimes cause severe attenuation making LADAR signals operationally useless.

The scientific community still relies on legacy programs such as the FASCODE in PLEXUS that are not maintained and contain an outdated High-Resolution Transmission molecular Absorption (HITRAN) database. These programs are typically used with standard and homogeneous atmosphere profiles that ignore critical features that may have large effects on LADAR wavelength transmission. One of the key atmospheric features that is ignored in these legacy programs is the enlarging of aerosols at the top of the boundary layer due to an increase in relative humidity. More realistic atmospheric profiles are needed to accurately account for this haze layer. Also, the contribution of

other atmosphere properties on attenuation must be accurately accounted for such as molecular composition, optical turbulence, precipitation, and clouds.

1.3 Purpose

The objective of this research is to quantify the advantages of using a probabilistic atmosphere over a standard atmosphere profile when simulating LADAR signal-to-noise ratios. By incorporating a more comprehensive atmospheric propagation program model, future simulation tests on systems in development will have a higher fidelity level. An assessment of the differences in modeling LADAR propagation with the LEEDR model versus legacy systems such as FASCODE is accomplished. The assessment is limited by the correctness of the models used; validating the models is beyond the scope of this project. Instead, a difference between the models will indicate the overall effect specific factors in the atmosphere will have on propagation.

1.4 Hypothesis

The central research question for this work is "Can LEEDR help model more realistic LADAR signal-to-noise calculations?" In order to answer this question, current methods for modeling signal-to-noise must be evaluated, and LEEDR must be merged into these methods. LEEDR contains a more sophisticated boundary layer profile along with other environmental effects that are neglected by other atmospheric models. Whether LEEDR would have a substantial impact on LADAR performance simulations can be determined by quantifying the significance of including these environmental effects. Ratios of signal-to-noise will be compared and quantified using LEEDR at the ExPERT sites and FASCODE with specified atmospheric conditions. It is believed that

4

LEEDR will characterize LADAR signal-to-noise more precisely while legacy programs that use standard profiles will give overly optimistic values. Also, it is believed that this study will demonstrate LEEDR's ability to characterize a much wider range of atmospheric conditions and that it is overall a better, more realistic atmospheric effects model.

1.5   Approach

A comparison of LADAR performance produced by standard atmosphere profiles verses the correlated, probabilistic climatological profiles from LEEDR at the specified LADAR wavelength lines, 1.0642, 1.56, and 2.039 µm display the added fidelity in accounting for specific atmosphere features. A variety of scenarios including look angles, and climate conditions are tested to develop an understanding of the conditions standard atmosphere profiles become ineffective. A short 3 km range at 1530 m altitude and a long 50 km range at 10 km altitude are examined. The vertical engagements at these altitudes are also investigated. The upward looking geometries are also characterized with the High Energy Laser End-to-End Model (HELSEEM) producing signal-to-noise ratio images of a small remote piloted aircraft (RPA). Turbulence effects for both the short and long range scenarios are demonstrated on these images. All scenarios for this research are for the 50th humidity percentile and clear sky conditions. From past research, it is known that LADAR has little capability through clouds and rain. Also, it is expected that the more accurate LEEDR profiles will display properties of the different wavelengths that can be exploited to achieve better propagation.

In order to demonstrate the value in using an up-to-date radiation transfer model, a comparison of transmittance and signal-to-noise ratio calculations from LEEDR,

standard atmosphere, and FASCODE is accomplished. Only the Geiger Mode single pulse LADAR system is evaluated. Similar assessments could be done for various LADAR systems. With such a comparison, it is expected that the need to switch to an industry standard of modeling LADAR propagation with LEEDR or LEEDR-type software that is based on probabilistic atmosphere profiles will be apparent.

A characterization of background noise radiation is vital in this study in order to predict a signal-to-noise ratio. Background noise often "clutters" the sensor making it difficult to process LADAR data. LEEDR is used to model background noise by analyzing the transfer of background radiation over a small spectral band around the laser wavelength. Any photons that do not originate from the reflection of laser light off the target are noise for a Geiger Mode LADAR system. Three sources of noise are considered in this study, the laser scatter, sun scatter, sun reflection, and blackbody radiation.

The approach taken in this study will lead directly to future work. LEEDR produced atmospheres can be fed into more advanced LADAR models used by the Air Force Research Laboratory (AFRL) or other organizations to characterize the signal-to-noise ratio in both Designator and CW class systems. Restricting the study to simulation displayed aspects that are captured by a more sophisticated model. However, knowledge of the accuracy of a computer model is vital given the need to characterize real world scenarios. This thesis sets up model simulations needed for future experimental data comparisons. The physics within a radiative transfer model can be advanced with simple model comparisons, but without real data to analyze, the model accuracy in

characterizing real world systems is unknown. Only through real data analysis can we determine the advantages of a more complex model such as LEEDR.

1.6   Implications

Results of this study quantified the differences on LADAR propagation modeling using standard atmosphere profiles verses using a climatological radiative transfer model. Quantifying the advantages of using probabilistic climatological radiative transfer software to simulate LADAR propagation will give users more confidence in implementing this technology. Researchers will be able to test system capability for an array of applications. Currently, the capabilities of LADAR systems for use in ranging and targeting are largely unknown. With higher fidelity in characterizing the systems signal propagation in different atmospheric conditions, limitations and advantages can be realized and system development will proceed at a quicker rate. With simulation, accurate experiments can be done at the fraction of the cost enabling program managers and the acquisition work force to develop realistic program requirements that will enable LADAR systems to become operational. Models are also a preliminary tool used by test and evaluators, and with more accuracy, computer simulations can save time and money that would otherwise be spent on failed field tests. With the advantages of high resolution 3D imaging, covert surveillance, and near exact ranging, LADAR systems will give the United States military a great advantage over traditional RADAR.

1.7   Outline

Chapter two of this paper discusses the atmosphere effects on laser propagation and specifically the effects on LADAR signals. An overview of how LADAR systems

operate is given. A summary of the LEEDR and FASCODE software packages is also included. Chapter three gives a detailed account of the approach taken and specific steps to model LADAR performance. An overview of the tools used and prior work done using these tools will be included. Chapter four contains the analysis and charts that display what was accomplished and the significance of the thesis. Chapter five is the conclusion, highlighting what was and was not successful in the project along with ideas for future development.

II   Literature Review

2.1   Chapter Overview

The purpose of this chapter is to summarize the relevant science and past research in the current literature that pertains to modeling LADAR propagation through the atmosphere. A synopsis of the atmosphere, its components and characteristics that affect laser propagation, is discussed. Next, an overview of LADAR systems and how they operate is presented. An overview of the LEEDR and the FASECODE model is shown. Finally, some relevant research concludes the literature review.

2.2   Relevant Science

2.2.1   Atmospheric Effects

The lower atmosphere structure can be broken into two pieces: the Troposphere and Stratosphere. The Troposphere extends from Earth's surface to a vertical height between 8 and 14.5 km. The Stratosphere extends above the Troposphere to an altitude of 50 km. In the Troposphere, temperature decreases near linearly with altitude to about - 52 degrees Celsius and then in the Stratosphere increases slowly to -3 degrees Celsius because of ultraviolet radiation absorption. The boundary layer is the region of the Troposphere from the ground to about 2 km where the air is well mixed. This region is characterized by the interaction of the surface and airflows. The water vapor mixing ratio, aerosol number concentration, and potential temperature (the temperature that a parcel of air would have if it is brought dry adiabatically to a pressure of 1000 hPa) are nearly constant. Because of the decrease in pressure with altitude, temperature and temperature dew point (temperature at which condensation occurs) are allowed to vary at different rates. The lowest 50 m of the boundary layer is called the surface layer and

experiences extreme instability. Each of these layers contains molecules and particles that effect the propagation of electromagnetic radiation. Water and carbon dioxide have the largest molecular effect in the LADAR wavelengths. Hydrometeor particles (ice and water droplets) along with aerosols, especially water soluble aerosols, greatly degrade LADAR signals. Because of the different molecular and particle concentrations as well as turbulence properties, each atmospheric layer possesses different radiation attenuation characteristics (Perram *et al.* 2010).

Laser propagation is affected by absorption, scattering, and turbulence in the atmosphere, all being wavelength dependent. Extinction is the sum of the attenuation due to absorption and scattering. Even in clear, cloudless conditions, propagation is degraded by the molecular and aerosol content of the atmosphere. Water vapor is the single most significant absorber in the atmosphere, followed by carbon dioxide, ozone and oxygen. Absorption is the capturing of electromagnetic radiation at a higher wavelength and reemitting it at a lower wavelength. The wavelength dependence on transmittance for the cloud and aerosol free atmosphere is shown in Figure 1. (Perram *et al.* 2010).
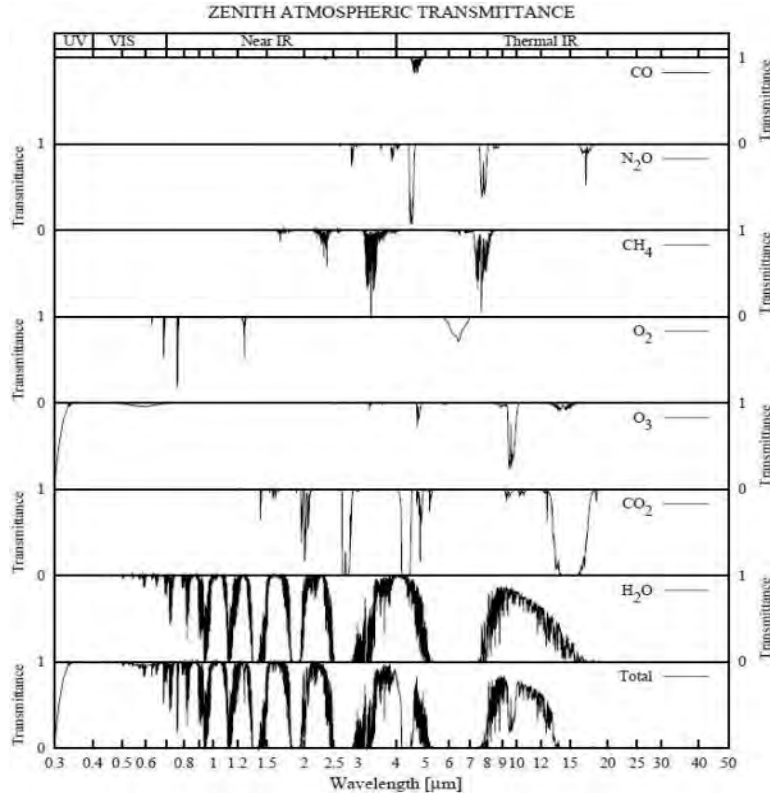
Figure 1. Transmittance due to top molecular absorbers in the atmosphere (Petty 2006)

Absorption is a consequence of the distinct energy levels of atmospheric molecules. The total energy in a molecule is contained in the electron orbital levels, vibrational states, rotational states, and finally translational movement. The quantum nature of the orbital, vibrational, and rotational states causes discrete absorption lines. These lines have widths due to molecular collisions, pressure broadening, and Doppler broadening, the Doppler shift caused from the radiation incident on the moving molecules. From Beer's Law, the transmittance due to molecular absorption, defined as one minus the total absorption, can be determined by the equations,

$$T = e^{-\tau} \, , \tag{2.1}$$

$$\tau = \int_{s_1}^{s_2} k\rho r \, ds \, , \tag{2.2}$$

11

where τ is the optical path or optical thickness when measured vertically, k is the mass absorption coefficient, ρ is the density of the air, r is the mass of the absorbing gas per unit mass of air, and ds is the differential path length (Wallace and Hobbs 2006).

Scattering, on the other hand, is the reflection of energy in all directions by particles causing laser light to not reach its intended target. Aerosols and hydrometeors, such as rain and ice, are the most significant scattering particles. Water-soluble aerosols grow with relative humidity causing a sharp increase in scattering near the top of the boundary layer (Perram *et al.* 2010). The amount of decrease in radiation due to scattering can be described by the equation,

$$dI = -IkN\sigma ds ,\qquad(2.3)$$

where I is the incident intensity, k is the scattering or absorption efficiency, N is the number of particles per volume of air, σ is the area cross section of each particle, and ds is the differential path length along the ray path. Although scattering particles come in a variety of shapes and sizes, they can be estimated by Mie theory, which assumes spherical particles. Mie theory is based upon the size parameter defined by,

$$x = \frac{2\pi r}{\lambda}\qquad(2.4)$$

where r is the radius of the particle, and λ is the wavelength of the radiation. Scattering is broken into three different classes: Rayleigh, Mie, and geometric optics. For $x \ll 1$ is the Rayleigh scattering regime and causes phenomenon such as the blue seen in the sky caused from atmospheric molecules being much less than the wavelengths of visible light. The Mie scattering regime for $0.1 \leq x \leq 50$ can be seen for example by the

reflection off of clouds at sunset where the cloud droplets are close in size to the visible wavelengths. Finally, for $x > 50$ is the geometric optics regime, which causes rainbows, where the water droplets are much larger than the visible wavelengths. In the Mie and geometric optics regime, the majority of the scattered radiation is directed forward unlike the Rayleigh regime where scattering is divided evenly between the forward and back hemispheres of the particle (Wallace and Hobbs 2006).

Scattering from atmospheric molecular constituents and aerosols not only degrades the laser propagating signal, but also cause noise in the LADAR receiver. The atmospheric backscatter spectral width seen by LIDAR (Light Detection and Ranging) receivers is governed by Brownian motion and wind turbulence. These systems measure the frequency shift caused by Doppler effects, which is similar to the way continuous wave LADAR's operate. Brownian motion is the random drifting and collisions of molecules in a suspended medium. The spectral width is wider for faster moving particles. The speed distribution can be described by a Gaussian with a standard deviation of,

$$\partial V_r = \sqrt{\frac{k_B T}{m}} \tag{2.5}$$

where k_B is Boltzmann's constant in Joules/Kelvin, T is temperature in Kelvin, and m is the mass in kilograms. The most common atmospheric molecule, N_2, has a standard deviation of 298 m/s while heavier aerosol particles have a standard deviation of 1 mm/s at 300K. The much slower aerosols cause a much narrower spectral backscatter return. If aerosol densities are significant, the backscatter from the aerosols will be much higher in intensity. Generally, the largest external contributors to noise in LADAR receivers in

13

order is the aerosol backscatter, molecular backscatter, and then the background light as seen in Figure 2 (Fujii and Fukuchi 2005).
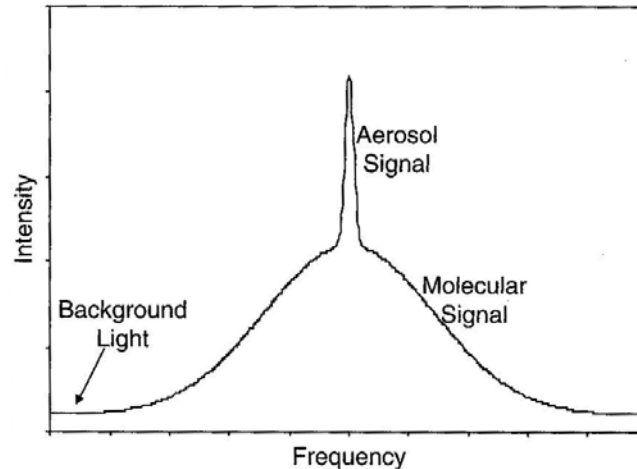
Figure 2. Theoretical contribution of backscatter intensity and frequency spread (Fujii and Fukuchi 2005).

Turbulence, atmosphere motion, is also a major contribution to laser propagation degradation. Optical turbulence is the distortion of electromagnetic radiation due to temperature gradients caused by atmospheric turbulent motions. These motions range in size from the molecular to the planetary scale. Laser systems are especially sensitive to optical turbulence effects from the resulting vertical temperature differences, wind shear, and inertial cascades in the atmosphere. Temperature gradients caused by turbulence result in variations in the index of refraction changing the "optical distances" for different wavelengths. The changing index of refraction ultimately causes phase aberrations (blurring), and amplitude fluctuations (flickering), of the propagating wave. Scintillation, or the change in amplitude and phases, is one way to measure atmospheric turbulence. Scintillation is most commonly described by the refraction structure constant, C_n^2 $(m^{-2/3})$ established by Kolmogorov's theory and is routinely measured at meteorological sites

14

throughout the world. Refraction structure constant values range from weak turbulence, $10^{-17} m^{-2/3}$ to strong values, $10^{-13} m^{-2/3}$. C_n^2 values are highly variable, but in general, are a maximum at the surface decreasing rapidly through the troposphere with a secondary, much smaller maximum in the tropopause. Some turbulence effects can be reduced with beam control systems including adaptive optics. Turbulence greatly affects LADAR systems because of the importance of maintaining wave geometry to receive accurate information (Perram *et al.* 2010).

2.2.2   LADAR Systems

LADAR is a special application of a Light Detection and Ranging (LIDAR) system first applied in 1949, using search light mirrors and photo electrical cell detectors to measure cloud decks. Present day LIDAR usually involves lasers and has many applications from atmospheric studies to algae detection (Fujii and Fukuchi 2005). LIDAR and LADAR can be categorized by transmitted waveform (CW, modulated or pulsed), receiver concept (heterodyne or direct detection), or intended measurement such as range, velocity, backscatter and spectral absorption. In heterodyne receivers, part of the outgoing signal is split and sent to the receiver where the detector acts as a classical mixer. The circuitry is not sensitive enough to respond to the LADAR high frequency, but can measure the difference between the outgoing signal and the Doppler shifted signal from a moving target. Direct detection systems use pulsed lasers measuring the reflected energy and time between the sent and received signal.

LADAR is quite limited in usable wavelengths due to design considerations and atmospheric windows, unlike RADAR which has considerable flexibility in usable frequency bands. Typical wavelengths used by LADAR are 9 to 11 μm for CO_2, 1.06

μm for Nd:YAG, and 1.5 μm for erbium-doped material lasers. Because of the limited

control over operational frequency on LADAR systems, the atmospheric effects on the

transmitted signal are of great concern. The main classes of LADAR systems are

designator class and Continuous Wave (CW) or long pulse coherent class. The

designator class is an incoherent, short pulse, low duty cycle laser while the CW or

modulated long pulse systems are coherent with near unity duty cycle (Richmond and

Cain 2010). A unique capability of LADAR is that its high resolution is able to produce

three-dimensional (3D) imagery. Direct detection system 3D imaging is accomplished by

a timing circuit with pixilated distance measurements. The difference in measurable

depth is described by the simple formula,

$$\Delta x \geq \frac{c}{2} \Delta t \text{ ,}$$

(2.6)

where Δx is depth resolution, c is the speed of light, and Δt is the change in time. Depth

resolution is limited by whichever is longest, the laser pulse length, detection system time

constant, or photon counting time-bin width (Fujii and Fukuchi 2005).

A lot happens to the LADAR signal between the time it leaves the system and

returns to hit the detector. The LADAR end-to-end equation captures the signal's

journey as,

$$P_{det} = \frac{\tau_0 \tau_a^2 D_R^2 \rho_t (dA) P_t}{R^2 \theta_R (\theta_t R)^2},$$

(2.7)

where

       P_{det} = returned power seen by the detector (W)
       τ_0 = transmission of the receiver optics
       τ_a = atmospheric transmission
       D_R = receiver aperture diameter (m)

ρ_t = target surface reflectivity generally between 2 and 25%
dA = surface area parameter (m^2)
P_t = transmitted power (W)
R = range to the target (m)
θ_R = target surface solid angle dispersion (π steradians for Lambertian targets)
θ_t = transmission angular divergence (rad)

The equation assumes a pulse rectangular in shape that exists for a period of time equal to the pulse width. The equation also assumes that the transmitted beam is hitting the target at an angle normal to the target's surface. To account for various non-normal incident angles on a realistic target surface, the bidirectional reflectance distribution function (BRDF) would need to be incorporated. The BRDF is a 4D function that determines the amount of reflected light as a function of incidence, observation, local azimuth, and zenith angles (Richmond and Cain 2010).

LADAR receivers transform photons into detectable electrons called photoelectrons. The mean number of photoelectrons produced in the receiver is determined by,

$$E[N_{signal}] = \eta \left(\frac{P_{det}\Delta t}{h v} \right), \tag{2.8}$$

where E is the expectation operator, N_{signal} is the number of photoelectrons produced by the detector, η is the quantum efficiency of the detector and Δt is the integration time of the detector circuit (Richmond and Cain 2010).

Noise is entered into the system primarily by four different means, photon counting, laser speckle, thermal, and background noise. Although the expectation value of the number of photons received within a period of time is constant, the actual number is random due to quantum effects. Photon counting noise is usually extremely small in

17

comparison to the other contributors. Laser speckle is caused from the interference from several independent coherent signals. Speckle is proportional to the square of the power incident on the detector and quickly becomes dominant when the signal is almost entirely coherent. Thermal noise is seen because all objects not at zero Kelvin radiate photons. Background noise is any radiation not from the LADAR beam, usually caused by the sun's radiation hitting the receiver. The total signal-to-noise can be approximated by,

$$SNR = \frac{N_{signal}}{\sqrt{Q_n^2 + \sigma_{speckle}^2 + N_b}},$$
(2.9)

where Q_n is the charge standard deviation of the number of thermal noise electrons, $\sigma_{speckle}^2$ is the variance of the measured photo counts, and N_b is the number of photoelectrons contributed by the background (Richmond and Cain 2010). The signal-to-noise analysis given in this equation is for a system with a constant background that can be subtracted and the noise is the variance of the signal. The strength of the signal in a coherent detection system is usually characterized by the ratio of the heterodyne signal photocurrent at the difference frequency and the receiver noise current, defined as the carrier-to-noise ratio (CNR). CNR is a concept from RF communication and radar nomenclature (Fujii and Fukuchi 2005). For incoherent pulsed systems operating in Geiger mode, the signal-to-noise ratio is merely the total number of signal photons divided by the total number of noise photons because a constant background cannot be subtracted. The noise in this case is any photons that do not originate from the laser reflecting off of the target.

A variety of noise sources impact the detection and false alarm rates of a system. A false alarm is defined as a detector count at a location other than the target location.

Special cases causing different false alarm rates include that the noise sources may be non-Gaussian, targets may be smooth or diffuse, incoherent SNR is quadratically related to power, and the atmospheric turbulence can cause log-normal fluctuations. Detection statistics that describe microwave radars can be applied to coherent detection systems because of the local feedback signal. These statistics, developed by Marcum and Swerling, are based on fluctuating signal intensities in a Gaussian noise receiver of a microwave search radar system. For direct detection systems, on the other hand, because of the small number of photons, quantum statistics must be used unless a high signal-to-noise is present in which case continuous probabilities can be applied to determine detection statistics (Jelalian 1992).

The background light noise depends on the background radiating source or sources, whether they are well described by a thermal blackbody or reflected radiation. Also, the atmosphere attenuates the background radiation source just as the primary laser signal is subject to attenuation. The background spectral radiance is measured in units of radiance per wavelength ($Wm^{-2}m^{-1}sr^{-1}$). Planck's equation describing blackbody radiation at a specific wavelength λ assuming a Lambertian source is given by,

$$L_{bg} = \frac{\varepsilon 2hc^2}{\lambda^5 (e^{hc/\lambda k_B T_{bb}} - 1)}, \tag{2.10}$$

where ε is the source emissivity with temperature T_{bb} and k_B is Boltzmann's constant. Though many emitting sources are well described by a blackbody, the smaller features of the emitting spectrum are not accounted for, as can be seen in the sun's emitting spectrum. The wave dependent absorption, transmission and scattering by atmospheric particles must also be accounted for in order to determine received radiation. The amount of background light radiation

19

detected by the LADAR receiver is found by integrating the spectral radiance over the receiver

aperture, A_r, field of view, Ω, filter bandwidth, $\Delta\lambda$, and transmission losses, T. The background

radiance can be approximated by,

$$P_{bg} \approx TA_r\Omega\Delta\lambda L_{bg}. \tag{2.11}$$

This approximation is most accurate for narrowband systems looking at a specific wavelength

(Fujii and Fukuchi 2005).

2.3   Relevant Research

2.3.1   Modeling

In order to fully understand the dynamic nature of atmospheric effects on

electromagnetic propagation, several models have been developed. The uniqueness in

the LEEDR model developed by AFIT/CDE is that it incorporates a correlated,

probabilistic climatological database that creates realistic atmosphere profiles. LEEDR

allows for the creation of vertical profiles of temperature, pressure, water vapor content,

optical turbulence, and atmospheric particulates including hydrometeors. The major

advantage of LEEDR's probabilistic approach is that vertical profiles are produced for a

specific location and time based on the statistical likelihood of that specific profile

occurring. This type of profile is drastically different than a standard atmosphere profile

where density is assumed to vary with height characterized by a dry adiabatic lapse rate.

The standard atmosphere was created by using averages over time at specific altitudes.

Because the standard atmosphere is made of averages at each layer, the entire profile is

not necessarily a profile that has actually occurred. Using LEEDR, an actual ground

weather condition that has existed is chosen from which a profile is built. The user has

the option of choosing a probabilistic percentage of how dry or damp of an atmosphere

20

from within the distribution of atmospheres at a given location. LEEDR has 573 land locations of surface data to produce probabilistic profiles (Fiorino *et al.* 2008).

Probability density function databases used in LEEDR are the Extreme and Percentile Environmental Reference Tables (ExPERT), Master Database for Optical Turbulence Research in Support of the Air borne Laser, and the Global Aerosol Data Set (GADS). Molecular absorption is computed for the top 13 absorbing species using the HITRAN 2010 database with a molecular absorption continuum code. The Wiscombe Mie model computes aerosol and hydrometeor scattering and absorption. Climatological turbulence profiles are produced by correlating relative humidities between data from the Master Database for Optical Turbulence Research in Support of the Airborne Laser tailored and the ExPERT data base. The C_n^2 profiles used are based upon relative humidity because optical turbulence and relative humidity have been shown to be largely interrelated, but the exact reason why they are linked is unclear. Cloud-free line of sight (CFLOS) probability is obtained from the Air Force Combat Climatology Center ground-to-space CFLOS tables (Fiorino *et al.* 2009).

Within LEEDR, the boundary layer temperature, as well as dew point temperature, is allowed to vary with a constant water vapor mixing ratio. The change in temperature $\frac{dT}{dz}$ and dew point temperature $\frac{dT_d}{dz}$ is calculated using the equations,

$$\frac{dT}{dz} = -\frac{g}{c_p}\frac{1 + l_v {}^{w_s}/_{RT}}{1 + l_v^2 {}^{w_s}/_{c_p R_v T^2}}, \tag{2.12}$$

$$\frac{dT_d}{dz} \approx -\frac{g}{w_\varepsilon l_v}\frac{T_d^2}{T}, \tag{2.13}$$

21

where g is the gravitational constant, l_v is the latent heat of vaporization of water, w_s is the saturation mixture ratio of water, c_p is the specific heat of air at constant pressure, R is the gas constant, R_v is the moist air gas constant, and w_ε is the ratio of the molecular weight of water over the molecular weight of dry air. Because temperature lapses at a greater rate than the dew point, saturation often occurs within the boundary layer. Aerosol sizes are greatly affected by the variation in the relative humidity causing a spike in laser propagation attenuation as seen in Figure 3. Attenuation increases as aerosol sizes increase with relative humidity, even though number density remains constant throughout the boundary layer. This spike is often seen in LIDAR measurements but is not captured in transmission models using a standard atmosphere (Fiorino *et al.* 2008).
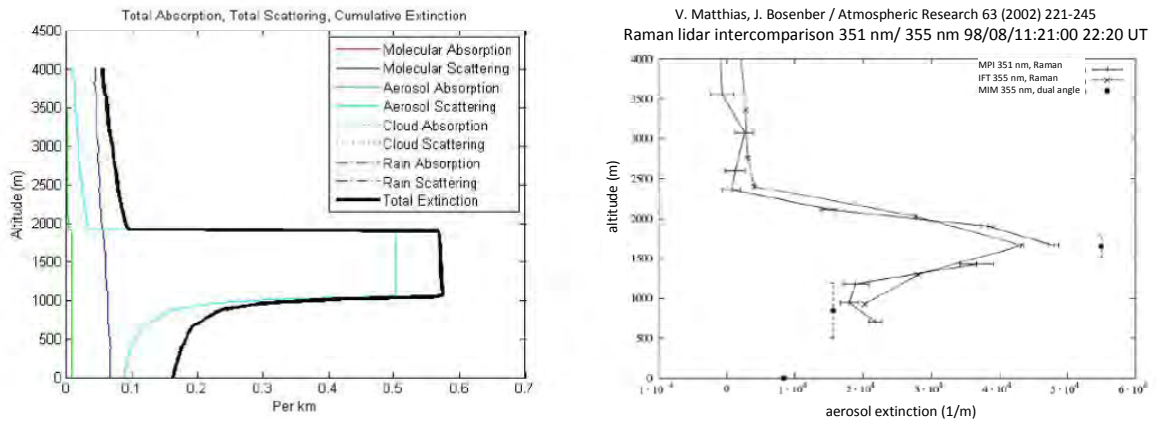
Figure 3. Example of increased attenuation at top of boundary layer due to swollen aerosols. Left is output from LEEDR, right is a LIDAR measurement (Fiorino *et al.* 2008).

The Fast Atmospheric Signature Code (FASCODE) model has become the standard for atmospheric radiation transfer, and the background for band model approaches to radiation transport. FASCODE is a first principles, line-by-line atmospheric radiance and transmittance model developed by AFRL (Mazuk and Lynch

2001). The code was first developed in 1978 by AFRL, Air Force Geophysics

Laboratory as an improvement from the HIRACC algorithm which was developed for a

uniform atmospheric path with constant temperature, pressure and absorber

concentration. FASCODE uses the HIRACC algorithm but approximates the atmosphere

by a series of layers and incorporating the more realistic Voigt line shape. At high

altitudes, the Doppler, Gaussian line shape dominates while at lower altitudes the

pressure broadened Lorentz shape dominates. The Voigt function used in FASCODE is a

weighted sum of the Doppler function and the Lorentz function. The model uses a series

of atmospheric layers to allow for thermodynamic properties and densities of absorber

molecules to vary. The algorithms within FASCODE were developed with accurate

approximations and techniques to minimize computer time. One such technique was the

larger sampling interval at lower altitudes where line shapes are broader. Absorption is

the only attenuating parameter in the original FASCODE model, neglecting scattering

and turbulence effects. Because absorption is the largest attenuating factor in the rural

clear sky atmosphere, FASCODE gives reasonably good transmission and radiance

approximations in these conditions. Considering the computational limitations at the

time, FASCODE was a monumental advance in atmospheric radiation transfer studies

(Smith *et al.* 1978).

       Since its inception, FASCODE has undergone many upgrades. The latest version

of FASCODE now called FASCODE for the Environment (FASE) incorporates the

Department of Energy's standard radiative transfer model, Line-by-Line Atmospheric

radiation Code (LBLRTM) along with several other upgrades. The major consideration

in the upgrades in FASE is the increased computational capacity of the modern computer.

New cross-sections for heavy molecules, improved solar irradiance model, and Schumann-Runge bands have been added. Also, the code has been formatted for improved flexibility, maintainability, and usability (Snell, Moncet *et al.* 1995). Improved coding issues including line shape and radiance algorithms for H_2O and CO_2 continua, code vectorization and array parameterization have been inserted. The spectral range of a radiation transfer run was increased from 520 cm^{-1} to 110 cm^{-1}. The index of refraction calculation was approximated in the previous FASCODE, now replaced with the exact formulation of the index of refraction as shown by Kneizys *et al*. (1983). FASE now accepts HITAN 96 line parameters and upgraded from using 32 species to 36 species. An upgrade to cloud and rain parameters was implemented. The clouds now have more advanced adjustable parameters to more realistically specify cloud characteristics. The LASER calculations option has an enhanced method of specifying the boundary emissivity or reflectivity and new coefficients for absorption cross-sections (Snell *et al.* 1996). The merging of FASCODE and LBLRTM with the above upgrades has resulted in a flexible radiative transfer model, but needs to undergo comparisons with other models and validation against data sets (Snell *et al.* 2000).

2.3.2   Previous Research

Several LADAR simulations have been produced in an attempt to accurately capture environmental effects. For instance, BAE Systems created a complete 3D LADAR model that incorporated both atmospheric transmission and scattering. The rigorous treatment of the laser spatial distribution and backscatter based on a Gaussian pulse with a random distribution gain variance is unique to this model. The BAE model intricately accounts for the spatial resolution across the pixels of a receiver array.

Performance parameters such as the noise equivalent power, signal-to-noise ratio, and detection probability of a specified LADAR system can be analyzed as a function of range, gain, or pixels on target. The model is built to incorporate standard atmospheric parameters from MODTRAN or FASCODE to produce a single path transmission, extinction coefficient, and scattering-to-extinction ratio. The Air Force optical radiation backscatter model, BACKSCAT is then used to determine a backscatter coefficient (Grasso *et al.* 2006).

Apart from the strengths of the BAE model listed above, there are several weaknesses. By using standard atmosphere profiles, real boundary layer effects are being neglected. Also, because only a single scattering coefficient is being used, the large scattering difference above and below the boundary layer is being averaged. Noise sources included in the model are detector dark current, solar reflection off the target, target blackbody emission, and laser backscatter. The laser backscatter is only taken at one range location inside the gate. Also, the solar scatter off of atmospheric particles is neglected. Solar scatter in the receiver field of view many times is the primary noise source for a LADAR system. Incorporating LEEDR atmosphere profiles into LADAR models such as that created by BAE or those described by Brown *et al.* (2005) and Telgarsky *et al.* (2004) can allow for a complete characterization of the atmosphere. Integrating LEEDR's ability to capture the variability of scattering and extinction coefficients with altitude, boundary layer effects, and account for solar atmospheric scatter can make LADAR models more accurate.

An enhanced atmospheric effects model is important to the LADAR community as recent advances in technology have made available to the LADAR system designer a

multitude of options. Several wavebands and their compatible detectors are now available to choose from. Because of this increase in options it is important to study the accompanying trade space. In a study by Osche and Young, theoretical comparisons were made between a 1.54, 2.092, and 10.59 μm wavelength systems. Available laser systems and their accompanying detectors were compared along with atmospheric effects at their respective wavelengths. The atmospheric effects were produced with FASSCODE and MODTRAN using rural, urban, and maritime aerosol models with a mid-latitude summer standard atmosphere. Fog and rain conditions were also considered. The study compared range visibility at the different wavelengths with different environmental conditions. The study concluded that near infrared systems (1.54 and 2.092 μm) do not suffer from water absorption at long ranges like the far infrared systems (10.59 μm) experience. Far infrared systems outperform near infrared systems being able to penetrate fog (Osche and Young 1996).

Past research has been done on an assessment of LADAR at 1.0642 μm and 1.557 μm signal-to-noise ratios comparing LEEDR to standard atmosphere profiles. The standard profiles were MODTRAN with rural aerosols. The assessment actually used HELEEOS which contains the LEEDR package within it. Variations in the boundary layer, heavy rain, thick fog, and cloud-free line of sight probabilities were evaluated. Two geometries were examined with the laser at an altitude of 1525 m with a path length 1530 m and 3000 m to a ground target. The signal received was calculated using the standard laser radar equation for extended Lambertian targets,

$$P_r = P_s \cdot \frac{D^2}{4R^2} \rho \cdot T \cdot \eta_t \cdot \eta_r \,, \tag{2.14}$$

where P_r is the power received, P_s is the power transmitted, D is the aperture diameter, R is the slant range, ρ is the optimal reflectance (33.33%), T is the roundtrip transmittance through the atmosphere, η_t is the system optical efficiency, and η_r is the receiver optical efficiency. The noise was calculated using the noise equivalent power equation,

$$NEP = \frac{hc}{\lambda} \cdot \frac{2B}{\eta}, \tag{2.15}$$

where NEP is the noise equivalent power, h is Planck's constant, c is the speed of light, λ is the LADAR wavelength, B is the bandwidth, and η is the quantum efficiency. These equations contain many approximations and neglect the background radiation. In the study, climatologically based transmittance values were significantly less than those produced with the standard profile over the ocean due to sea salt aerosols being hydroscopic. Overall, standard profiles gave an overly optimistic estimate of transmission, and therefore signal-to-noise ratios. For heavy rain conditions, LADAR systems were shown to be severely limited. The 150 m thick fog layer reduced the system capability by 93% for the oblique geometry and 75% for the vertical geometry (Fiorino *et al.* 2009).

Another study using LEEDR to examine LADAR showed that 1 to 2 µm wavelengths had little capability in cloud-free heavy rain but still outperformed sub-millimeter to millimeter radar. LADAR had no performance through clouds or fog, while radar is only slightly affected in these conditions. However, due to a large number of rain drops being very nearly the same size as the sub-millimeter to millimeter wavelengths of the radar, and raindrops being somewhat transparent in the µm wavelengths, LADAR

27

outperforms radar in heavy rain conditions. This study used very similar techniques to the previous study of LEEDR to standard atmosphere profiles in determining signal-to-noise ratios (Fiorino *et al.* 2010).

A major advantage of LADAR is that the laser signal is very narrow making it covert. The signal is concentrated to a specific region and is not being spread as is traditional radar. Off-axis scattering from the laser hitting atmospheric particles and physical objects though can be detected by an observer not collocated with the system. In a recent study, off-axis laser scatter has been detectable at about a 1 km range and an off-axis angle of 1.22 degrees for a 1 to 5 watt laser. The range and off-axis detectable angle are expected to be much greater for a more powerful laser. AFIT's HELEEOS code was used to model the off-axis scatter, allowing scatter by molecules and aerosols to be observed at an off-axis point while incorporating spreading and blooming effects. Aerosol distributions along the laser and the observer path were accomplished by determining the visibility and climatological aerosols for southwestern Ohio (Fiorino *et al.* 2010). The modeled results were compared to measured data from a turbulence laser profiler beam that was imaged off-axis with a calibrated camera array. In order to see the off-axis signal, a background subtraction algorithm was used. Radiance values were averaged over several frames when the laser was off, and then subtracted from frames in which the laser was on. Temporal fluctuations caused the noise to remain too high for the signal to be detected. Because the majority of the frame is background noise, an additional noise subtraction was done by building a histogram to determine the background radiance. Subtracting out the rest of this noise sufficiently minimizes the background allowing the scattered signal to be seen. The background still contained

28

noise which could not be eliminated. The HELEEOS-modeled off-axis irradiance was within two orders of magnitude of the measured irradiance. Considering the measured values were on the order of 10^{-8} W/m^2, the modeled values gave a good approximation. The agreement was not close enough to serve as a validation for HELEEOS (Fiorino *et al.* 2010).

Although previous work has been accomplished in using atmospheric models to characterize the effects the atmosphere may have on LADAR propagation, a first principals complete integration of the physics included in LEEDR has not. The physics other models ignore include an increase in scattering at the top of the boundary layer, climatological variation, and turbulence effects. Although LEEDR has been used previously to produce worldwide signal-to-noise ratios, only atmospheric transmission was used in conjunction with an arbitrary sensor noise level. Presented here is the first study using LEEDR that includes atmospheric transmission and scattering effects on a LADAR systems performance.

2.4 Summary

By introducing the relevant science and past research in the current literature that pertains to modeling LADAR propagation through the atmosphere, the reader is now better prepared to understand the methodology of this work. This thesis combines the science of atmosphere radiation transfer, laser remote sensing, and advanced physics-based models. Now that these subject areas have been thoroughly introduced, a detailed account of the approach taken in using LEEDR to produce simulations of LADAR signal-to-noise ratios and what steps were taken to accomplish this is shown in Chapter three.

III Methodology

3.1 Chapter Overview

The purpose of this chapter is to give a detailed account of the approach taken to demonstrate if there are advantages when modeling LADAR propagation using location specific probabilistic atmospheric characterizations such as those created by LEEDR. An explanation and overview of the tools used and how they were exploited is discussed. The modeled scenarios for comparing signal-to-noise are laid out. The process of creating signal-to-noise values using LEEDR is explained along with how comparisons were made against standard atmosphere characterizations and assessments done with FASCODE.

This research contains two main parts, first to compute worldwide signal-to-noise ratios, and second to produce images at a specified location incorporating signal and noise returns. All results are for a simulated pulsed direct detect system operating in Geiger mode. Both parts were accomplished using the tools described here in combination with Matlab scripts that are included in Appendix A. The global signal-to-noise ratios are completed for airborne LADAR system geometries targeting objects at the ground. A low altitude short range engagement along with a high altitude long range engagement is examined. The low altitude engagement has the platform at 1,530 meters Above Ground Level (AGL) with a slant path of 3,000 meters. The high altitude engagement has the platform at 10,000 meters AGL with a slant path of 50,000 meters. The completely vertical path for both the low and high altitude scenarios is also analyzed. The low altitude engagement is a possible flight profile for small remotely piloted aircraft (RPA) while the high altitude engagement is a possible flight profile for a traditional

30

manned aircraft. Both the slanted and vertical geometries are studied here to demonstrate the effects different paths through the atmosphere have on laser propagation.

Three wavelengths are considered, 1.0642, 1.56, and 2.039 μm. All modeled runs are completed for clear sky conditions, meaning no clouds or precipitation, and with the sun directly overhead at a zero zenith angle. The zero zenith angle for the sun is chosen to keep the geometry simple with platform, target, and sun in the same plane. LEEDR-produced signal-to-noise ratios are computed for the worldwide 573 ExPERT sites. The ExPERT atmosphere, also referred throughout this document as the LEEDR atmosphere, is taken for a summer day at 1500-1800 local when the boundary layer is fully developed. The 50th humidity percentile is chosen along with Global Aerosol Data Set (GADS) aerosol profiles for the LEEDR atmosphere. ExPERT site signal-to-noise ratios are compared to signal-to-noise values produced for various standard atmospheres and standard aerosol profiles. FASCODE transmissions are computed using Phillips Laboratory ExPERT User Software (PLEXUS). LADAR target signal returns are created from these transmissions. Signal-to-noise ratios are then found by using the standard atmosphere computed noise. Developing noise sources with FASCODE is beyond the scope of this study. This "FASCODE" signal-to-noise is then compared to LEEDR created target signal returns. Although this is not a fair assessment of FASCODE as the signal is only half the equation, it does give insight into the significance of using different total path transmissions in computing the target signal.

For the purposes of this study, only atmospheric signal and noise values are considered. All other sources of noise due to the actual LADAR sensor are ignored. LASER speckle noise is also ignored. Given the intent of this study to compare

31

atmospheric propagation models, the signal and noise returns at the LADAR platform are computed before entering the actual receiver optics. Signal returns for the down looking engagements are based on a Lambertian reflecting flat target normal to the LADAR beam with a 10% reflectivity. Noise returns are comprised of any energy sources that did not originate from the laser reflecting off the target. The noise sources are laser backscatter from atmospheric particles, solar reflection off the target, solar scatter off atmospheric particles in the field of view, and blackbody emission from the target. Signal-to-noise ratios are then simply computed by dividing the total signal photons by the noise photons.

To produce images incorporating signal and noise returns, images of a 2 m tip to tail remotely piloted aircraft are created using the High Energy Laser System End to End Model (HELSEEM). The short and long range slant paths are examined, except this time the platform is located on the ground looking up. The HELSEEM configuration looking at the RPA was originally created for the AFIT CDE RPA tracking system. Noise returns and transmission values are calculated using ExPERT and standard atmosphere profiles in LEEDR. The noise is incorporated into the pixel values from HELSEEM giving a visual demonstration of the effect the noise sources have on resolving the target. After all noise sources are included, the image is then fed through AFIT CDE's light tunneling algorithm using MZA Corporation's implementation of Light-Tunneling within WaveTrain. For this research, LEEDR-produced climatological turbulence profiles are inserted into the algorithm which simulates blurring due to atmospheric turbulence. Once again only atmospheric effects were considered, ignoring the noise contributions and effects from the LADAR receiver.

## 3.2	Tools Used

### 3.2.1	Laser Environmental Effects Definition and Reference (LEEDR)

LEEDR produces worldwide probabilistic profiles based on historical weather data and predicts radiation transfer through the atmosphere. The primary objectives as stated in the user's manual are:

1. To create correlated, vertical profiles of meteorological data and environmental effects such as gaseous and particle extinction, optical turbulence, and cloud free line of sight.

2. To allow graphical access to and export of the probabilistic data from the ExPERT database (LEEDR User Guide Version 3.0 2011).

Chosen atmospheric parameters create the desired profile from which absorption, scattering, and total extinction are calculated. Atmospheric inputs include any global location, summer or winter season, local time of day in three hour blocks, relative humidity percentile conditions, a standard atmospheric condition, and a specified aerosol effects model. If one of the 573 red dot locations is selected, as seen in Figure 4, then specific site surface and upper air probabilistic data is pulled from the ExPERT database. The atmosphere tab inputs include eight turbulence profiles, two wind models, and various rain and cloud types at different altitudes. Among the available turbulence profiles is a climatological profile, a novel feature of LEEDR. The climatological turbulences are produced by correlating the temperature and relative humidity percentiles in the ExPERT database to percentage values in the Master Database for Optical Turbulence Research in Support of the Airborne Laser (Fiorino *et al.* 2008). The laser and geometry tab allows for a desired laser wavelength and geometry.

33
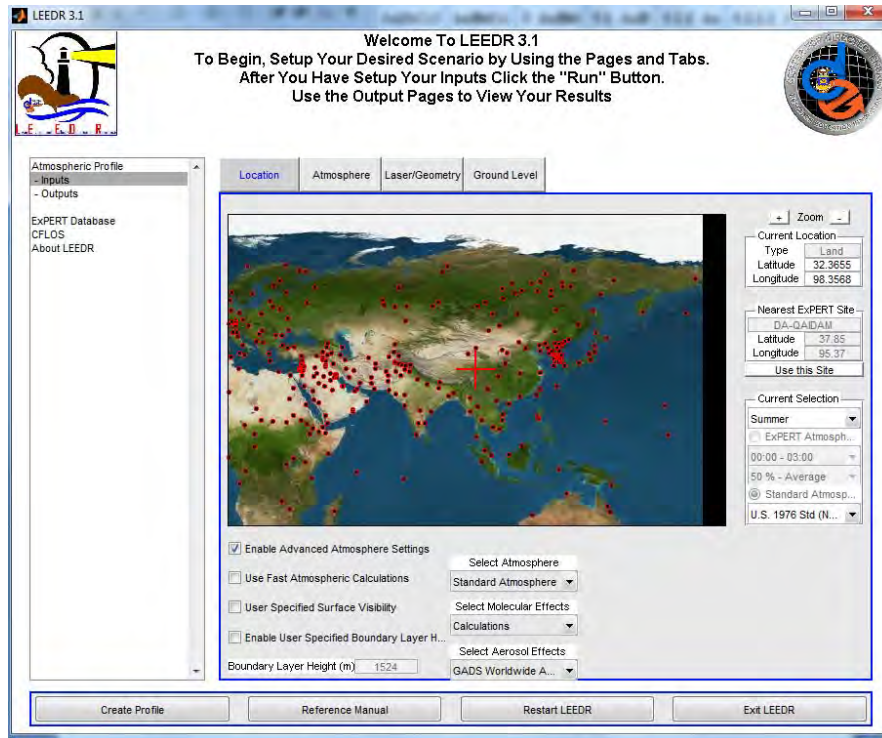
Figure 4. LEEDR inputs screen

3.2.2   High Energy Laser End-to-End Operational Simulation (HELEEOS)

HELEEOS models dynamic high energy laser weapon engagements predicting

laser atmospheric propagation, radiation at the target, and ultimately a probability of kill

statistic. In the laser engagement, the target and platform can move in any direction in

space with specified directions, velocities, and accelerations (Fiorino *et al.* 2009).

LEEDR is the atmospheric propagation package used within HELEEOS. For this

research, LEEDR atmospheres were created in HELEEOS. HELEEOS was originally

created for high energy laser weapon engagements, but has some very useful aspects for

LADAR propagation as well. Running HELEEOS was advantageous because of features

such as the ability to save settings and computing a diffraction spot size on the target

based on the user-defined wavelength, exit aperture, and turbulence profile. A 1 cm exit

aperture and probabilistic turbulence are used throughout this study. The HELEEOS inputs screen is nearly identical to the one found in LEEDR except for the additional input tabs to specify the laser optics and dynamic engagement.

3.2.3   Phillips Laboratory ExPERT User Software (PLEXUS)

PLEXUS is a user oriented software package that integrates seven of the Air Force Research Laboratory atmospheric and astronomical background codes. The integrated codes are the Department of Defense standard spectral radiance and transmittance models for the atmosphere. The software provides a graphical user interface, as seen in Figure 5, which allows the user to make various selections to create outputs for physically realistic simulations. PLEXUS also contains tools to display and analyze spectral transmission and radiance outputs (Help for PLEXUS 2006).

The 2006 release of PLEXUS 3.0 beta 1 is used in this study. The 1997 release of FASCODE 3 with HITRAN 2000 is contained in PLEXUS and is run to compute laser line transmission. According to the user's manual, FASCODE "is a first principle code which provides high resolution spectral radiance based on line-by-line calculations. This code provides the accuracy typically required for laser propagation applications (Help for PLEXUS 2006)."
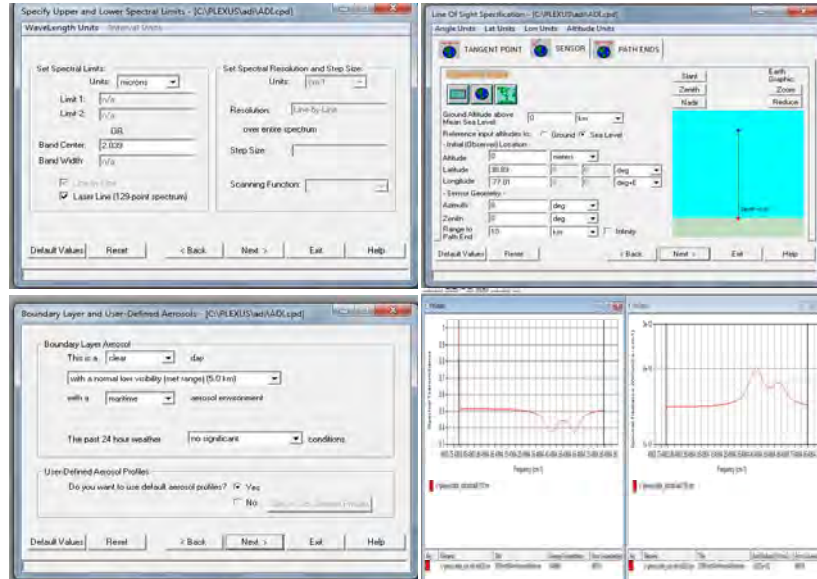
Figure 5. **A few of the PLEXUS input screens and the output screen with a transmission and radiance plot**

3.2.4 High Energy Laser System End-to-End Model (HELSEEM)

HELSEEM is a flexible open architecture code that simulates high energy laser system scenarios. The open architecture is achieved by using the Joint-services Message Passing Simulation (JMPS) framework from which different components can be easily added, subtracted or modified. The model was created to be an all purpose simulation platform for the high energy laser community that caters to various users, fidelity levels, and scenarios. HELSEEM incorporates high-performance legacy codes and has the ability to build wrappers around additional code (Ritter *et al.* 2009).

AFIT CDE is in the process of building a RPA tracking simulation system built on the HELSEEM architecture which is then fed into atmospheric, light-tunneling, and sensor effects code. The RPA tracking HELSEEM code produces an illuminated pristine image of a target from incident laser radiation without atmospheric or blurring effects, as seen in Figure 6. The pristine image was used in this research, and external noise sources

and turbulence effects were added. The code was used in simple laser one-on-one mode

and run through the Windows command prompt. Some of the inputs into the model and

their settings for this research are included in Table 1.

Table 1. **HELSEEM input parameters and values used in this study.**

Input Name	Input Value
Obscuration	0.0001 m
Beam quality	1.3
Active center of receiver	1.0642 μm, 1.56 μm, and 2.039 μm
Active band of receiver	4 nm
Laser center	1.0642 μm, 1.56 μm, and 2.039 μm
Laser power	20 MW
Camera spacing	Varied based on geometry to maintain a 6.144 m field of view
Resolution	512
Full width half max of laser upon exiting	0.01 m
Target location (x, y, z coordinates in m)	(0, 2580.5, 1530) and (0, 48989.8, 10000)
Sun location	Zero zenith
Laser focus	Varied based on geometry to maintain a 2.9 m full width half max spot size at the target
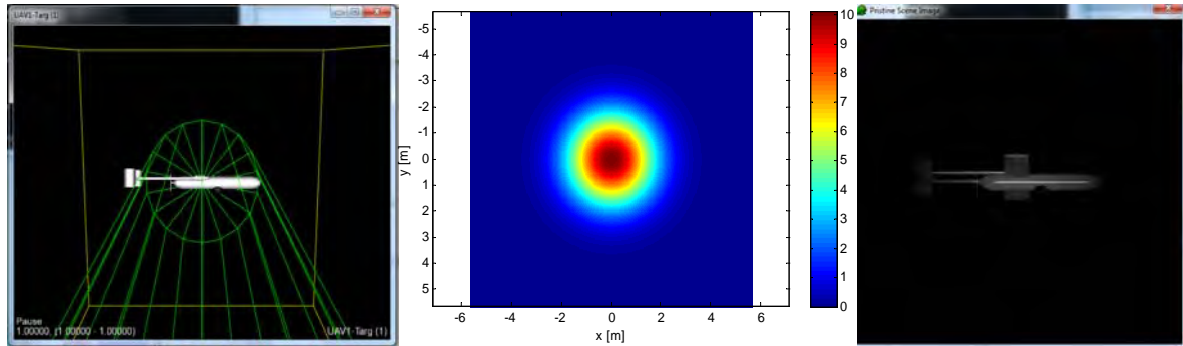
Figure 6. Image outputs from HELSEEM. From left to right the images are, the beam spread in green and the field of view in yellow at the RPA, the Gaussian beam spot at the target, and last is the return signature of the RPA.

3.2.5   Light-Tunneling within WaveTrain

Light-Tunneling is a computationally more efficient approach within WaveTrain

than the traditional Incoherent Reflector model that involves spanning the scene with

many independent speckle realizations. The basic idea of the more efficient approach is to propagate a number of point sources and interpolate the point spread function, also known as the blur function, between these points at the receiver. WaveTrain produces the point spread functions by propagating the point sources through the defined turbulence profile. Superposition is leveraged in that the resulting intensity at any pixel is the sum of its own and the overlap of nearby pixel blurring intensities from the interpolated point spread function. The blurring effects are implemented by creating a Gaussian centered at each of the pristine image pixels and then shifted by a x and y translation based upon the point spread function (Beardmore 2006).

For this study, the LEEDR-produced climatological C_n^2 profiles are fed into WaveTrain. An evenly spaced 16 by 16 point grid of point sources is propagated. Although it is possible to use fewer point sources by concentrating points on the target to optimize the routine, this is not necessary for the limited number of implementations performed. Fifteen equally spaced phase screens are used. These phase screens are determined in WaveTrain and represent the optical aberrations encountered along the path.

3.3   Signal Calculations

A pulsed LADAR system gates a distance around the target to suppress the background and laser backscatter. Within this gate are thousands of bins that determine the depth resolution. In other words, the receiver only opens up after a certain amount of time after the pulse has left the laser and then registers the signal based on an integration time. This integration time is also the width of a bin, usually equal to the pulse length in time. A pulsed Geiger mode LADAR system was used for this analysis. A Geiger mode

system uses avalanche photo diodes (APDs) that are very sensitive allowing for a single photon to be detected. When a photon is detected, the system counts it as a return "saturating" the system. This makes the system very sensitive, but unable to determine how many returns were actually detected as only one return in a single bin will be detected. Also, only one return will be registered per pulse. In reality, the system will be composed of a two dimensional array of APDs which will allow the system to paint a picture of the scene. Dark current from within the sensor itself can also set off an APD, but this is ignored as the study concentrated on only the atmospheric effects. Because any photon can set off an APD, the background light cannot be subtracted and must be considered noise.

The signal was created for a single laser pulse with an assumed rectangular function in time reflecting off a flat Lambertian target. An ideal laser is used in which only a single wavelength is being transmitted. The returned signal irradiance is then a function of the surface normal angle, θ_n, incident irradiance, I_{target}, target reflectance, ρ_t, laser spot size area, dA, atmospheric transmission, τ_a, target to LADAR platform range, R, and the radiation dispersion solid angle, θ_R defined by the equation

$$I_{rec} = \frac{\cos(\theta_n)\, I_{target}\rho_t dA\tau_a}{R^2\theta_R}.$$
(3.1)

The dA term is the illuminated area seen by the detector and in some instances may be limited by the field of view of the detector (Richmond and Cain 2010).

Equation 3.1 gives the target return in irradiance that will only appear in the target bin. In actuality, the signal could be spread over two bins but for this study, it was assumed that the signal fits perfectly into one bin. Because any photon can set off the APD, the noise calculated for this research was the total number of noise photons within

39

the entire gate. The noise contained in the signal bin will in fact add to the detection probability, but for the signal-to-noise ratios in this analysis only the target return was considered signal. This is a good approximation because the noise per bin is typically thousands of times smaller than the sum of the noise from each bin. The signal-to-noise ratio gives a good idea of the probability of detecting a target versus detecting the noise, as will be shown later.

In equation (3.1), the cosine term comes from the fact that intensity observed for a diffusely reflecting surface scales as the cosine of the angle θ_n between the observer and the surface normal. The surface normal angle was zero, the target reflectivity was 0.1, the radiation dispersion sold angle was set to π for Lambertian reflectance, and path transmittance values were computed by LEEDR. The laser spot size was determined from the HELEEOS calculated 1/e of the peak power diffraction with turbulence effects diameter which was about 0.5 m for the 3 km path and 7 m for the 50 km path.

The normal target incident irradiance in equation (3.1) is calculated via,

$$I_{target} = \frac{4P_t\tau_a}{\pi(\theta_t R)^2},$$

(3.2)

where P_t is the average power of the laser pulse and θ_t is the beam divergence angle (Richmond and Cain 2010). The above equation is just the power divided by the area of the laser spot on the target multiplied by the atmospheric transmission. Throughout this research, the power was set to 20 MW and the divergence angle was determined from the angle formed from the edges of the exit aperture to the spot size on the target. LADAR pulsed lasers are typically described by their energy and pulse length. The scenarios here are modeled to closely resemble the JIGSAW LADAR with a 10 mJ 500 ps pulse. This gives a peak power of 20 MW (O'Brien and Fouche 2005).

3.4   Noise Calculations

The noise considered in this research is any external sources of energy that do not originate from the reflection of the laser off the target. Three main noise sources are examined, laser light that is backscattered off of atmospheric particles, sunlight that is scattered in the field of view back to the receiver by atmospheric particles, and the reflection of sun light off the target. Blackbody radiation is also examined, but is negligible for the wavelengths and target temperatures considered. These sources are noise as they are always present and contain no distance information.

Depending upon the pulse repetition frequency and the dwell time on a target, a statistical analysis may be done to subtract out noise returns. This is a result of the target returns all being concentrated within a single bin while the noise returns will be spread out over the entire gate. For this study, it is assumed this statistical analysis cannot be done because either the LADAR operated for a very short amount of time or is scanning very quickly in which case there is not a substantial amount of time for many target returns to be registered within a single bin. Therefore, only single pulse analysis is accomplished for this study.

The signal-to-noise calculations are computed by dividing the signal irradiance by the sum of the noise irradiance in each bin over the entire gate. The solar noise from reflection off the target and scatter off of air particles is constant for every bin, including the target bin. The only noise source that is not constant over the bins is the laser backscatter, normally with a peak in the first bin. In creating signal-to-noise ratios, the units can be kept in irradiance even though by definition the signal-to-noise ratio is the number of signal photons divided by the number of noise photons. To change to photons,

both the signal and noise must be multiplied by the integration time and receiver aperture and divided by the frequency and Planck's constant. These constants all cancel when determining the signal-to-noise ratio. The only difference is the time t, which for the signal is only one bin while the noise is the entire gate. The noise irradiance must be multiplied by the number of bins, assuming the noise is constant across the gate. The laser backscatter is not the same in every bin, and therefore, the noise irradiance I_{noise} in every bin must be summed to find the signal-to-noise ratio SNR according to the equation,

$$SNR = \frac{I_{signal}}{\sum_{i=1}^{b} I_{noise_i}}.$$
(3.3)

 The solar reflection and solar scatter is the same in each bin and can just be multiplied by the number of bins b, but the laser backscatter is different in every bin and must be added individually. Figure 7 displays the irradiance within each bin across the gate for the 10 km altitude vertical path. Ten percent of the path length was gated, so the bin furthest to the right is at an altitude of 1000 m being near the top of the boundary layer where aerosols have swelled. The figure has a sudden jump down after it leaves this region as depicted by bins before about bin number 1700.
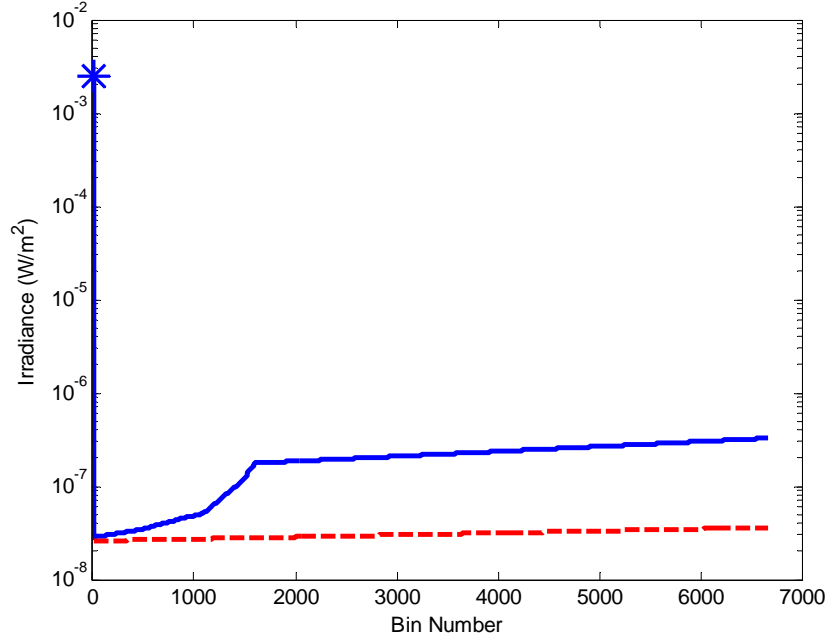
Figure 7. Irradiance values for each bin with the target irradiance at the zero bin represented by an asterisk. The ExPERT Shanghai 10 km slant path simulation, solid blue line and the standard urban atmosphere values, red dashed line values are displayed.

The signal-to-noise ratios computed have direct correlation to the probability of detection and false alarm. This correlation was determined by using Poisson statistics for the single firing APD detector per gate scenario using the equation,

$$P_{target} = e^{-fN}(1 - e^{S-w}), \tag{3.4}$$

where f is the fraction of bins in front of the target, one for this study, N is the total number of noise photons, S is the number of signal photons, and w is N/b where b is the total number of bins. The probability of no primary electron generation is,

$$P_{ne} = e^{-N-S}, \tag{3.5}$$

and the probability of false alarm is,

$$P_{fa} = 1 - P_{target} - P_{ne}. \tag{3.6}$$

The probability of no primary electrons comes from equation (1) from O'Brien and Fouche,

$$P(m; t_1, t_2) = \frac{1}{m!} [M(t_1, t_2)]^m \exp[-M(t_1, t_2)],$$ (3.7)

which is the equation for a Poisson process that m events will occur between times t_1 and t_2. For m=0, or that no primary electrons are created, the equation reduces to $\exp[-M(t_1, t_2)]$. Therefore, the probability of one or more primary electrons is $1 - \exp[-M(t_1, t_2)]$, which is the second term in equation (3.8). For the Geiger mode LADAR, $M(t_1, t_2)$ is the number of photons in a particular bin. Plugging this into,

$$P_j = \exp\left(-\sum_{i=1}^{j-1} M_i\right)[1 - exp(-M_j)],$$ (3.8)

the probability of no electron detection can be found. The equation predicts the probability of the detector firing in the jth bin is determined by the sum of all the photons before and the number of photons in the jth bin. To determine the probability of not firing at all $exp(-M_j)$ is substituted for the second term, $1 - exp(-M_j)$, where M_j is the number of signal photons S. The first term becomes $exp(-N)$ which is the total photons for all the noise bins. This yields equation (3.5), $P_{ne} = e^{-N-S}$. From these equations, probability-of-detection and false-alarm curves as a function of the total number of photons for several different signal-to-noise ratios are produced. The probabilities are a function of the total number of photons because no matter how strong the signal is, if there are a significant number of photons before the target bin, the target will never be seen (O'Brien and Fouche 2005).

From Figure 8, the correlation between, the signal-to-noise ratio and the

probability of detection can be seen. Notice how the probability of detection curve never

rises above the probability of false alarm curve for the signal-to-noise ratio of one case.

Taking the maximum probability of detection for varying signal-to-noise curves and the

probability of false alarm at the same total number of photons yields the plot in Figure 9,

which can be used as a metric.
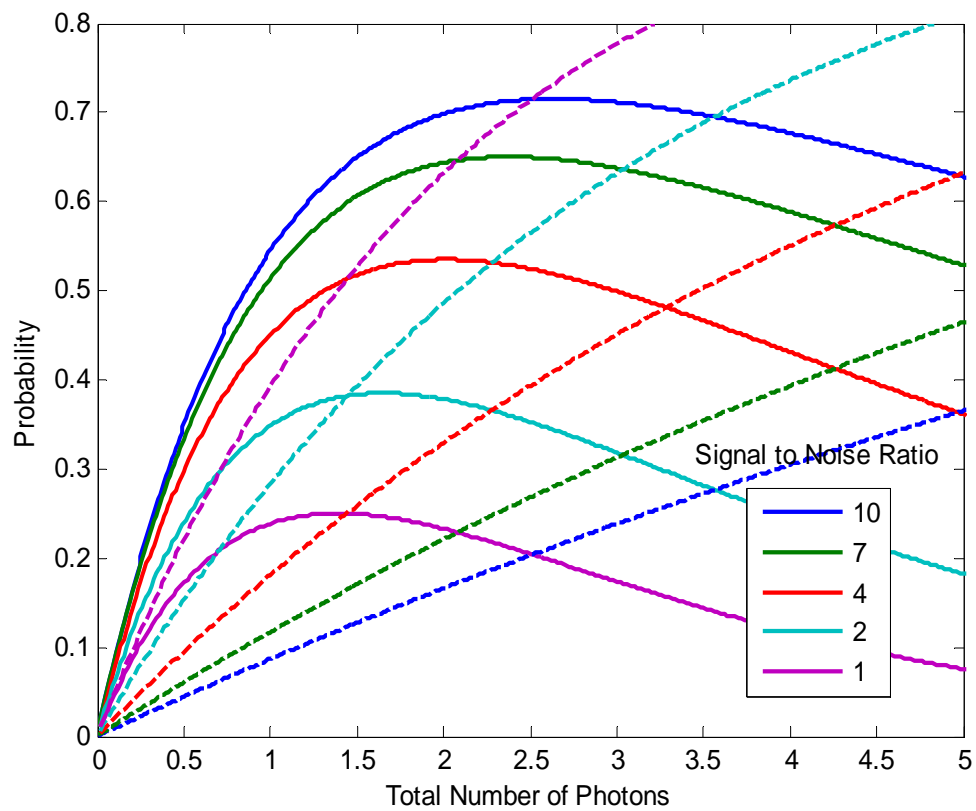
Figure 8. Probability of detection, solid lines, and probability of false alarm, dashed lines as a function of total number of photons for various signal-to-noise ratios.
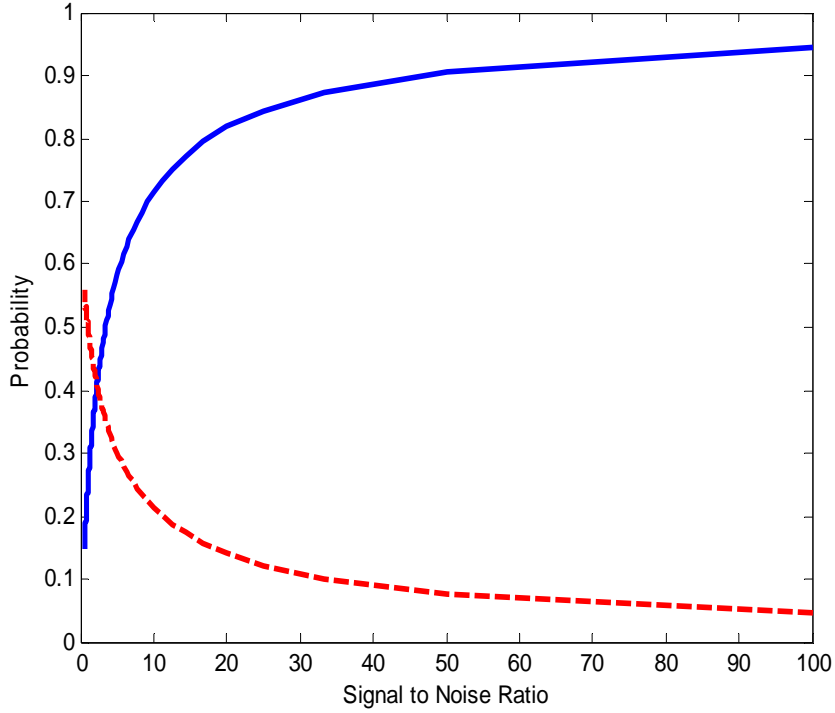
Figure 9. Peak probability of detection, solid line and probability of false alarm, dashed line, as a function of the signal-to-noise ratio.

3.4.1   Laser Scatter Noise

Molecules, aerosols, and hydrometeors in the path of the laser will cause a portion of the laser energy to be reflected back to the receiver. When a laser in the visible band is used in a dusty environment, the entire length of the laser beam is seen; while if it is operated in a vacuum, only the illuminated spot on an object is observed. The beam itself is visible because of the scattering of laser light off of particles suspended in the air. For LADAR systems the back scattered laser intensity can become a major source of noise, especially when there is no knowledge about where the target may be. This scattering of laser light can be expressed by the equation,

$$I_{SCA} = \tau_a \int \frac{P(\theta)\beta_{SCA}I_0}{4\pi R^2} dv \,, \tag{3.9}$$

where I_{SCA} is the backscattered laser irradiance, τ_a is the path transmittance, $P(\theta)$ is the phase function, β_{SCA} is the volume scattering coefficient, I_0 is the incident irradiance, R is the range to the parcel of air, and dv is the differential volume element of the laser (Fiorino *et al.* 2010). The laser scattering equation was performed for both aerosol and molecular scattering.

The scattering integral gives the total backscatter for a continuous laser at an instant in time, but for a pulsed LADAR, the equation represents the total backscatter noise integrated over the entire gate. The equation is turned into a summation of equally spaced bins or segments equal to the pulse length of the laser over the length of the gate. The gate only extended in front of the target bin as there is no laser backscatter beyond the target. The volumes of the segments are determined from creating cylinders with diameters found at the center of each segment. The diameters are calculated by linearly interpolating between the start of the gate diameter and the spot size at the target. The diameter at the start of the gate is found by determining a beam divergence angle from the edge of the exit aperture to the spot size at the target. This assumes the entire beam is in the field of view. Inadvertently, the spot size being calculated using diffraction in HELEEOS was slightly larger than the chosen field of view for the 2.039 μm wavelength. A slight error in the 2.039 μm wavelength signal-to-noise results when laser backscatter is dominate, thought to be less than 10% to high, is introduced. The phase function and volume scattering coefficients are linearly interpolated from the calculated LEEDR values. LEEDR produces 1,000 equally spaced atmospheric layers with these coefficients for any given engagement geometry. The phase function defines the amount of scattered energy per solid angle in a particular direction. The phase function is

dependent upon the direction of energy scattering from its original direction represented by the angle θ as well as altitude, while the volume scattering coefficient is only dependent on altitude. Examples of the phase function plotted against scattering angle and the scattering volume coefficients plotted against altitude are shown in Figure 10. The plots in Figure 10 are created for a 1.0642 μm laser from the Jan Mayen ExPERT 50th humidity percentile atmosphere with GADS aerosols for a summer day between 1500 and 1800.
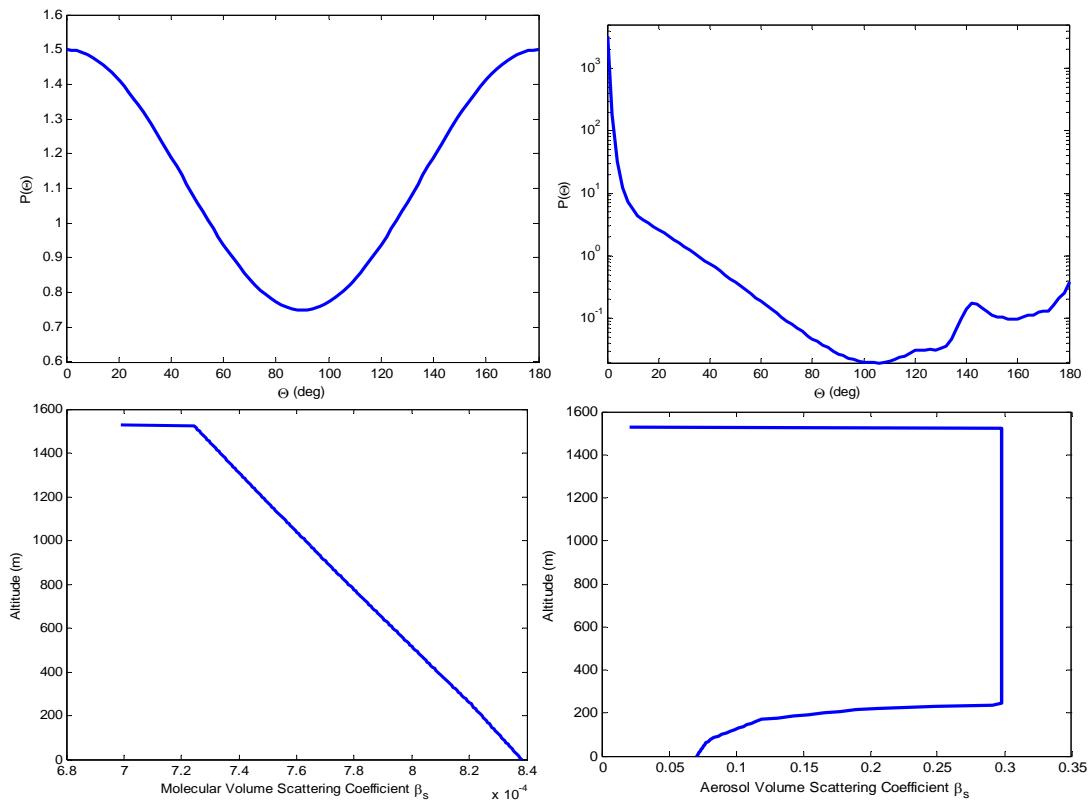
Figure 10. From left to right, top to bottom, molecular phase function, aerosol phase function, molecular volume scattering coefficient, and the aerosol volume scattering coefficient.

The incident irradiance I_0 in equation (3.9) is found by multiplying the laser power by the transmission to the center of each volume element and dividing by the beam

cross sectional area. In reality, the cross sectional irradiance in the beam will vary, often

modeled as a Gaussian. For this research, the beam did not need to be resolved as only

the total reflected irradiance was needed. The transmission to each segment center was

found using the equation,

$$\tau_a = e^{\int_{s_1}^{s_2} \beta_e(s)ds} ,$$
(3.10)

where $\beta_e(s)$ is the extinction coefficient at a specified distance s, and ds is the

differential length element. Once again, the extinction coefficients were interpolated

from the LEEDR-produced coefficients. A transmission from the platform to the gate

front was determined and then multiplied by the transmission from the gate front to each

of the segment centers. Multiplying these two transmissions together gave the

transmission from the platform to each segment center in the gate.

Because of the R^2 term in the denominator of equation (3.9), the size of the gate

has a large effect on the backscattered irradiance, especially if the gate is allowed to

extend the entire distance from the target. The plot in Figure 11 demonstrates the effect

the gate size has on the backscattered irradiance. It is created with an ExPERT site

atmosphere for a summer day between 1500-1800 local at Bucharest, Romania. The

platform is at an altitude of 1530 m with a 3 km slant path and a laser power of 100 W.

The exit aperture is 1 cm with a spot size at the target of 40 cm.
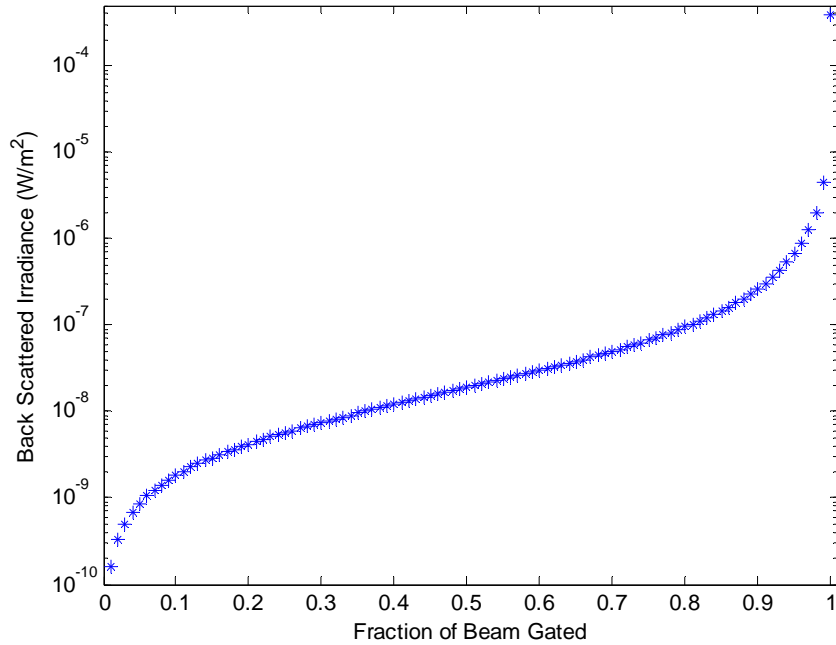
Figure 11. **The back scattered laser irradiance as a function of the fraction of the beam gated in front of the target.**

3.4.2 Solar Scatter Noise

It should be noted that only the single scatter is considered in this scenario and is

a good approximation for clear sky conditions. On the other hand, inside clouds,

radiation can scatter thousands of times within a very short distance. Equation (3.9) is

used in computing the solar scatter noise. The phase function and volume scattering

coefficient are once again interpolated from LEEDR but this time for the entire range

from the platform to the target. The range was segmented into 100 equally spaced

volume elements with a square cross sectional area at the segment centers determined by

the length of the side of the square detector and the receiver optics focal length. The

volume elements for the solar scatter are in fact the field of view volume modeled as a

pyramid broken into segments starting as a point at the platform and extending to a

square field of view area at the target. The incident irradiance is calculated by taking the

solar spectrum at the top of the atmosphere, integrating over the receiver bandwidth, and then multiplying by the path transmittance through the atmosphere to the segment centers. The 2 nm resolution American Society for Testing and Materials (ASTM) 2000 extraterrestrial solar spectra is used for the solar spectral irradiance at the top of the atmosphere and is shown in Figure 12. Note that at 1 μm, the solar irradiance is six times larger than that at 2 μm. With this information, the noise in our system from the sun is expected to be much less for the 2.039 μm as compared to the 1.0642 μm wavelength.
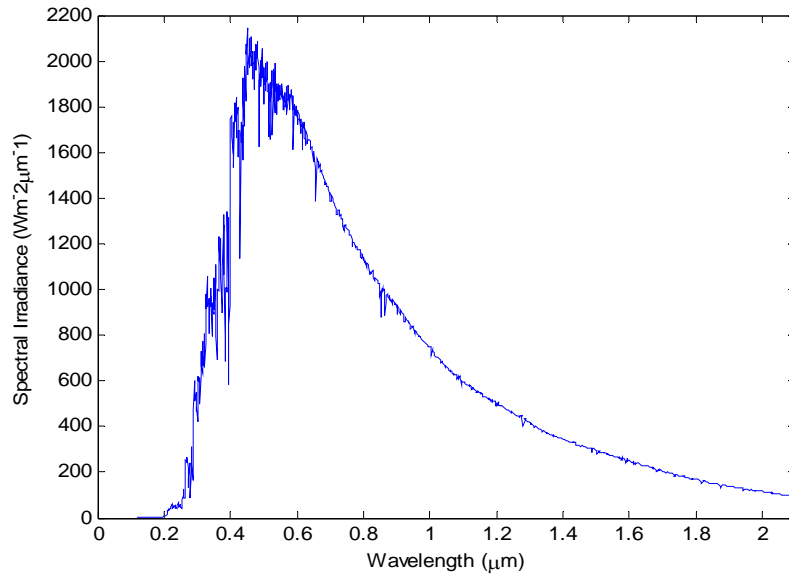
Figure 12. Spectral irradiance at the top of the atmosphere (ASTM 2000)

The following equation is used to find the incident solar irradiance,

$$I_{target\ solar} = \tau_a \int_{\lambda-\frac{BW}{2}}^{\lambda+\frac{BW}{2}} S(\lambda)d\lambda ,$$

(3.5)

where BW is the detector bandwidth and $S(\lambda)$ is the top of the atmosphere solar spectral irradiance. The ASTM solar spectrum is numerically integrated over the receiver bandwidth from ten equally spaced interpolated points within the bandwidth. After the

solar spectrum over the bandwidth is determined, it is then multiplied by the atmospheric transmission τ_a, which changes with the path length the radiation must travel through the atmosphere. Equation (3.4) is used to compute the transmission from the top of the atmosphere to the segment centers and the transmission from the segment centers to the receiver. The solar incident path lengths through the atmosphere are calculated from the sun's zenith angle using trigonometry from the center of the earth. One thousand atmospheric layers are created in the solar incident radiation calculation, interpolating the extinction coefficients from the LEEDR calculated extinction coefficients. Unlike the laser, the sun's irradiance does not change or spread because of the increase in the size of the volume element. In a vacuum, the sun equally illuminates the top and bottom of the atmosphere, mainly due to the sun's great distance from Earth.

3.4.3   Solar Reflection Noise

The solar reflection off the target is calculated the same way the signal is determined using equation (3.1). Looking at equation (3.1), the surface normal equation is now dependent upon the location of the sun (zero zenith for this study), dA is now the entire field of view, and the incident irradiance is now the incident solar radiation. The target reflectance is kept at 10%. The equation assumes that the target surface fills the entire field of view of the detector.

To find the incident solar irradiance, the solar spectral irradiance at the top of the atmosphere was integrated over the receiver bandwidth and multiplied by the LEEDR computed transmission through the atmosphere. Once again, the ASTM 2000 extraterrestrial solar spectra are used along with equation (3.5). The path length is ultimately determined from the solar zenith angle. The sun zenith angle has very little

52

effect on the transmission when the sun is overhead but as the sun drops further in the sky, the transmission begins to change more rapidly (see Figure 13). This is akin to taking a tape measure a few inches from perpendicular to the ceiling. Changing the angle of the tape measure increases the distance the tape measure must extend to touch the ceiling, with the greatest increases occurring at the higher angles.
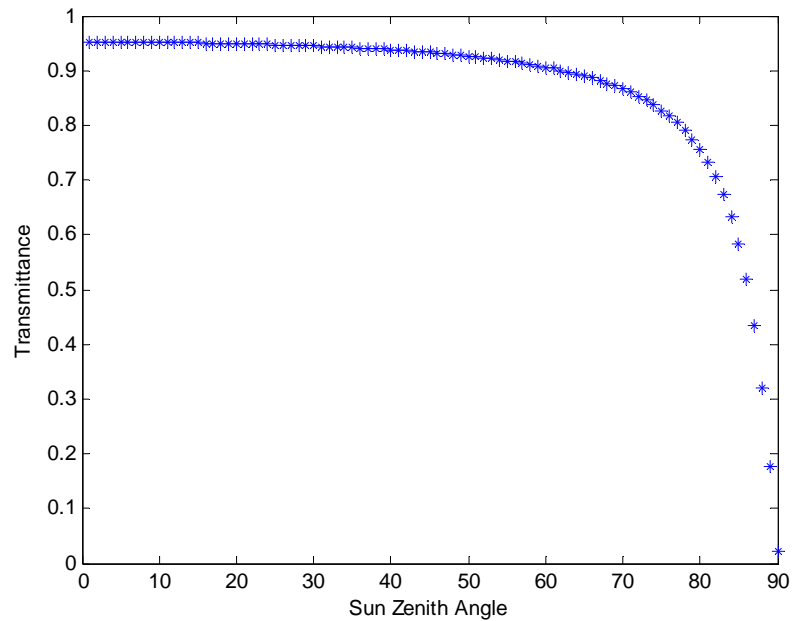
Figure 13. Solar transmittance as a function of sun zenith angle for the summer 1500-1800 50th humidity percentile LEEDR ExPERT atmosphere at Bucharest, Romania

3.4.4 Blackbody Noise

Any object that is not at absolute zero (K) radiates energy. This energy is the blackbody radiation and is determined by the equation,

$$I_{bb} = \frac{\tau_a FOV^2}{R^2} \int_{\lambda - \frac{BW}{2}}^{\lambda + \frac{BW}{2}} \frac{2hc^2}{\lambda^5 \left(e^{\frac{hc}{k_B \lambda T}} - 1 \right)} d\lambda \,, \tag{3.6}$$

where FOV is the linear field of view (m), h is Planck's constant (6.626 x 10^{-34} J s), c is

the speed of light (2.998 x 10^8 m/s), k_B is Boltzmann's constant (1.381 x 10^{-23} J/K), and T

is the objects temperature (K) (Petty 2006).

The temperature of the target for this analysis was assumed to be 300 K or about

80° F. For imperfect blackbody objects, the blackbody radiation is then multiplied by an

emissivity. For this study, the blackbody radiation without an emissivity proved to be

negligible because of the shorter wavelengths, narrow band, and low temperature. Figure

14 shows that blackbody emission nearly goes to zero for wavelengths shorter than 2.5

μm.
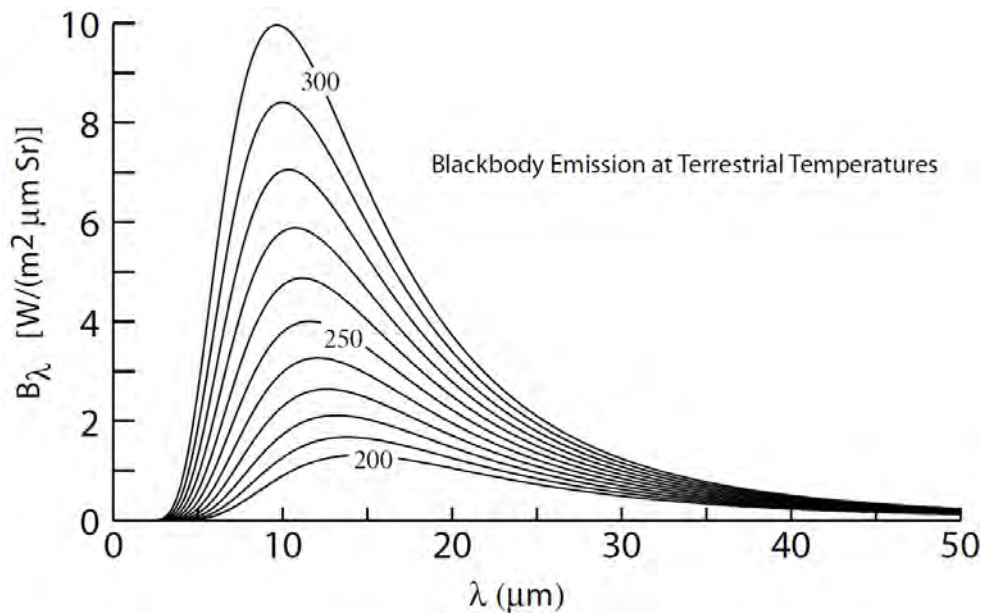
Figure 14. Black body curves for temperatures between 200 and 300 K (Petty 2006).

3.5 HELSEEM Images

HELSEEM returns pristine images in the form of a matrix containing irradiance

values for each pixel. The images are referred to as pristine as they contain no

atmospheric extinction or turbulence effects. In generating images to display atmospheric noise effects, the pristine image is used as the signal. The previously described methods are employed to compute noise. The HELSEEM code used is for an up-looking geometry, so the Matlab scripts for the down-looking signal and noise calculations were modified to be compatible for an up-looking engagement. A 3 km slant path with a target at 1530 m and a 50 km slant path with a target at 10 km at the Shanghai, China is examined. Atmospheric effects based on the ExPERT atmosphere with GADS aerosols are compared against the mid-latitude north standard atmosphere with MODTRAN urban aerosols. A comparison against using FASCODE transmissions for the signal propagation as well as a comparison against the ExPERT atmosphere with MODTRAN aerosols is executed.

One of the major differences between the down-looking geometries done previously for the global plots and the up-looking engagements here is that the solar scatter is no longer only the scattered sunlight in the field of view in front of the target, but also beyond the target. In order to incorporate the noise onto the signal matrix, both the signal and the noise are converted to radiance values in watts per meter squared per steradian. The image radiance values are found by dividing each pixel irradiance value in the image by its steradian value found by dividing the pixel area on the target by the squared range to the target. The computed noise irradiance is for the entire field of view so it is converted to radiance by dividing the field of view area by the squared range to the target. The solar reflection is computed in HELSEEM by doing a separate run in which the laser is off and only the sun's illumination creates the image.

Once the image and the noise are both in radiance units, each noise component is added. It is assumed that if the noise is greater than or equal to the signal, the signal is no longer visible. After the solar reflection is incorporated, the signal with the subtracted solar reflection is multiplied by the total path transmittance. The solar scatter behind the target is only added to all the zero signal image pixels because the RPA blocks all of the radiation directly behind it. The remaining noise is incorporated by adding the noise to every pixel with a value less than the previously added noise plus the current noise up to the total noise value. This process is illustrated in Figure 15. Imagine filling up a bathtub with an object in the middle; parts of the object slowly are submerged as the water level rises. When outputting the image, each pixel was divided by the noise resulting in units of signal-to-noise. This method assumes that no signal under a signal-to-noise ratio of one will be visible.

After all noise effects are accounted for, the image matrix of radiance values is fed into the Light-Tunneling within WaveTrain algorithm. LEEDR climatological winds and climatological turbulence profiles are used in the algorithm. The final image has atmospheric transmission, noise, and turbulence effects included.
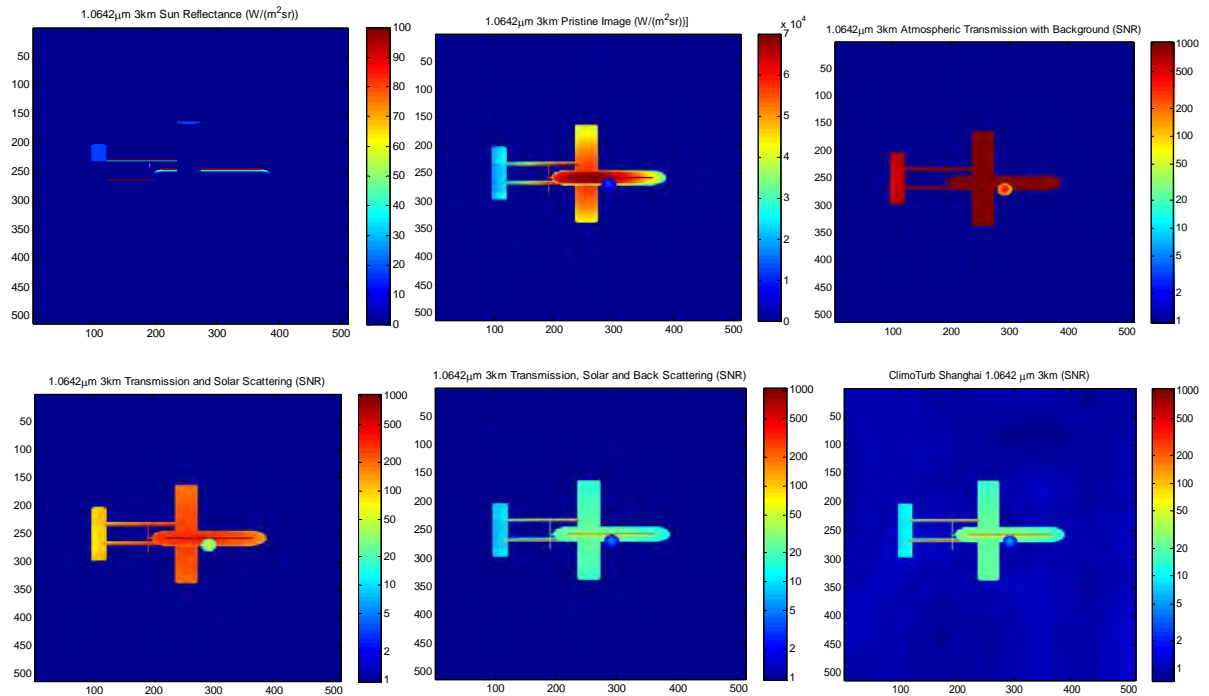
Figure 15. Progression of adding noise from left to right, top to bottom, the sun reflection, pristine image, background and transmission, solar scatter, laser backscatter, and finally the turbulence is added.

3.6   Summary

The method described here to show if LEEDR ExPERT atmospheres with GADS aerosols are advantageous to use in simulating LADAR over a standard atmosphere with a standard aerosol profile has two main parts. The two main parts are to produce signal-to-noise ratios for a Lambertian target, and then generate images to show signal-to-noise effects. Only atmospheric noise effects are considered in this study. Both parts are accomplished for ExPERT atmospheres with GADS aerosols and standard atmospheres with standard aerosols. By comparing the outputs from the two different atmospheres, the advantages of using ExPERT atmospheres with GADS aerosols are evident and will be shown in the next chapter.

IV   Analysis and Results

4.1   Chapter Overview

Global signal-to-noise ratios computed using LEEDR atmospheres are presented here as well as comparisons to standard profiles with standard aerosol distributions, and FASCODE transmissions. Images of an RPA displaying signal-to-noise is also shown displaying the difference between LADAR signal-to-noise for an ExPERT site as compared to a standard atmosphere profile. The reasons for the differences are discussed as well as the advantages that the probabilistic atmosphere approach brings to the LADAR modeling problem.

4.2   Results

4.2.1   World Wide Lambertian Target Signal-to-Noise Results

Figure 16 displays the resulting signal-to-noise ratios for the short range 3 km slant and vertical engagements from an altitude of 1530 m. The left global plots are for the slant path while the right global plots are for the vertical path. The scale was kept constant for all wavelengths for each geometry, making it easier to distinguish changes in the signal-to-noise ratios between different wavelengths. It was necessary to change the scale between geometries as the signal-to-noise ratios changed drastically. Because the scale was constant with a linear scale, many locations saturated the scale. This was necessary in order to keep the scale constant while seeing variations at the 1.0642 μm wavelength. The majority of contrast can be seen between the 1.0642 μm and 1.56 μm wavelengths for both geometries. In the 3km slant path geometry plots, several sites with signal-to-noise ratios hovering around 100 at the 1.0642 μm wavelength jump to over 500

at the 1.56 μm wavelength. Looking at the difference between the short range slant and vertical geometries at the 1.0642 μm wavelength, the signal-to-noise ratios are doubled for many locations while other locations remain almost the same. The major difference between locations is the aerosol profiles, and hence the signal-to-noise remains low regardless of the wavelength at locations with denser aerosols.
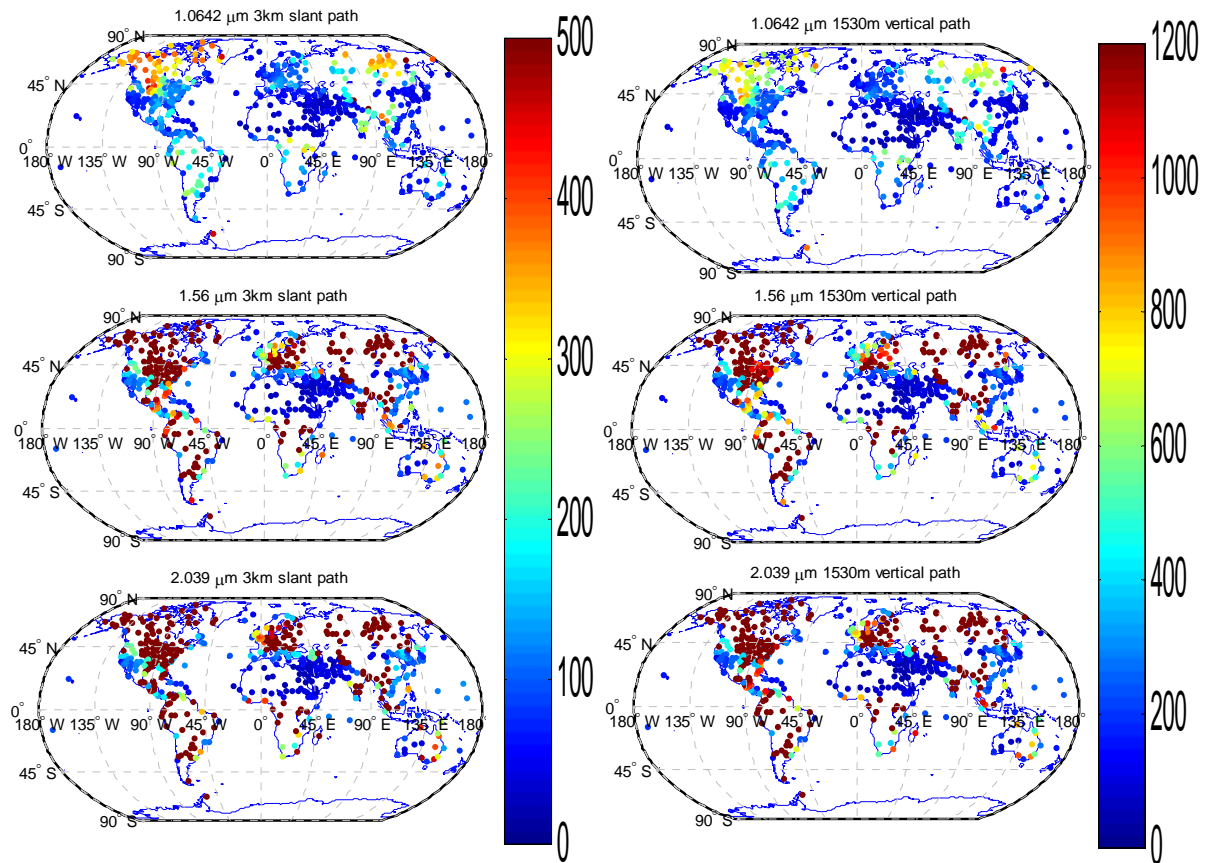
Figure 16. Short range slant path and vertical path signal-to-noise ratios for LEEDR ExPERT site atmospheres with GADS aerosols. The platform is at 1530 m altitude looking down at a target on the ground.

Figure 17 displays the resulting signal-to-noise ratios for the long range 50 km slant and vertical engagements from an altitude of 10 km. The left global plots are for the slant path while the right global plots are for the vertical path. Again, the scale was kept

constant for all wavelengths for each geometry. Notice that the scales are now 0 to 10 for the 50 km slant path and 0 to 100 for the vertical path. This is more than an order of magnitude smaller than the short range scale. Once again, the majority of contrast can be seen between the 1.0642 μm and 1.56 μm wave lengths for both geometries. Also, there are many regions of the world that remain to have a low signal-to-noise ratio regardless of the wavelength. These areas are desert and maritime locations. Maritime locations generally have larger wind speeds increasing aerosols in the air. Sea salt aerosols at these locations are also hygroscopic being allowed to swell in size with relative humidity. Desert locations also generally have higher wind speeds causing desert aerosols to become suspended in the air. Although these particles are not hygroscopic, they are generally smaller and denser than other regional aerosols.
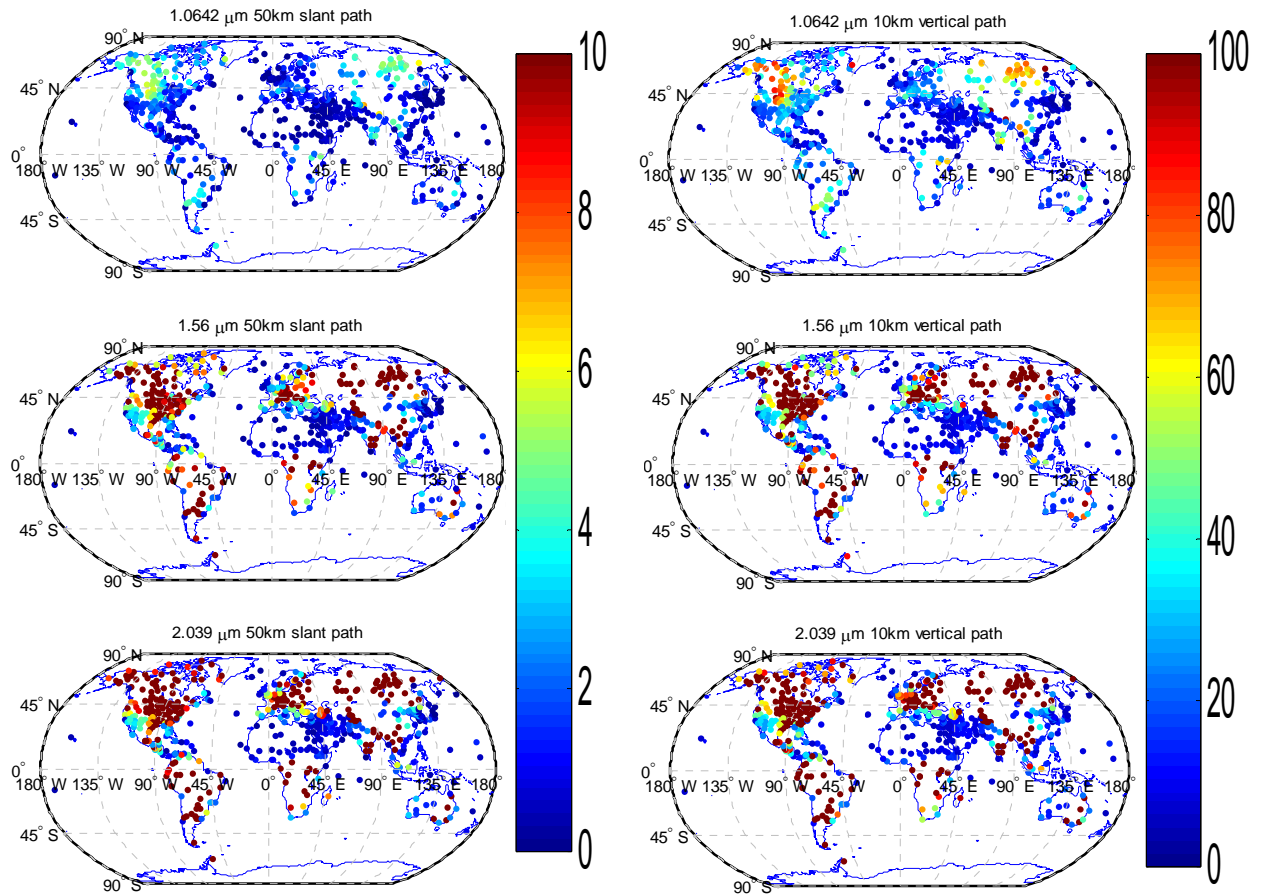
Figure 17. Long range slant path and vertical path signal-to-noise ratios for LEEDR ExPERT site atmospheres with GADS aerosols. The platform is at 10 km altitude looking down at a target on the ground.

While the global signal-to-noise ratio plots give great insight into atmospheric climatological conditions and locations that are ideal for LADAR usage, the purpose of this research is to identify advantages of using ExPERT atmospheres with GADS aerosols over standard atmosphere profiles with standard aerosol distributions. In order to accomplish this, the next charts are created to compare standard atmosphere and aerosol profile types with ten chosen ExPERT sites with the specified type of climate. The four standard atmospheres and their aerosol types chosen to study are the mid-latitude north with MODTRAN urban aerosols, mid-latitude north with MODTRAN rural

aerosols, desert with desert aerosols, and tropical with maritime tropical aerosols. Besides

the specified standard atmosphere and standard aerosol profile signal-to-noise ratios,

FASCODE values incorporating FASCODE transmissions are also included.

Table 2 gives insight into how FACODE transmissions change for different

aerosol types. The transmissions are created by using PLEXUS, which has a graphical

user interface to run FASCODE. In this study, the normal high visibility transmissions

are used except for the urban climate analysis in which case the normal low visibility

FASCODE transmissions are used. The urban low visibility transmissions are originally

thought to have values closer to the those found at urban ExPERT sites with GADS

aerosols.

Table 2. FASCODE transmissions for the different geometries, wavelengths and various aerosol types

	Aerosols	Short Range Slant (1.53km Alt 3km Range)			Short Range Vertical (1.53km Alt 1.53km Range)			Long Range Slant (10km Alt 50km Range)			Long Range Vertical (10km Alt 10km Range)		
		1.0642 µm	1.56 µm	2.039 µm	1.0642 µm	1.56 µm	2.039 µm	1.0642 µm	1.56 µm	2.039 µm	1.0642 µm	1.56 µm	2.039 µm
Normal High Visibility (23Km)	Urban	0.8511	0.9009	0.8613	0.9211	0.9481	0.9255	0.489	0.6437	0.5155	0.8657	0.915	0.8613
	Rural	0.8637	0.9163	0.8779	0.928	0.9564	0.9346	0.5149	0.6835	0.5513	0.8748	0.9261	0.8731
	Desert	0.8817	0.9368	0.8915	0.9378	0.9672	0.9419	0.5519	0.7367	0.5804	0.8871	0.9402	0.8822
	Maritime	0.7553	0.7879	0.7625	0.8667	0.8855	0.8698	0.3259	0.4075	0.3408	0.7974	0.8343	0.7921
Normal Low Visibility (5Km)	Urban	0.3771	0.5426	0.5977	0.6083	0.732	0.7679	6.76E-02	0.1812	0.2093	0.5728	0.707	0.7171
	Rural	0.4127	0.6022	0.672	0.6369	0.772	0.8152	8.43E-02	0.2384	0.2854	0.6014	0.7482	0.7642
	Desert	0.4682	0.6896	0.7383	0.6792	0.8273	0.8553	0.1154	0.3404	0.3654	0.6433	0.8045	0.8035
	Maritime	0.1812	0.2385	0.2831	0.4187	0.4813	0.5247	1.59E-02	2.64E-02	3.43E-02	0.3874	0.4553	0.4807

The FASCODE atmosphere type in the following charts is created by using the

standard atmosphere and aerosol types for the noise calculations and then using the

FASCODE transmissions for the signal calculations. Although this is not a fair

assessment of FASCODE, it does give insight into the effects using different total path

transmission values has on LADAR performance. The charts also contain the mean

absolute difference and the mean absolute percent difference for both the standard

atmosphere and FASCODE values. Although using the absolute difference does not give

any indication of systematic error greater or smaller than the ExPERT site values, it does give an indication to the variability of the values. This method of analysis is chosen as it is expected that the ExPERT values will vary greater and smaller than the standard atmosphere characterization, but how great this variability is shows the importance of using a probabilistic approach. The percent difference column is actually the ratio of the absolute mean difference divided by the standard atmosphere or FASCODE value. Transmissions were also included in the chart to analyze the degree of correlation between signal-to-noise ratio and transmission values.

From Table 3, urban ExPERT sites with GADS aerosols are relatively well described by the shorter 1.0642 μm wavelength standard profile having a mean absolute difference of about 25% for both the short range slant path and the vertical path but is relatively poor in describing the longer wavelengths. As expected, there does not seem to be a trend of higher or lower ExPERT values as compared to the standard atmosphere. The sites seem to be both evenly spread with greater and lower values, with greater variation at the two higher wavelengths. Analyzing the correlation between the transmissions and the signal-to-noise ratios shows there is no correlation when the ExPERT sites are compared to the standard atmosphere values at a specified wavelength.

Table 3. Mid-Latitude North standard atmosphere with MODTRAN urban aerosols for the short range slant and vertical path

Atm Type	3 km Slant Path						1530 m Vertical Path					
	1.0642 um SNR	1.56 um SNR	2.039 um SNR	1.0642 um T	1.56 um T	2.039 um T	1.0642 um SNR	1.56 um SNR	2.039 um SNR	1.0642 um T	1.56 um T	2.039 um T
MidLatNorthUrbanMod	116.54	361.95	889.31	0.4	0.62	0.71	240.46	729.22	1779.63	0.63	0.78	0.84
FASCODE Urban	101.76	280.28	628.19	0.38	0.54	0.6	224.8	640.17	1486.07	0.61	0.73	0.77
PITTSBURGH/GREATER	132.03	639.02	1201.42	0.81	0.9	0.89	261.04	1263.39	2380.85	0.9	0.95	0.94
CAMP SPRINGS/ANDREW	117.24	560.71	1035.56	0.77	0.88	0.88	231.88	1108.17	2051.01	0.88	0.94	0.94
BOSTON/LOGAN INTL	135.07	401.1	568.54	0.72	0.76	0.75	267.11	792.4	1124.19	0.85	0.87	0.86
LONDON/HEATHROW AIR	75.73	256.97	387.29	0.59	0.69	0.72	150.2	507.99	765.86	0.76	0.83	0.84
PARIS-ORLY	78.4	267.29	403.2	0.68	0.77	0.77	155.46	528.39	797.93	0.82	0.88	0.88
LUXEMBOURG/LUXEMBOU	112.49	541.92	1009.29	0.76	0.87	0.88	222.48	1070.87	1997.71	0.87	0.93	0.94
ZURICH-KLOTEN	147.35	726.2	1401.43	0.83	0.91	0.9	291.29	1436.62	2780.06	0.91	0.95	0.95
KYIV	105.87	514.54	967.83	0.72	0.85	0.87	209.47	1016.73	1915.22	0.84	0.92	0.93
SHANGHAI/HONGQIAO	47.31	89.89	101.02	0.47	0.55	0.54	93.92	177.84	200.59	0.68	0.73	0.73
PYONGYANG	63.33	144.31	170.21	0.61	0.76	0.78	125.33	284.69	336.6	0.77	0.87	0.88
Absolute Mean Std Atm Diff	28.17	190.11	398.53	0.29	0.19	0.12	59.25	373.08	789.97	0.2	0.11	0.07
Absolute Mean Std Atm Percent Diff	0.24	0.53	0.45	0.72	0.31	0.17	0.25	0.51	0.44	0.32	0.15	0.08
Absolute Mean FASCODE Diff	28.18	206.45	398.53	0.32	0.25	0.21	54.41	390.89	789.97	0.22	0.15	0.13
Absolute Mean FASCODE Percent Diff	0.28	0.74	0.63	0.84	0.46	0.35	0.24	0.61	0.53	0.36	0.21	0.17

Comparing the 1530 m to the 3 km path, the $1/r^2$ drop off that effects power is not present in the signal-to-noise ratio. Instead the signal-to-noise ratio is only halved for all the low altitude scenarios. Recalling the signal equation,

$$I_{signal} = \frac{P_t \rho_t dA \tau_a^2}{R^4 \pi^2 \theta_t^2},$$ (4.1)

The FOV is larger than the spot size at the target so $dA = \frac{\pi \theta_t^2 R^2}{4}$, which is just the spot size at the target. Plugging in dA yields the equation

$$I_{signal} = \frac{P_t \rho_t \tau_a^2}{4 \pi R^2}.$$ (4.2)

Only τ_a and R change between the 3 km and 1530 m path lengths. Examining the Mid-Latitude North standard atmosphere with MODTRAN urban aerosols at 1.0642 μm shows that the transmissions are .4 and .63 for the 3 km and 1530 m path lengths

respectfully. Dividing the 3 km path variables designated by subscript one by the 1530 m variables designated as subscript two,

$$\frac{\tau_{a_1}^2 R_2^2}{\tau_{a_2}^2 R_1^2},$$ (4.3)

yields a factor of about 9.5 increase in signal. This is shown by the signal in at the 3 km path of 0.0115 (W/m^2) and the signal at the 1530 m path of 0.1075 (W/m^2) making the actual factor about 9.4. The factor did not come out exactly as the transmission values were rounded. The same factor is found for the noise if laser backscatter is dominate which is calculated from

$$I_{Sca} = \tau_a \int \frac{P(\theta)\beta_{Sca} I_0}{4\pi R^2} dv,$$ (4.4)

where $I_0 = \frac{P_t \tau_a}{dA}$ and $dv = dA * dl$ which yields the equation

$$I_{Sca} = \tau_a^2 \int \frac{P_t P(\theta)\beta_{Sca}}{4\pi R^2} dl,$$ (4.5)

where $\boldsymbol{dl}$ is the differential path length element. Once again the variables that change from the 3 km to the 1530 m path are $\boldsymbol{\tau_a}$ and $\boldsymbol{R}$ which yields the same factor of about a 9.5 increase. This means the signal and laser scatter noise are exactly cancelling and the main difference is the number of bins. The number of bins is decreased by about half going from the 3 km range to the 1530 m range causing the noise to increase by about 4.25 instead. This is shown by the noise values in at the 3 km path of $\boldsymbol{9.9 * 10^{-5}}$ (W/m^2) and the noise at the 1530 m path of $4.\boldsymbol{47 * 10^{-4}}$ (W/m^2). The value is not exact as there are other noise contributions and the numbers were rounded in this demonstration. The above analysis also shows that once laser scatter becomes the dominate noise source and if the number of gate bins is kept constant, the signal-to-noise

ratios remains constant regardless of laser power or distance to the target. Notice from Table 4 that the solar scatter is dominant for the 50 km range and is reduced for the 10 km range as the field of view area in which sunlight can scatter has been reduced. Laser scatter becomes dominate at the 10 km range mainly due to the drastic increase in transmission from .02 to .48.

Table 4. Composition of noise components for 1.0642 μm Mid-Latitude North standard atmosphere with MODTRAN urban aerosols (W/m^2)

Path Length	Signal	Total Noise	Laser Scatter	Solar Reflection	Solar Scatter	Black Body
3000 m	0.011525	9.89E-05	9.81E-05	6.37E-07	1.5E-07	3.02E-19
1530 m	0.107511	4.47E-04	4.46E-04	9.93E-07	5.66E-08	2.4E-19
50 Km	1.43E-07	9.48E-06	1.36E-07	2.44E-07	9.1E-06	2.96E-19
10 Km	0.001448	5.71E-05	5.14E-05	4.92E-06	8.13E-07	1.19E-18

The values in the next chart are considerably higher as they are characterizations of rural environments which have far fewer aerosols. The signal-to-noise values are especially high for the two longer wavelengths with the standard atmosphere profile being more than an order of magnitude greater than the 1.0642 μm signal-to-noise ratio value. The ExPERT sites also display this increase but not to the same degree. Interestingly, though the mean difference for the signal-to-noise ratios are about 50% the transmissions are nearly identical only being about 5% different. Once again, this shows that though transmissions may be similar, the signal-to-noise ratios may have large differences.

The rest of the charts for the four climate types and both the short and long range engagement are shown below with a discussion at the end.

Table 5. Mid-Latitude North standard atmosphere with MODTRAN rural aerosols for the short range slant and vertical path

	3 km Slant Path						1530 m Vertical Path					
Atm Type	1.0642 um SNR	1.56 um SNR	2.039 um SNR	1.0642 um T	1.56 um T	2.039 um T	1.0642 um SNR	1.56 um SNR	2.039 um SNR	1.0642 um T	1.56 um T	2.039 um T
MidLatNorthRuralMod	142.94	1689.24	1931.11	0.87	0.95	0.93	283.06	3372.36	3837.15	0.93	0.97	0.96
FASCODE	139.83	1582.07	1727.96	0.86	0.92	0.88	279.95	3260.94	3616.3	0.93	0.96	0.93
MEDFORD-JACKSON COU	273.5	585.77	690.67	0.92	0.94	0.92	541.56	1157.49	1364.42	0.96	0.97	0.96
WATERLOO MUNICIPAL	114.55	533.73	957.24	0.74	0.86	0.86	226.55	1054.72	1895.33	0.85	0.92	0.93
GRIFFISS AFB/ROME	165.39	712.26	1186.83	0.86	0.93	0.9	326.89	1408.74	2351.79	0.93	0.96	0.95
GRAFENWOEHR	134.26	626.97	1130.09	0.81	0.9	0.89	265.44	1239.5	2238.95	0.9	0.95	0.94
NJANDOMA	174.44	738.74	1218.58	0.82	0.9	0.9	344.78	1461.25	2412.42	0.9	0.95	0.95
TUGULYM	154.79	676.19	1143.7	0.82	0.91	0.9	305.94	1336.97	2264.13	0.91	0.95	0.95
NIZHNEUDINSK	275.68	1129.41	1841.05	0.89	0.94	0.93	545.34	2240.58	3654.47	0.94	0.97	0.96
ZEJA	312.79	1406.03	2554.53	0.9	0.95	0.94	619.05	2795.72	5087.33	0.95	0.97	0.97
ALDAN	329.98	1474.37	2656.58	0.92	0.96	0.94	653.18	2933.34	5293.95	0.96	0.98	0.97
VITIM	323.33	1446.59	2612.28	0.92	0.96	0.94	639.95	2877.33	5207.19	0.96	0.98	0.97
Absolute Mean Std Atm Diff	90.34	756.24	737.97	0.05	0.03	0.02	178.64	1521.8	1475.56	0.03	0.02	0.01
Absolute Mean Std Atm Percent Diff	0.63	0.45	0.38	0.06	0.03	0.03	0.63	0.45	0.38	0.03	0.02	0.01
Absolute Mean FASCODE Diff	92.21	649.07	679.33	0.05	0.03	0.04	180.5	1410.37	1394.85	0.03	0.02	0.02
Absolute Mean FASCODE Percent Diff	0.66	0.41	0.39	0.06	0.03	0.04	0.64	0.43	0.39	0.03	0.02	0.02

Table 6. Desert standard atmosphere with desert aerosols for the short range slant and vertical path

	3 km Slant Path						1530 m Vertical Path					
Atm Type	1.0642 um SNR	1.56 um SNR	2.039 um SNR	1.0642 um T	1.56 um T	2.039 um T	1.0642 um SNR	1.56 um SNR	2.039 um SNR	1.0642 um T	1.56 um T	2.039 um T
DesertDesert	31.18	26.26	22.42	0.63	0.65	0.64	62.57	52.58	44.93	0.79	0.8	0.8
FASCODE	61.04	54.66	43.42	0.88	0.94	0.89	88.22	76.47	62.83	0.94	0.97	0.94
NELLIS AFB	72.78	122.21	121.81	0.86	0.88	0.87	143.93	241.27	240.57	0.93	0.94	0.93
WHITE SANDS	72.81	124.44	124.85	0.86	0.88	0.86	143.97	245.63	246.71	0.93	0.94	0.93
EL-GOLEA	25.26	21.04	17.57	0.57	0.59	0.59	50.95	42.34	35.35	0.75	0.76	0.77
TAMANRASSET	35.48	29.79	24.99	0.67	0.68	0.69	71	59.51	49.88	0.81	0.82	0.83
FAYA	31.18	26.18	21.92	0.63	0.65	0.65	62.57	52.43	43.9	0.79	0.8	0.8
WADI HALFA	30.15	25.35	21.22	0.62	0.64	0.64	60.54	50.79	42.53	0.78	0.8	0.8
AL-MADINAH	38.9	32.96	27.69	0.69	0.71	0.71	77.73	65.71	55.21	0.83	0.84	0.84
TEHRAN-MEHRABAD	24.16	37.67	42.06	0.7	0.73	0.73	48.21	75	83.77	0.83	0.85	0.85
FARAH	45.02	38.46	32.28	0.72	0.74	0.72	89.74	76.53	64.35	0.85	0.86	0.85
KANDAHAR AIRPORT	68.36	60.65	51.6	0.81	0.83	0.81	135.59	120.04	102.25	0.9	0.91	0.9
Absolute Mean Std Atm Diff	16.02	26.86	27.49	0.1	0.1	0.1	31.45	52.78	54.12	0.06	0.06	0.06
Absolute Mean Std Atm Percent Diff	0.51	1.02	1.23	0.15	0.15	0.15	0.5	1	1.2	0.07	0.07	0.07
Absolute Mean FASCODE Diff	22.8	31.45	28.42	0.17	0.2	0.16	31.87	49.06	51.08	0.1	0.12	0.09
Absolute Mean FASCODE Percent Diff	0.37	0.58	0.65	0.19	0.22	0.18	0.36	0.64	0.81	0.11	0.12	0.1

Table 7. Tropical standard atmosphere with maritime tropical aerosols for the short range slant and vertical path

Atm Type	3 km Slant Path						1530 m Vertical Path					
	1.0642 um SNR	1.56 um SNR	2.039 um SNR	1.0642 um T	1.56 um T	2.039 um T	1.0642 um SNR	1.56 um SNR	2.039 um SNR	1.0642 um T	1.56 um T	2.039 um T
Tropical MaritimeTropical	22.21	28.34	30.43	0.66	0.7	0.68	44.57	56.69	61.07	0.81	0.83	0.82
FASCODE	28.99	35.96	38.82	0.76	0.79	0.76	51.1	64.05	69.02	0.87	0.89	0.87
LIHUE/KAUAI ISLAND	48.43	73.59	79.86	0.5	0.5	0.46	95.76	145.24	158.33	0.7	0.7	0.67
PAGO PAGO/INT.AIRP.	67.24	95.11	101.26	0.58	0.57	0.5	132.88	187.69	201.21	0.76	0.75	0.71
GUANTANAMO BAY NAS	64.91	105.09	110.95	0.69	0.7	0.64	128.16	207.17	219.85	0.82	0.83	0.79
SAN JUAN INTL ARPT	53.99	79.38	78.53	0.66	0.66	0.6	106.74	156.73	155.96	0.81	0.81	0.77
BERMUDA INTERNATION	74.25	117.86	129.82	0.63	0.64	0.59	146.54	232.21	256.95	0.79	0.8	0.76
GRANTLEY ADAMS	40.48	54.46	51.84	0.59	0.59	0.53	80.25	107.86	103.35	0.76	0.76	0.72
LAJES (ACORES)	57.6	88.71	97.03	0.55	0.55	0.52	113.76	174.87	191.73	0.73	0.74	0.72
SEYCHELLES INTERNAT	78.95	111.71	119.06	0.62	0.62	0.55	155.93	220.3	236.41	0.79	0.78	0.74
DIEGO GARCIA	68.71	97.52	103.94	0.59	0.58	0.51	135.77	192.42	206.47	0.76	0.76	0.71
KWAJALEIN/BUCHOLZ A	76.76	109.97	117.44	0.62	0.62	0.54	151.61	216.88	233.25	0.78	0.78	0.73
Absolute Mean Std Atm Diff	**40.92**	**65**	**68.55**	**0.06**	**0.1**	**0.13**	**80.17**	**127.44**	**135.28**	**0.04**	**0.06**	**0.09**
Absolute Mean Std Atm Percent Diff	**1.84**	**2.29**	**2.25**	**0.1**	**0.14**	**0.19**	**1.8**	**2.25**	**2.22**	**0.05**	**0.07**	**0.11**
Absolute Mean FASCODE Diff	**34.14**	**57.38**	**60.16**	**0.15**	**0.18**	**0.22**	**73.64**	**120.09**	**127.33**	**0.1**	**0.11**	**0.14**
Absolute Mean FASCODE Percent Diff	**1.18**	**1.6**	**1.55**	**0.2**	**0.23**	**0.29**	**1.44**	**1.87**	**1.84**	**0.11**	**0.13**	**0.16**

Table 8. Mid-Latitude North standard atmosphere with MODTRAN urban aerosols for the long range slant and vertical path

Atm Type	50 km Slant Path						10 km Slant Path					
	1.0642 um SNR	1.56 um SNR	2.039 um SNR	1.0642 um T	1.56 um T	2.039 um T	1.0642 um SNR	1.56 um SNR	2.039 um SNR	1.0642 um T	1.56 um T	2.039 um T
MidLatNorthUrbanMod	0.02	1.49	9.42	0.02	0.14	0.24	25.36	88.69	220.81	0.48	0.68	0.75
FASCODE	0.12	2.41	7.65	0.07	0.18	0.21	35.95	96.48	201.63	0.57	0.71	0.72
PITTSBURGH/GREATER	1.91	11.24	21.14	0.46	0.7	0.64	29.71	136.66	258.02	0.86	0.93	0.92
CAMP SPRINGS/ANDREW	1.53	9.98	19.03	0.4	0.65	0.6	26.35	121.9	227.55	0.83	0.92	0.9
BOSTON/LOGAN INTL	1.34	5.44	8.69	0.34	0.44	0.39	27.76	77.95	109.44	0.81	0.85	0.83
LONDON/HEATHROW AIR	0.44	3.36	6.73	0.17	0.32	0.33	16.62	55.62	84.11	0.71	0.8	0.8
PARIS-ORLY	0.75	4.53	8.09	0.25	0.41	0.4	17.94	60.39	91.2	0.76	0.84	0.83
LUXEMBOURG/LUXEMBOU	1.41	9.61	19.17	0.38	0.63	0.61	25.17	117.67	222.01	0.82	0.91	0.91
ZURICH-KLOTEN	2.18	12.21	22.71	0.5	0.72	0.65	32.93	151.68	291.12	0.87	0.94	0.92
KYIV	1.11	8.66	18.08	0.32	0.58	0.58	23.18	110.34	210.63	0.8	0.9	0.9
SHANGHAI/HONGQIAO	0.12	0.64	0.88	0.09	0.16	0.14	6.09	11.36	13.61	0.63	0.7	0.68
PYONGYANG	0.36	2.11	3.25	0.2	0.41	0.41	7.48	20.36	28.44	0.73	0.84	0.84
Absolute Mean Std Atm Diff	**1.1**	**5.46**	**7.25**	**0.29**	**0.36**	**0.26**	**7.1**	**41.26**	**90.29**	**0.3**	**0.18**	**0.11**
Absolute Mean Std Atm Percent Diff	**72.95**	**3.66**	**0.77**	**12.16**	**2.62**	**1.08**	**0.28**	**0.47**	**0.41**	**0.64**	**0.27**	**0.15**
Absolute Mean FASCODE Diff	**1**	**4.78**	**7.54**	**0.24**	**0.32**	**0.28**	**14.62**	**41.26**	**88.25**	**0.21**	**0.16**	**0.14**
Absolute Mean FASCODE Percent Diff	**8.52**	**1.98**	**0.99**	**3.61**	**1.79**	**1.33**	**0.41**	**0.43**	**0.44**	**0.36**	**0.22**	**0.2**

Table 9. Mid-Latitude North standard atmosphere with MODTRAN rural aerosols for the long range slant and vertical path

Atm Type	50 km Slant Path						10 km Vertical Path					
	1.0642 um SNR	1.56 um SNR	2.039 um SNR	1.0642 um T	1.56 um T	2.039 um T	1.0642 um SNR	1.56 um SNR	2.039 um SNR	1.0642 um T	1.56 um T	2.039 um T
MidLatNorthRuralMod	2.38	17.6	28.67	0.54	0.8	0.71	36.34	309.33	412.47	0.89	0.96	0.93
FASCODE	2.18	14.35	20.46	0.51	0.68	0.55	35.49	293.9	367.62	0.87	0.93	0.87
MEDFORD-JACKSON COU	3.76	11.36	16.23	0.65	0.75	0.66	61.88	135.54	169.37	0.92	0.95	0.92
WATERLOO MUNICIPAL	1.29	9.05	17.74	0.35	0.6	0.58	24.99	114.26	209.42	0.81	0.9	0.9
GRIFFISS AFB/ROME	2.63	12.68	21.46	0.56	0.76	0.65	37.49	153.61	262.88	0.89	0.95	0.92
GRAFENWOEHR	1.9	11.04	20.46	0.46	0.69	0.63	30.15	134.92	246.74	0.86	0.93	0.91
NJANDOMA	2.24	11.89	22.31	0.49	0.71	0.69	37.03	151.8	261.9	0.87	0.93	0.93
TUGULYM	2.19	11.67	21.04	0.49	0.71	0.65	34.43	144.64	252.25	0.87	0.94	0.92
NIZHNEUDINSK	3.71	15.73	27.12	0.65	0.82	0.73	56.66	214.69	366.36	0.92	0.96	0.94
ZEJA	3.95	17.02	30.06	0.68	0.85	0.75	61.52	244.65	449.68	0.93	0.97	0.94
ALDAN	4.46	17.99	31.54	0.72	0.88	0.78	67.2	260.92	475.09	0.94	0.97	0.95
VITIM	4.36	17.85	30.24	0.72	0.87	0.74	66.19	257.96	468.41	0.94	0.97	0.94
Absolute Mean Std Atm Diff	**1.05**	**4.1**	**6.02**	**0.11**	**0.08**	**0.06**	**15.3**	**128.03**	**127.41**	**0.03**	**0.02**	**0.02**
Absolute Mean Std Atm Percent Diff	**0.44**	**0.23**	**0.21**	**0.2**	**0.1**	**0.08**	**0.42**	**0.41**	**0.31**	**0.04**	**0.02**	**0.02**
Absolute Mean FASCODE Diff	**1.1**	**2.96**	**4.75**	**0.12**	**0.1**	**0.13**	**15.64**	**112.6**	**109.48**	**0.04**	**0.03**	**0.05**
Absolute Mean FASCODE Percent Diff	**0.5**	**0.21**	**0.23**	**0.22**	**0.14**	**0.24**	**0.44**	**0.38**	**0.3**	**0.04**	**0.03**	**0.06**

Table 10. Desert standard atmosphere with Desert aerosols for the long range slant and vertical path

Atm Type	50 km Slant Path						10 km Vertical Path					
	1.0642 um SNR	1.56 um SNR	2.039 um SNR	1.0642 um T	1.56 um T	2.039 um T	1.0642 um SNR	1.56 um SNR	2.039 um SNR	1.0642 um T	1.56 um T	2.039 um T
DesertDesert	0.11	0.29	0.34	0.08	0.1	0.09	8.01	6.97	5.97	0.6	0.63	0.62
FASCODE	3.84	11.94	11.79	0.55	0.74	0.58	17.14	15.56	12.15	0.89	0.94	0.88
NELLIS AFB	1.63	3.9	4.46	0.5	0.58	0.53	19.43	33.74	34.31	0.87	0.9	0.88
WHITE SANDS	1.68	4	4.49	0.52	0.6	0.53	19.3	34.2	34.97	0.88	0.9	0.88
EL-GOLEA	0.04	0.12	0.19	0.04	0.05	0.06	6.33	5.44	4.59	0.54	0.56	0.58
TAMANRASSET	0.18	0.42	0.53	0.1	0.13	0.14	9.2	7.99	6.79	0.64	0.66	0.68
FAYA	0.1	0.28	0.37	0.08	0.1	0.1	7.99	6.94	5.86	0.6	0.63	0.64
WADI HALFA	0.09	0.25	0.33	0.07	0.09	0.09	7.7	6.7	5.65	0.59	0.62	0.63
AL-MADINAH	0.45	0.75	0.74	0.2	0.24	0.23	10.19	8.93	7.58	0.73	0.75	0.74
TEHRAN-MEHRABAD	0.33	0.82	1.07	0.22	0.27	0.27	6.41	10.25	11.53	0.74	0.77	0.77
FARAH	0.62	0.98	0.89	0.25	0.29	0.26	11.86	10.51	8.84	0.76	0.78	0.76
KANDAHAR AIRPORT	0.98	1.74	1.74	0.3	0.35	0.35	18.07	16.87	14.5	0.79	0.81	0.81
Absolute Mean Std Atm Diff	**0.52**	**1.08**	**1.17**	**0.16**	**0.18**	**0.17**	**4.36**	**7.56**	**7.85**	**0.13**	**0.13**	**0.13**
Absolute Mean Std Atm Percent Diff	**4.77**	**3.77**	**3.48**	**2.04**	**1.92**	**1.96**	**0.54**	**1.08**	**1.31**	**0.21**	**0.2**	**0.21**
Absolute Mean FASCODE Diff	**3.22**	**10.61**	**10.31**	**0.32**	**0.47**	**0.32**	**6.57**	**9.03**	**8.16**	**0.17**	**0.2**	**0.15**
Absolute Mean FASCODE Percent Diff	**0.84**	**0.89**	**0.87**	**0.59**	**0.63**	**0.56**	**0.38**	**0.58**	**0.67**	**0.2**	**0.21**	**0.16**

Table 11. Tropical standard atmosphere with maritime tropical aerosols for the long range slant and vertical path

Atm Type	50 km Slant Path						10 km Vertical Path					
	1.0642 um SNR	1.56 um SNR	2.039 um SNR	1.0642 um T	1.56 um T	2.039 um T	1.0642 um SNR	1.56 um SNR	2.039 um SNR	1.0642 um T	1.56 um T	2.039 um T
TropicalMaritimeTropical	0.35	0.74	0.78	0.2	0.26	0.22	5.82	8.15	8.8	0.73	0.77	0.74
FASCODE	0.87	1.69	1.8	0.33	0.41	0.34	6.99	9.59	10.01	0.8	0.83	0.79
LIHUE/KAUAI ISLAND	0.19	0.43	0.41	0.12	0.13	0.09	3.7	6.17	6.42	0.66	0.67	0.63
PAGO PAGO/INT.AIRP.	0.29	0.57	0.47	0.19	0.21	0.13	4.1	6.75	7.03	0.72	0.73	0.67
GUANTANAMO BAY NAS	1.01	2.41	2.21	0.29	0.34	0.23	13.8	22.42	21.94	0.79	0.81	0.75
SAN JUAN INTL ARPT	0.63	1.39	1.16	0.25	0.28	0.18	8.34	13.69	12.95	0.76	0.78	0.72
BERMUDA INTERNATION	0.48	1.06	0.99	0.25	0.28	0.21	5.97	10.33	10.91	0.76	0.78	0.73
GRANTLEY ADAMS	0.3	0.62	0.51	0.17	0.19	0.12	4.76	7.69	7.56	0.71	0.72	0.66
LAJES (ACORES)	0.26	0.58	0.61	0.16	0.18	0.15	4.2	7.04	7.56	0.7	0.71	0.68
SEYCHELLES INTERNAT	0.38	0.74	0.61	0.24	0.26	0.16	4.76	7.88	8.26	0.75	0.77	0.7
DIEGO GARCIA	0.3	0.6	0.5	0.2	0.21	0.13	4.22	6.96	7.26	0.73	0.74	0.67
KWAJALEIN/BUCHOLZ A	0.38	0.76	0.62	0.24	0.26	0.16	4.84	8.02	8.35	0.75	0.76	0.69
Absolute Mean Std Atm Diff	**0.15**	**0.36**	**0.37**	**0.04**	**0.05**	**0.07**	**2.08**	**2.85**	**2.85**	**0.03**	**0.03**	**0.05**
Absolute Mean Std Atm Percent Diff	**0.44**	**0.48**	**0.48**	**0.21**	**0.19**	**0.3**	**0.36**	**0.35**	**0.32**	**0.04**	**0.04**	**0.07**
Absolute Mean FASCODE Diff	**0.48**	**0.92**	**1.07**	**0.11**	**0.17**	**0.18**	**2.75**	**3.43**	**3.34**	**0.06**	**0.09**	**0.1**
Absolute Mean FASCODE Percent Diff	**0.55**	**0.54**	**0.6**	**0.35**	**0.43**	**0.54**	**5.82**	**8.15**	**8.8**	**0.73**	**0.77**	**0.74**

The short range geometries in desert environments, Table 6, clearly show that both the signal-to-noise ratios and the transmissions are lower than for the previous two tables. As discussed earlier, desert environments provide the ideal scenario in which dust can be lifted into the atmosphere. Deserts have loose fine particles in the 50 to 200 μm range and regularly have surface winds above 0.2 m/s meeting the criterion to inject dust into the atmosphere. Desert regions are the atmosphere's main source of suspended dust particles (Wallace and Hobbs 2006). Unlike the mid-latitude standard profiles, transmissions are very strongly correlated to the signal-to-noise for the desert climate. Faya, Chad has the same transmission as the standard atmosphere with a value of 0.63. Interestingly, their signal-to-noise ratios also exactly match. This can be explained from the fact that the major difference between the ExPERT atmospheres and the standard atmospheres is the allowance of aerosols to swell with height. In desert environments,

70

the air is so dry that there is not enough moisture in the air for this to happen, and hence the standard and ExPERT profiles will look very similar. The composition of absorption and scattering due to molecules and aerosols will also be similar as desert aerosols have very little absorption.

In Table 8 the long range urban standard atmosphere, there was great dissimilarity from the ExPERT atmospheres for the 1.0642 μm wavelength being on average almost 73 times too small. That is a 7300 percent difference. Surprisingly, at the 2.039 μm wavelength, there was a great reduction in this number to a mean percent difference of 77. Of the locations analyzed, Shanghai, China had the worst transmissions and signal-to-noise ratios. The long range rural signal-to-noise ratios again are larger than the urban case. The standard atmosphere is tolerable in characterizing the ExPERT sites for this case, having a mean percent difference of about 20 for the two longer wavelengths. In Table 10, the long range desert climate assessments, the transmissions are once again very well correlated to the signal-to-noise ratios for both the slant and the vertical geometries. In the last chart, the long range tropical environments, the mean standard percent difference remained nearly constant across the three wavelengths for both the slant and vertical geometries. This was a result of the profiles scaling the same between the different wavelengths. Because the maritime tropical aerosols are mainly sea salt, this showed that both the standard atmosphere and the ExPERT atmosphere scaled these aerosols very nearly the same, though the ExPERT atmosphere let them swell with altitude.

The transmission does not always correlate to the signal-to-noise ratio. This is demonstrated by looking at the 2.039 μm wavelength 3 km urban signal-to-noise values

in Figure 18. The plots display the effect the uncorrelated noise for various atmosphere profiles have on the signal-to-noise ratio. Because the noise is uncorrelated for various atmosphere profiles, the signal-to-noise ratio is likewise uncorrelated. The shorter two wavelengths shows a similar uncorrelation to a lesser extent. The main cause for signal-to-noise not to be correlated is that different atmospheric profiles have different absorption and scattering profiles. The absorption causes a loss of transmission with no increased noise, while scattering causes a loss of transmission and an increase in noise.

Figure 18. Signal-to-noise ratio correlation at 2.039 μm wavelength 3 km range for the Mid-Latitude North urban simulations. From left to right is the signal, noise, and signal-to-noise plotted against transmission. The x marks the standard profile value and the o marks the FASCODE value.

Transmission will correlate with signal-to-noise ratios for profiles in which there is no absorption. Desert environment profiles have virtually no absorption and there is very little difference within the boundary layer because desert aerosols are not hygroscopic. Because of the noise correlation as seen in Figure 19 the signal-to-noise was also correlated. The FASCODE values did not correlate because the signal was produced using the FASCODE transmissions while the noise was calculated from the

standard profiles. The other two wavelengths for the desert simulations also show
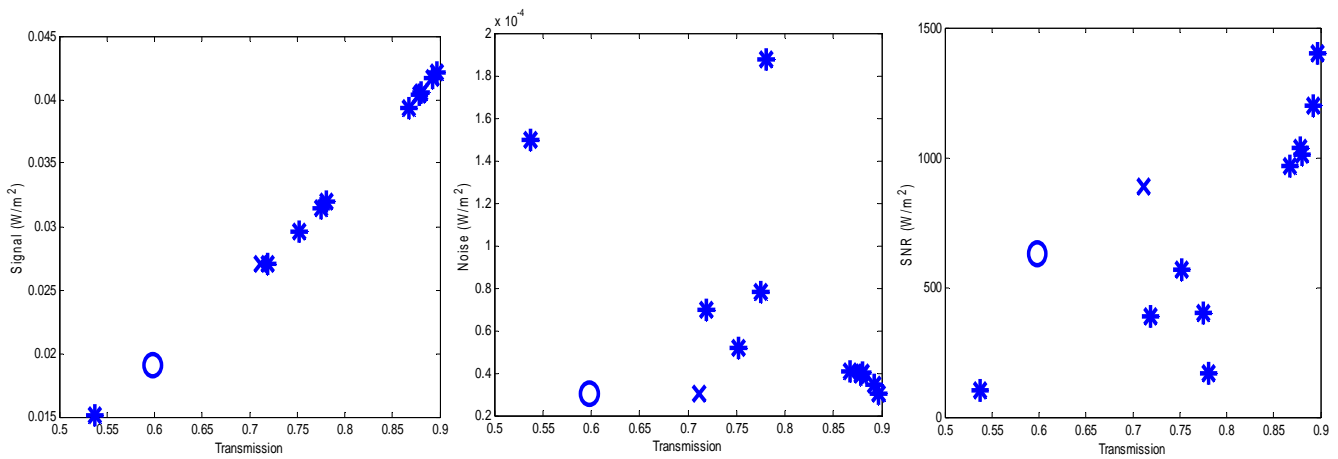
correlation, but not to the same extent.
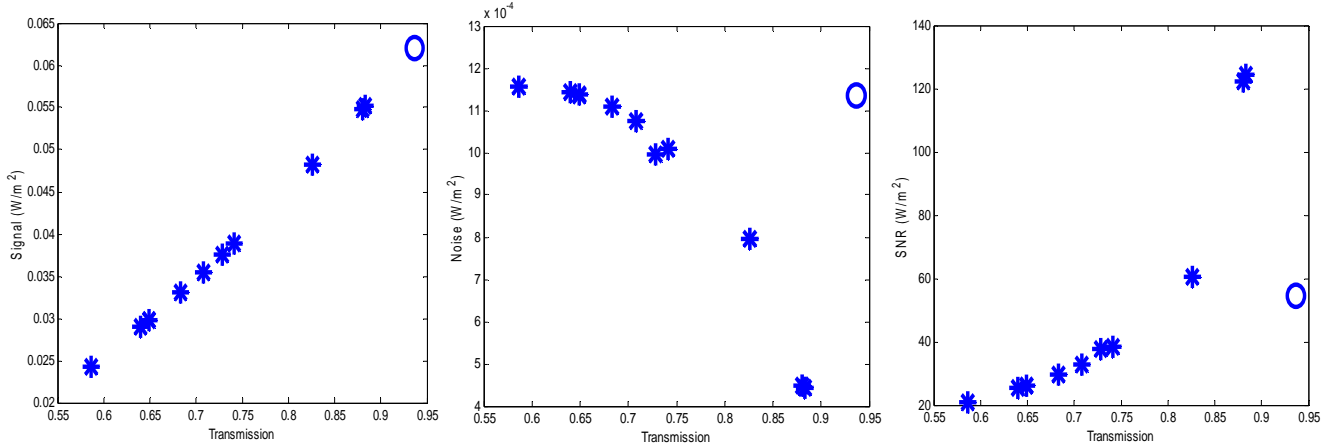
Figure 19. Signal-to-noise ratio correlation at 1.56 μm wavelength 3 km range for desert simulations. From left to right is the signal, noise, and signal-to-noise plotted against transmission. The x marks the standard profile value and the o marks the FASCODE value.

The previous data tables displayed the variability between ExPERT site

atmospheres with GADS aerosols to standard atmosphere assessments. The below charts

were created to narrow down the variables and analyze the effect ExPERT atmospheres

have on standard aerosol models. In order to accomplish this, LADAR performance was

analyzed with the previously chosen ExPERT sites for the urban climate environment but

this time in conjunction with the MODTRAN urban aerosol profile. From the below

charts, it is apparent that the ExPERT atmospheres, which allow aerosols to swell with

the increase in relative humidity with altitude, have a significant effect. There was a

much greater effect for the longer shallower 50 km geometry than the shorter 3 km slant

path. Even though the mean signal-to-noise ratio difference was in the single digits, the 3

km slant path clearly displayed a reduction in transmission when the aerosols were

allowed to swell with relative humidity. The small effect seen at the 1530 m altitude can

73

be explained from the fact that the 10% gate starts at 153 m above the ground where both

the ExPERT and standard profiles are nearly identical. The total transmission has little

effect on the signal-to-noise ratio as can be seen from Pyongyang, which has only a 7%

transmission, yet only a slightly lower signal-to-noise ratio than the standard profile.

Table 12. North standard atmosphere with MODTRAN urban aerosols for the short range slant and vertical path

	3 km Slant Path						1530 m Vertical Path					
Atm Type	1.0642 um SNR	1.56 um SNR	2.039 um SNR	1.0642 um T	1.56 um T	2.039 um T	1.0642 um SNR	1.56 um SNR	2.039 um SNR	1.0642 um T	1.56 um T	2.039 um T
MidLatNorthUrbanMod	116.54	361.95	889.31	0.4	0.62	0.71	240.46	729.22	1779.63	0.63	0.78	0.84
FASCODE	101.76	280.28	628.19	0.38	0.54	0.6	224.8	640.17	1486.07	0.61	0.73	0.77
PITTSBURGH/GREATER	124.97	397.23	827.24	0.23	0.46	0.6	259.52	801.66	1656.2	0.47	0.67	0.77
CAMP SPRINGS/ANDREW	123.35	392.98	823.83	0.21	0.44	0.59	256.57	793.18	1649.4	0.45	0.66	0.76
BOSTON/LOGAN INTL	116.24	374.68	835.83	0.12	0.33	0.5	246.27	756.93	1672.03	0.34	0.56	0.7
LONDON/HEATHROW AIR	120.35	385.09	824.06	0.16	0.38	0.55	251.86	777.57	1648.72	0.39	0.61	0.74
PARIS-ORLY	124.56	396.38	825.13	0.23	0.47	0.61	258.58	799.92	1652.36	0.47	0.68	0.77
LUXEMBOURG/LUXEMBOU	123.61	393.63	826.06	0.2	0.43	0.58	257.34	794.58	1653.19	0.44	0.65	0.76
ZURICH-KLOTEN	125.14	397.5	827.58	0.23	0.46	0.61	259.82	802.22	1657.02	0.47	0.68	0.77
KYIV	121	386.51	824.39	0.17	0.39	0.55	252.92	780.36	1649.5	0.4	0.62	0.74
SHANGHAI/HONGQIAO	107.09	354.16	883.81	0.08	0.26	0.42	235.75	716.5	1773.63	0.27	0.5	0.64
PYONGYANG	104.05	350.03	890.63	0.07	0.24	0.41	233.22	708.58	1783.85	0.25	0.48	0.64
Absolute Mean Std Atm Diff	**6.94**	**24.81**	**50.72**	**0.23**	**0.23**	**0.17**	**13.11**	**50.61**	**100.88**	**0.23**	**0.17**	**0.11**
Absolute Mean Std Atm Percent Diff	**0.06**	**0.07**	**0.06**	**0.58**	**0.38**	**0.24**	**0.05**	**0.07**	**0.06**	**0.37**	**0.22**	**0.13**
Absolute Mean FASCODE Diff	**17.28**	**102.54**	**210.67**	**0.21**	**0.16**	**0.06**	**26.39**	**132.98**	**193.52**	**0.21**	**0.12**	**0.04**
Absolute Mean FASCODE Percent Diff	**0.17**	**0.37**	**0.34**	**0.55**	**0.29**	**0.1**	**0.12**	**0.21**	**0.13**	**0.35**	**0.17**	**0.05**

Table 13 shows a much larger contrast because of the longer distance traveled

through the region of the atmosphere in which the aerosols have swelled. As seen in the

table, this almost reduces the signal-to-noise ratio in half for the 50 km 1.0642 μm case.

The larger effect at the 10 km altitude can be explained from the 10% gate starting at 1

km, near the bottom of the spike in the ExPERT atmosphere. The difference between the

two atmosphere transmissions are also much larger. The numbers are coming out to zero

for some columns because all numbers in the charts were truncated to two decimal places

for displaying purposes.

Table 13. North standard atmosphere with MODTRAN urban aerosols for the long range slant and vertical path

	50 km Slant Path						10 km Vertical Path					
Atm Type	1.0642 um SNR	1.56 um SNR	2.039 um SNR	1.0642 um T	1.56 um T	2.039 um T	1.0642 um SNR	1.56 um SNR	2.039 um SNR	1.0642 um T	1.56 um T	2.039 um T
MidLatNorthUrbanMod	0.02	1.49	9.42	0.02	0.14	0.24	25.36	88.69	220.81	0.48	0.68	0.75
FASCODE	0.12	2.41	7.65	0.07	0.18	0.21	35.95	96.48	201.63	0.57	0.71	0.72
PITTSBURGH/GREATER	0	0.37	5.42	0	0.06	0.15	21.52	77.82	198.54	0.35	0.57	0.69
CAMP SPRINGS/ANDREW	0	0.29	4.77	0	0.05	0.14	20.63	74.89	195.39	0.33	0.56	0.68
BOSTON/LOGAN INTL	0	0.07	2.44	0	0.03	0.09	13.66	50.57	155.85	0.25	0.48	0.63
LONDON/HEATHROW AIR	0	0.15	3.63	0	0.04	0.12	18.01	66.08	184.38	0.29	0.52	0.65
PARIS-ORLY	0	0.38	5.33	0	0.06	0.15	21.54	77.99	198.12	0.35	0.58	0.69
LUXEMBOURG/LUXEMBOU	0	0.26	4.75	0	0.05	0.14	20.39	74.09	195.17	0.32	0.55	0.68
ZURICH-KLOTEN	0	0.38	5.48	0	0.06	0.15	21.6	78.07	198.72	0.35	0.58	0.69
KYIV	0	0.17	3.84	0	0.04	0.12	18.5	67.69	186.87	0.3	0.53	0.66
SHANGHAI/HONGQIAO	0	0.02	0.6	0	0.01	0.06	2.7	9.68	23.94	0.2	0.43	0.57
PYONGYANG	0	0.01	0.5	0	0.01	0.06	1.95	7.12	17.62	0.19	0.42	0.57
Absolute Mean Std Atm Diff	0.01	1.28	5.74	0.02	0.1	0.12	9.31	30.29	65.35	0.18	0.15	0.1
Absolute Mean Std Atm Percent Diff	0.98	0.86	0.61	0.89	0.7	0.5	0.37	0.34	0.3	0.39	0.23	0.14
Absolute Mean FASCODE Diff	0.12	2.2	3.98	0.06	0.14	0.09	19.9	38.07	46.17	0.28	0.18	0.07
Absolute Mean FASCODE Percent Diff	1	0.91	0.52	0.96	0.77	0.44	0.55	0.39	0.23	0.49	0.26	0.09

Figure 20 displays the atmospheric profiles for both the standard and the ExPERT atmosphere with MODTRAN urban aerosols. The scale was kept constant for an easy comparison. The spike at about 1500 m, also known as the Fiorino spike, in the Expert atmosphere plots are due to the swelling of aerosols with the increase in relative humidity at the top of the atmosphere. While aerosol scattering decreases in the standard atmosphere at the two longer wavelengths, allowing aerosol absorption to become the major extinction constituent, aerosol scattering remains the number one extinction factor in the ExPERT profiles for all three wavelengths.
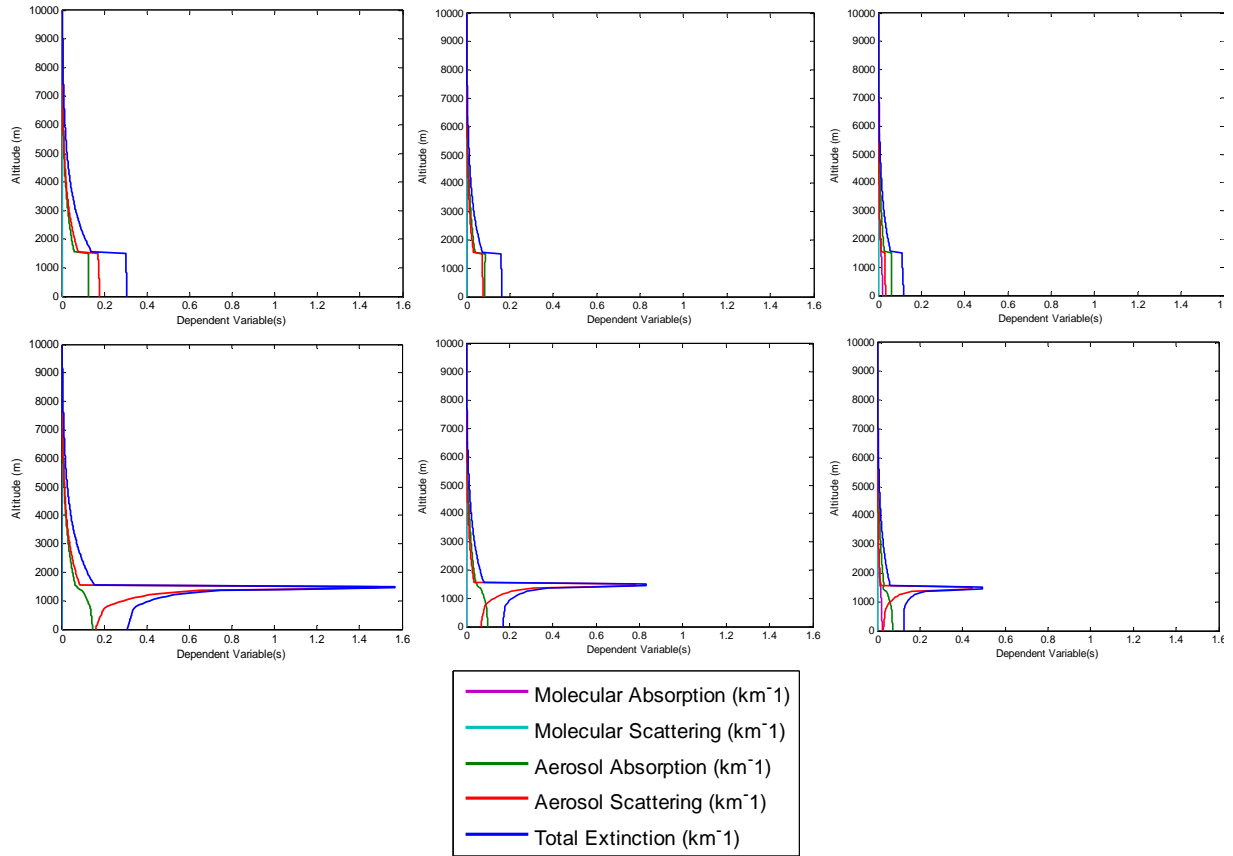
Figure 20. Atmosphere profiles for mid-latitude north with urban aerosols, top, and Paris, France ExPERT site, bottom. The columns from left to right are for the different wavelengths, 1.0642 μm, 1.56 μm, and 2.039 μm respectively.

4.2.1   Signal-to-Noise HELSEEM Image Results

The second part of this research was to analyze images produced with the

HELSEEM RPA tracking software. While looking at a Lambertian target to compare

atmospheric profiles is useful, it is not a very good approximation of reality. The

HELSEEM image of an RPA contains a complex bidirectional reflectance distribution

function (BRDF) that more closely approximates reality when imaging a military target.

The benefit of this is that the amount of detailed information that can be collected on a

target can be characterized. One of the major advantageous of LADAR is the spatial

resolution that is captured, and this type of analysis displays this detail.

76

Figure 21 displays images for the short range 3 km slant path engagement. Each row was produced with different atmosphere profiles while the columns left to right are the three wavelengths, 1.0642 μm, 1.56 μm, and 2.039 μm, respectively. A log scale was used to better show the detail at smaller signal-to-noise ratios while keeping all the images on the same scale. The ExPERT site used here is Shanghai, China in an effort to capture the extremes as it has the lowest signal-to-noise ratios of the ten sites analyzed earlier. The standard atmosphere used is the mid-latitude summer north. As before, the FASCODE images are produced by using the standard atmosphere noise and signals being attenuated with FASCODE transmissions, urban low visibility transmissions in this case.

There is an obvious boost in the signal-to-noise for the longer wavelengths for each atmosphere except for the ExPERT with GADS aerosols. Close inspection reveals there is some increase in the signal-to-noise, but it is very minor as compared to the standard atmosphere and FASCODE assessments. This can be explained by the composition of scattering versus absorption contribution to the total extinction. An interesting aspect that is captured in these images is the degree to which the ExPERT atmosphere has an effect with urban aerosols, the second row, as compared to the standard atmosphere with the same urban aerosol distribution. Here, the effect of allowing aerosols to swell with height at the top of the boundary layer reduces the signal-to-noise by almost two orders of magnitude. The large effect here can be explained from the fact that with the up-looking geometry and the target at 1530 m, the target is now "hiding" in the Fiorino Spike. Also, the solar scatter becomes more significant for up-looking geometries because aerosols preferentially scatter in the forward direction. The

77

ExPERT atmosphere scattering aerosols greatly raise the noise, keeping the signal-to-noise ratio low for all three wavelengths. The standard profile does not have this spike, allowing the signal-to-noise ratio to be much larger.
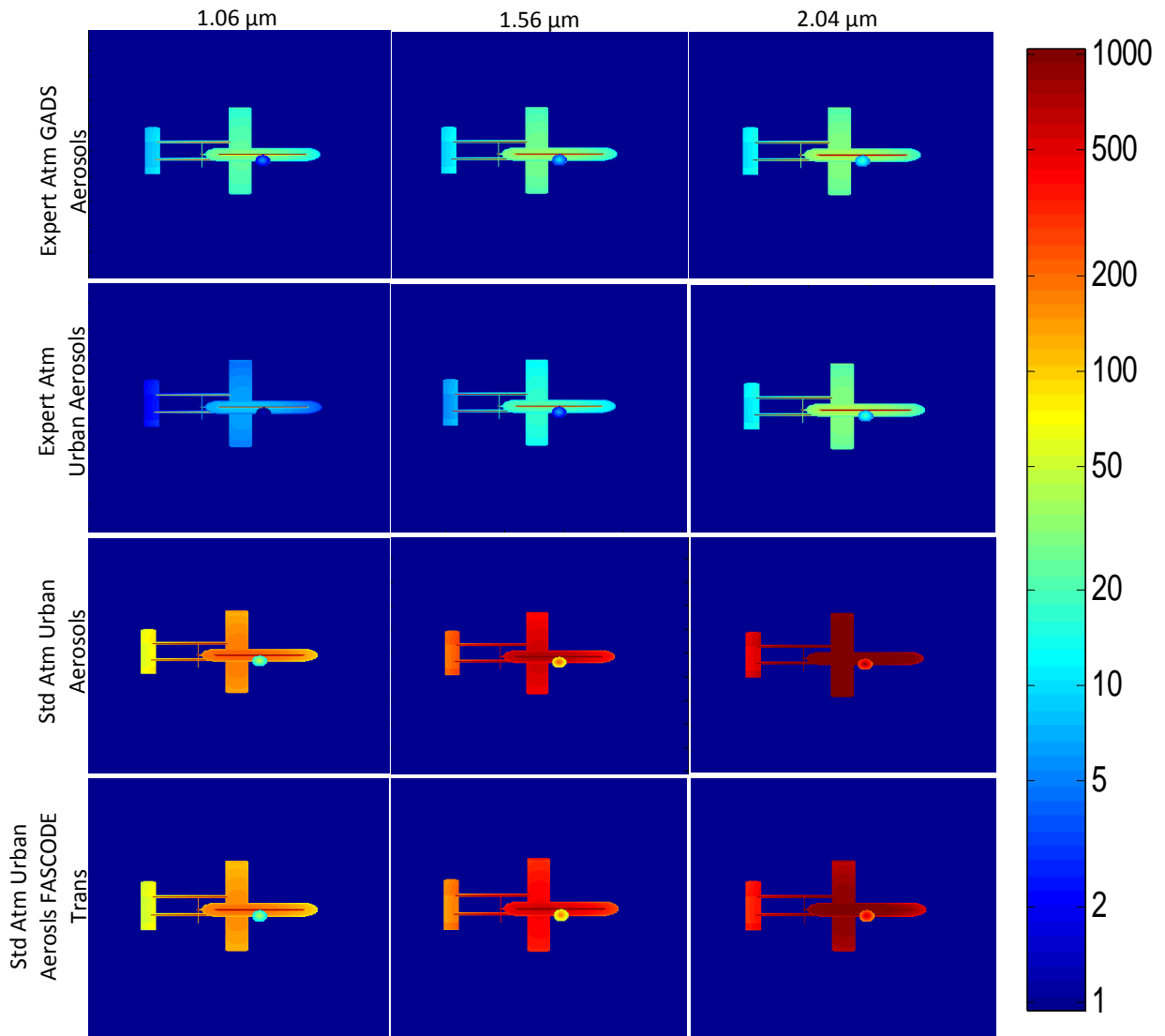

Figure 21. Short range 3 km slant path image signal-to-noise ratios. The platform is on the ground looking up at a 1530 m altitude target.

Table 14 displays the total path noise components in irradiance units of watts per meter squared for the 3 km slant path for the ExPERT Shanghai, China and the standard

atmosphere profile. The major difference between the two is the laser scatter being two orders of magnitude larger for the ExPERT atmosphere. The solar scatter is also much larger, being about one order of magnitude larger. The solar reflection is not included here as it was computed with HELSEEM and merely subtracted from the plane signature.

Table 14. Composition of noise components for the 3 km slant path geometry

ExPERT	Background	Laser Scatter	Solar Scatter	Black Body	Transmission
1.0642 μm	2.98E-05	1.937E-3	1.6E-4	3.69E-17	0.469779
1.56 μm	1.01E-05	1.565E-3	5.55E-05	1.05E-11	0.546315
2.039 μm	4.44E-06	8.33E-4	1.75E-05	3.72E-09	0.537467
Std Atm					
1.0642 μm	3.36E-05	9.15E-05	8.11E-05	3.17E-17	0.403737
1.56 μm	1.13E-05	6.91E-05	1.94E-05	1.19E-11	0.616893
2.039 μm	2.08E-06	2.95E-05	3.23E-06	4.92E-09	0.711559

Figure 22 is the signal-to-noise images for the 50 km up-looking engagement. The images are produced exactly the same way as Figure 21, except for the longer range geometry and the scale has been reduced to have a maximum value of 100. In this scenario, the increase in the signal-to-noise for the ExPERT atmosphere with GADS aerosols with the increase in wavelength is very apparent. At the 1.0642 μm wavelength, very little shows up above the noise besides the normal facing stripe on the fuselage and the front tail strut of the RPA for every atmosphere except for the ExPERT with urban aerosols, in which case the plane is not visible at all. There is a drastic difference displayed in this scenario between the standard atmosphere with urban aerosols and the ExPERT atmosphere with urban aerosols. In fact, for both the 1.0642 μm and the 1.56 μm wavelength ExPERT atmosphere with urban aerosols image, no information can be gained about the plane. There is also a noticeable difference between the standard

atmosphere and the FACODE images at the 1.56 µm wavelength. The FASCODE

transmission is clearly less than that of the standard profile, causing lower signal-to-noise

ratios. The large difference between the ExPERT and standard profile images can once

again be explained from the aerosol spike at the top of the boundary layer. Although the

gate is far above the spike, solar scattering noise, which is the dominate noise source for

the long range scenario, comes from scattering over the entire path. The difference

between the up-looking images in Figure 22, and the smaller effect previously seen in the

long range down looking tables can be explained by the fact that the aerosol spike is now

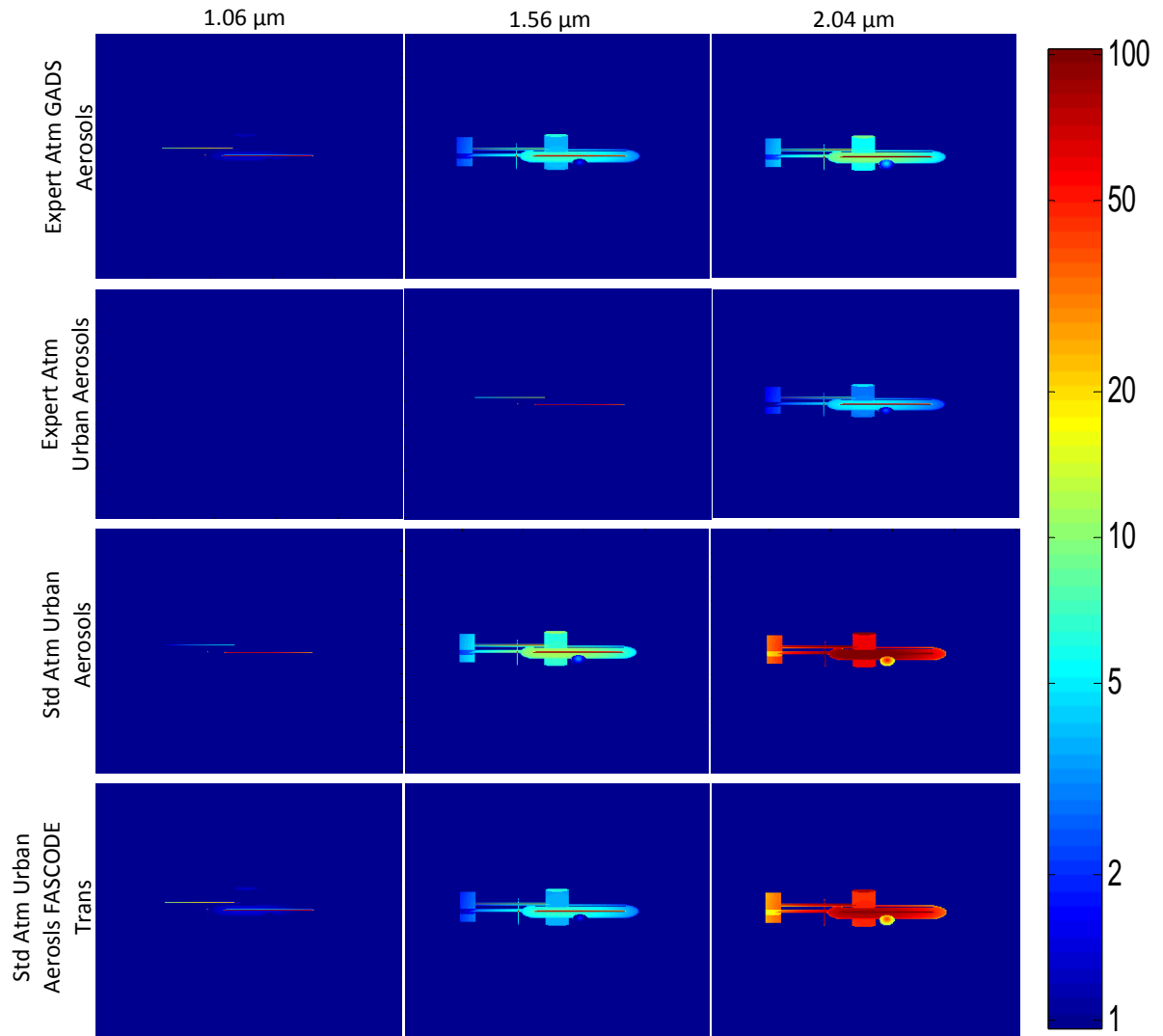much closer to the receiver with much less distance to disperse.

Figure 22. Long range 50 km slant path image signal-to-noise ratios. The platform is on the ground looking up at a 10 km altitude target.

Table 15 lays out all the noise components for the above images. While the transmissions increase for each increasing wavelength for the standard atmosphere, the transmission actually drops from the 1.56 μm to the 2.039 μm wavelength for the ExPERT atmosphere. Although the transmission drops between these wavelengths, the image is still brighter as seen in Figure 22. This clearly shows that just looking at the transmissions alone cannot determine LADAR performance.

Table 15. Composition of noise components for the 50 km slant path geometry

ExPERT	Background	Laser Scatter	Solar Scatter	Black Body	Transmission
1.0642 µm	8.34E-08	2.00E-08	7.29E-06	4.44E-19	0.094184
1.56 µm	5.43E-08	1.73E-08	2.62E-06	1.85E-13	0.160024
2.039 µm	1.39E-07	6.94E-09	7.66E-07	5.94E-11	0.143053
Std Atm					
1.0642 µm	1.71E-08	1.10E-09	3.57E-06	1.12E-19	0.023753
1.56 µm	1.10E-08	8.27E-09	1.19E-06	1.60E-13	0.138791
2.039 µm	3.19E-09	8.32E-09	2.22E-07	9.85E-11	0.237333

Figure 23 explains why just looking at the transmissions alone is unable to predict the signal-to-noise ratio. By looking at the profiles, why the signal-to-noise ratio goes off the charts for the standard atmosphere while increasing at a much smaller rate for the ExPERT atmosphere can be seen. Notice at the two longer wavelengths that aerosol absorption becomes the major extinction constituent for the standard atmosphere profiles while scattering remains extremely high in the ExPERT profile with very little contribution from absorption. This is important because the noise seen by the Geiger mode LADAR system is due to scattering. Therefore, two profiles could have exactly the same transmission while the signal-to-noise ratios could differ greatly. The scales are changed from plot to plot so the contributions to extinction from the different parameters could be identified.
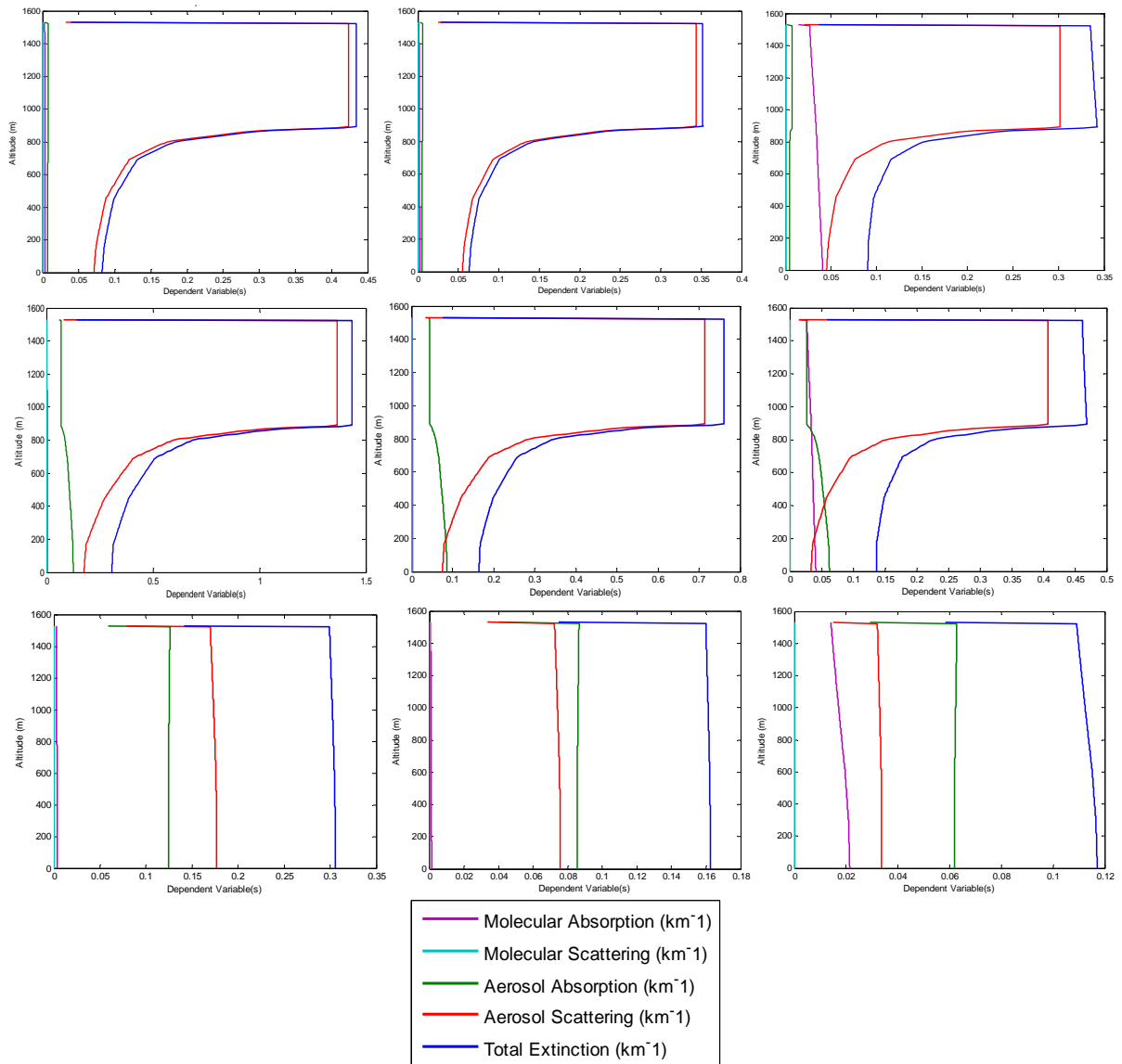
Figure 23. Atmosphere profiles for Shanghai ExPERT with GADS aerosols, Shanghai ExPERT with urban aerosols, and mid-latitude north with urban aerosols from top to bottom. The columns left to right are for the three wavelengths, 1.0642 μm, 1.56 μm, and 2.039 μm respectively. The plots have the extinction coefficient values (km⁻¹) along the x axis and altitude (m) along the y axis.

While analyzing atmospheric effects on LADAR signatures, atmospheric turbulence cannot be ignored. While turbulence will not affect the actual signal-to-noise ratio, it will affect what information can be obtained from the target. Figure 24 is created using the climatological wind and turbulence profiles at the 50th percentile in LEEDR.

Turbulence has very little effect on the 3 km slant range, but has a drastic effect on the 50 km slant range. In the 3 km slant path geometry images, fine detail about the RPA can be identified, including the radar dome on its belly as well as the dimensions of various components of the aircraft. At the 50 km range, all detail of the plane as been blurred, to the point it is hard to even tell if it is an airplane.
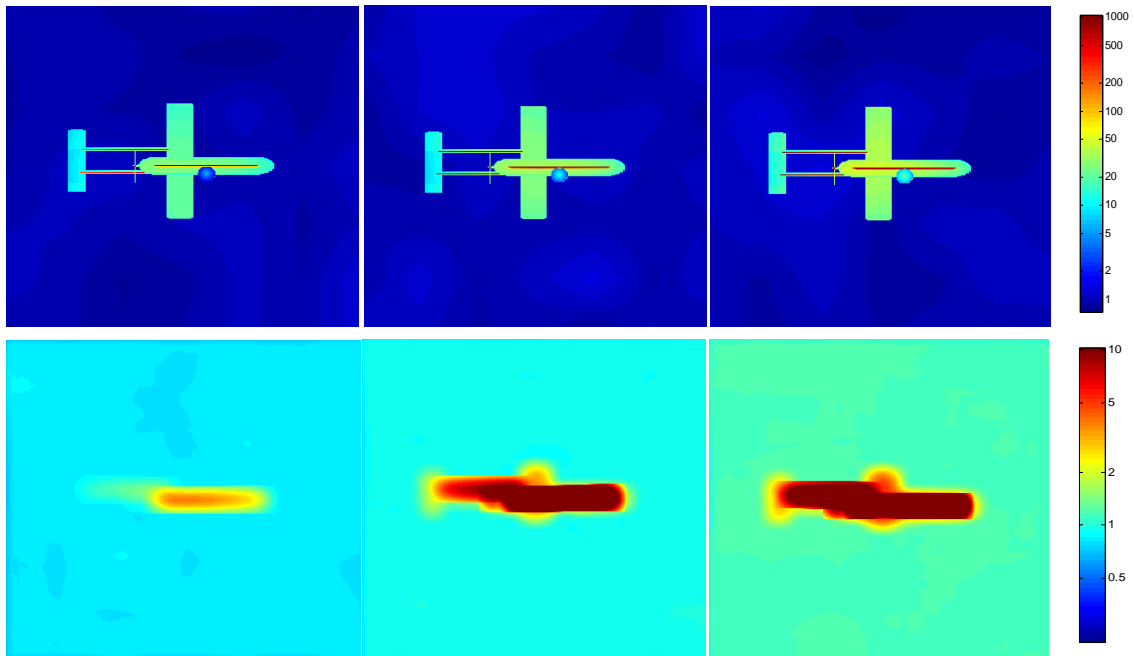

Figure 24. ExPERT with GADS images with atmospheric turbulence effects. Top row is the 3 km slant path engagement while the bottom row is the 50 km slant path engagement. From left to right the columns are for the 1.0642 μm, 1.56 μm, and the 2.039 μm wavelength respectively.

4.3   Summary

The global signal-to-noise ratios computed using LEEDR atmospheres revealed how the signal-to-noise varied with wavelength, engagement geometry and climate. While the standard profile characterizations many times provided satisfactory results in describing the average LADAR performance in different atmospheric conditions, there is strong variability between global locations despite having similar environments. This

variability is better captured with the ExPERT atmospheres and GADS aerosols. The signal-to-noise ratio and transmission are shown to not always correlate. Images of an RPA displaying signal-to-noise in conjunction with atmosphere profiles reveal that the correlation between signal-to-noise and transmission values is greatly dependent upon the composition of the scattering and absorption of the extinction profiles. These images also show that ignoring the aerosol spike at the top of the boundary layer leads to signal-to-noise ratio values that can be several orders of magnitude too large being wavelength, geometry, and gate location dependent.

V   Conclusions and Recommendations

5.1   Chapter Overview

Current developers of LADAR systems do not have tools to accurately model many propagation features of the atmosphere. The objective of this research is to quantify the effect of using the more realistic LEEDR atmospheres versus a standard atmosphere profile when simulating LADAR signal-to-noise ratios. This study shows that accounting for location climatology and aerosol expansion at the top of the boundary layer can cause orders of magnitude differences in signal-to-noise evaluations.

5.2   Conclusions of Research

Upon the onset of this research, the goal was to show the advantages of using a probabilistic climatological approach to modeling atmospheric effects on LADAR performance. From plotting global maps of signal-to-noise ratios computed using ExPERT atmospheres with GADS aerosols, it is clear that the different climates give different values. In fact, desert and maritime regions have signal-to-noise ratio values orders of magnitude less than rural areas. This suggests that a standard profile with a standard aerosol model may be able to capture these different regions of the earth. However, after careful analysis by choosing various locations that should be adequately described by a certain standard profile, significant differences are seen.

The differences are rooted in the fact that just because a specified location has a certain type of climate, its atmosphere is still significantly different than a similar climate at another location on the globe. For instance Wadi Halfa, Sudan and Nellis AFB, Nevada from Table 4-5 can both be described as desert locations. However, Wadi Halfa

86

has a signal-to-noise ratio of 30.15 while Nellis has a signal-to-noise ratio of 72.81. The standard atmosphere solution is 31.18. Using a standard atmosphere with a standard profile gives a ballpark answer, but does not give the precision needed when evaluating the performance of combat systems. For all the scenarios studied, the average absolute mean percent difference in signal-to-noise ratios is 1.03, meaning the ExPERT site on average gives a value with a difference of about the value of that of the standard profile. Over all, a value of 0.34 for the equivalent transmission comparison is found. The equivalent median signal-to-noise ratio and transmission values are 0.51 and 0.15 respectively. Surprisingly just using the FASCODE transmissions for the signal generation reduces this value to 0.847. The biggest difference comes from the 50 km slant path urban comparison at 1.0642 μm for which the ExPERT sites give signal-to-noise ratios 72 times greater than that of the standard profile which is excluded from the above statistics being an outlier.

Another significant result is the analysis of correlations between signal-to-noise ratios and transmission values. There is clearly some correlation, but what really matters is the composition of the total extinction profile between absorption and scattering. Because scattered energy constitutes the largest noise component in the Geiger mode LADAR system, more scattering means more noise. Therefore, two profiles can give the same transmission, but significantly different signal-to-noise ratios. This is clearly seen in the HELSEEM 3 km slant path for the 1.0642 μm wavelength as the transmission is 0.4 or 40% for the standard profile and 0.47 or 47% for the ExPERT profile, yet the signal-to-noise in much of standard profile image is more than four times greater than that of the ExPERT profile.

Another conclusion can be drawn from comparing the images produced with urban aerosols, one with a Shanghai ExPERT atmosphere, and the others with the standard profile. These images show that ignoring the swelling of aerosols with altitude as the standard profile does leads to orders of magnitude differences in the signal-to-noise ratio. Without factoring in the aerosol spike at the top of the boundary layer, it is impossible to accurately model LADAR propagation that travels any significant distance in this region.

5.3   Significance of Research

One important result of this research is that a method is developed by which Geiger mode LADAR system environmental effects can be analyzed. Also, a technique to compare different atmosphere profiles is shown. This sets the foundation from which future research can be developed.

The variance of location climatology is significant enough that a single atmospheric model for similar environments cannot effectively capture the effects on LADAR systems. This research shows that if a standard profile is used to model environmental effects on a Geiger mode LADAR system, the solution could be orders of magnitude different from that of a probabilistic approach. Also, this study shows the importance of allowing aerosol effects to increase at the top of the boundary layer where they swell with relative humidity. Once again, the difference between allowing aerosols to swell and failing to let them swell was a couple orders of magnitude in the signal-to-noise ratio. This investigation also shows that not only is the total transmission important in determining the signal-to-noise, but also the composition of total extinction between absorption and scattering.

The engagement geometries studied show some interesting employment techniques that could both be used to exploit and defeat the environmental conditions. As expected, longer engagement geometries cause lower signal-to-noise ratios, but more significant was the atmospheric turbulence effects. To capture useful data at high altitudes, it is expected that near vertical geometries are required or the employment of adaptive optics techniques. An even more fascinating result is that ground LADAR systems will have a much lower signal-to-noise ratio for targets flying at the top of the boundary layer where aerosol scattering is maximized. The aerosol spike could effectively be used to hide small RPAs from ground based LADARs.

LADAR is an emerging technology, and as systems are built, it is important to understand their performance in certain environments. If atmospheric effects are deemed insignificant on the system because of a study done using a standard atmosphere, actual experimental data may yield a completely different analysis. Using a climatological approach in modeling these systems will better capture the effects various atmosphere types around the world will have on the system. With this knowledge, developers will be able to better tailor the system to the type of environment in which it is expected to operate.

5.4   Recommendations for Future Research

The results show that there is significant variance between a climatological and a standard profile approach. However, how more accurate the climatological approach is, or if it is even more accurate, is not studied. An analysis against real LADAR system signal-to-noise high fidelity data at various locations would be an appropriate way to determine the validity of the probabilistic atmosphere approach. Another way to validate

the probabilistic approach would be to leave the LADAR system out of the equation, and do an in-depth analysis and validation of the ExPERT atmosphere profiles with GADS aerosols.

This research only focused on the environmental effects and therefore did not consider different real-world LADAR detectors. By analyzing an actual detector's capability, the signal-to-noise ratios could be tailored to determine if signals would be detected for that system. This type of analysis could be done at a specified location and then compared to experimental data. A major simplification is taken in the probability of detection versus false alarm analysis as only a single pulse scenario is examined. To better characterize the detectability of a particular system, a statistical analysis would need to be accomplished. Some LADAR systems operate as a continuous wave instead of distinct pulses. Some of the analysis in this research would still apply, but a different approach would need to be taken as they operate far differently than the pulsed system.

Every situation modeled in this study is for clear air with 50th percentile humidity. If a global capability of a particular system needed to be analyzed, cloud and rain effects would need to be included. To accomplish this type of study, an analysis of the effects different hydrometers have on the LADAR and then the probability of these hydrometers at locations worldwide could be analyzed. Global plots could be made to show what percent of the time at various locations worldwide conditions allow for a specified signal-to-noise threshold to be met. This would be invaluable to operators of these systems as they would be able to assess at what locations they should expect them to function at acceptable levels.

More comparisons against different wavelengths, especially in the visible spectrum, could show the advantages of not only certain wavelengths, but also LADAR systems versus other systems that operate at certain wavelengths. It is expected that systems that are optically based in the visible spectrum would show much degradation as atmospheric haze would cause more attenuation.

5.5   Summary

The goal of this research was to quantify the advantages and differences between modeling LADAR environmental effects with standard atmosphere and standard aerosol profiles versus the probabilistic approach available using LEEDR ExPERT sites and GADS aerosols. The mean absolute deviation between the two methods was quantified and deemed significant. Integrating LEEDR into LADAR system performance models would better capture the atmosphere physics and climatological effects on these systems. Also, further validation needs to be performed on the ExPERT profiles in order to develop more confidence in their accuracy.

Appendix A

```matlab
function LADAR_SNR()
%% Setup initial Vars
%% Finds backscatter from a downlooking LADAR
% Uses the Aperture diameter as the initial size of the beam and then
the user defined spot size as the diameter of the beam at the target

clear all
close all
warning('off')

global Inputs outputs transoutputs globalvars
%add path settings for HELEEOS - update to your directory structure
% addpath(genpath('I:\My Documents\CDE'))

%Inputs
gateFraction=.1; %fraction of the beam length in front of target that
is in the gate
pulseLength=.5e-9;%5e-9; %time of rectangular pulse (s)
addedLength=0; %added distance to front of detector for backscatter
calc
targetReflectance=.1; %reflectance of the target
targetDisp=pi; %solid angle of dispersion from the target (rads)(pi for
Lambertian)
bandWidth=4e-9; %bandwidth of LADAR receiver (m)
backGroundTemp=300; %temperature of target area for BB calc (K)
detLength=1e-4; %length of square detector side for FOV calc (m)
FOV=detLength/recFocalLength
recFocalLength=.5; %focal length of receiving optics for FOV calc (m)
solarsegnum=100; %number of FOV partitions for solar backscatter
calculation
zenithAngle=1e-4; %sun zenith angle 1e-4 to 90 (deg)(cannot be zero
because of trig functions)
scatterAngle=120.6638; %Scattering angle of Sun light from original
direction in FOV to receiver (deg)
targetNormalAngle=0; %Angle of target surface normal to incident beam
(deg)
solarNormalAngle=59.3362; %Angle of target surface normal to incident
solar radiation (deg)
globalvars.FileName='LADAR'; %'LADAR';
globalvars.SpotSize='diffraction'; %2.9327;%;%; %diameter (m),
'diffraction' for Heleeos calculated
%%%%%%%%%%%%%%%%%%%%%%%%%%%%%%%%%%%%%%%%%%%%%%%%%%%%%%%%%%%%%%%%%%%%%%%%

%load HELEEOS data
load('C:\Users\Ben\Documents\CDE\GUIs\HELEEOS\mainHeleeos3Library.mat')
%Update this to your directory structure
inputsStruct =
savedStructures{find(strcmpi(savedStructures(:,1),globalvars.FileName))
,2}; %Load the saved setting profile
clear savedStructures

load ExPERTData.mat locationCellArray
```

92

```matlab
%Change saved inputs for Heleeos file
inputsStruct.page3.tab2.Power=20e6;%1000; %Change the power
inputsStruct.page3.tab2.wavelength=25; %25 option is the user defined
wave length
% inputsStruct.page3.tab2.userWavelength=1.0642e-6;
lambda=[1.0642e-6 1.56e-6 2.039e-6];
% inputsStruct.page3.tab1.initialDist=196078.603; %change beam length
% inputsStruct.page4.tab1.initialAlt=100000; %target Altitude
inputsStruct.page3.tab1.initialDist=3000; %change beam length
inputsStruct.page4.tab1.initialAlt=0; %target Altitude
inputsStruct.page3.tab1.initialAlt=1530; %Platform Altitude

PlatAlt=[1530,1530,10000,10000];
initialDist=[3000,1531,50000,10001];
% Set up loop for all geometries, wavelengths, and ExPERT sites
for k=1:4
inputsStruct.page3.tab1.initialAlt=PlatAlt(k); %Platform Altitude
inputsStruct.page3.tab1.initialDist=initialDist(k); %change beam length
if k==1;
scatterAngle=120.6638;
solarNormalAngle=59.3362;
end
if k==2;
scatterAngle=180;
solarNormalAngle=0;
end
if k==3;
scatterAngle=101.537;
solarNormalAngle=78.463;
end
if k==4;
scatterAngle=180;
solarNormalAngle=0;
end
% Set global variables
globalvars.platAlt=inputsStruct.page3.tab1.initialAlt;
globalvars.targAlt=inputsStruct.page4.tab1.initialAlt;
globalvars.beamLength=inputsStruct.page3.tab1.initialDist;
globalvars.zenithAngle=zenithAngle;

NumberOfBins=round(globalvars.beamLength*gateFraction/(2.99793e8*pulseL
ength));
SNR_Out = zeros(length(locationCellArray),9);
backScatter_Out = zeros(length(locationCellArray),NumberOfBins);
for j=1:3
inputsStruct.page3.tab2.userWavelength=lambda(j);
for i = 1:length(locationCellArray)

    m = (locationCellArray{i,3}); %lat
    n = (locationCellArray{i,4}); %lon

    inputsStruct.page2.tab1.currentLat = m;
    inputsStruct.page2.tab1.currentLon = n;
    globalvars.lat=m;
```

93

```matlab
    globalvars.lon=n;

    % Input to Heleeos and Run Heleeos
     Inputs = GuiStruct2DataStruct(inputsStruct);
     outputs = heleeosCalcTotalScenario(Inputs,false); %make the
calculation
    % Find slant range to calculate the spot size from additional
outputs
    % function
    R=globalvars.beamLength;

outputs.avg=heleeosCalcAdditionalOutputs('Spot',outputs.avg,outputs.Inp
uts,'1/e','T',R);
    globalvars.transmission=outputs.avg.totalTrans;

     SignalIrr=signal(targetReflectance,targetDisp, detLength,
recFocalLength,targetNormalAngle)
    [BinBScaIrr, TotalBScaIrrFromSeg] =
backscatter(gateFraction,pulseLength,addedLength);

    [bbIrr, solarReflIrr]=background(bandWidth,backGroundTemp,
targetReflectance, targetDisp, detLength,
recFocalLength,solarNormalAngle)
    SolarScaIrr =
solarBackscatter(solarsegnum,addedLength,detLength,recFocalLength,bandW
idth,zenithAngle,scatterAngle)

    TotalNoise=BinBScaIrr+bbIrr+solarReflIrr+SolarScaIrr;

SNR_Out(i,:)=[m,n,SignalIrr,TotalNoise,BinBScaIrr,solarReflIrr,SolarSca
Irr,bbIrr,Transmission];
    backScatter_Out(i,:)=TotalBScaIrrFromSeg;
    i

if k==1
    totalDistance='3km';
end
if k==2
    totalDistance='1530m';
end
if k==3
    totalDistance='50km';
end
if k==4
    totalDistance='10km';
end

end
    if j==1

save(['Data__1_0642_',totalDistance,'.mat'],'SNR_Out','backScatter_Out'
)  %save variables - change the .mat file name to what you want
    end
    if j==2
```

```matlab
save(['Data__1_56_',totalDistance,'.mat'],'SNR_Out','backScatter_Out')
%save variables - change the .mat file name to what you want
    end
    if j==3

save(['Data__2_039_',totalDistance,'.mat'],'SNR_Out','backScatter_Out')
%save variables - change the .mat file name to what you want
    end

end
end




function [signalIrr] = signal(rho_t,theta_r,delta,fl,normalAngle)
%SignalIrr Calculates the Irradiance at the reciever
% Signal(rho_t,theta_r,delta,fl,normalAngle) where rho_t is the
reflectivity of the target, theta_r is the dispersion solid angle (pi
for Lambertian targets) delta is the length of one side of the square
reciever detector, fl is the focal length of the reciever optics, and
the normalAngle is the incident angle to the target relative to the
normal.  The code uses a simple top hat beam with a constant divergence
angle The exit aperture is the size of the beam at exit while the user
%   defined spot size is the size of the beam at the target
global Inputs outputs globalvars
if strcmp(globalvars.SpotSize,'diffraction')==1;
    spotSize=outputs.avg.irrDiffBQTurbSpotSizeT;
else
    spotSize=globalvars.SpotSize;
end

exitApDiam=Inputs.transmittingOptics.platform.exitApDiam;

% Distance to target
R=globalvars.beamLength;
Ta=outputs.avg.totalTrans;

% Beam divergence angle
theta_t=(spotSize-exitApDiam)/R;
Pt=Inputs.Laser.power; % Transmitting Power
% dA=pi*(theta_t*R+exitApDiam)^2/4;% for illuminating beam limited
dA1=(delta/fl*R)^2; %target area seen by the reciever (receiver FOV
limited)
dA2=pi*(theta_t*R+exitApDiam)^2/4; % for illuminating beam limited
if dA1 < dA2 %determine which effective target surface area is limiting
    dA=dA1;
%     disp('Effective target surface area is receiver FOV limited')
else
    dA=dA2;
%     disp('Effective target surface area is illuminating beam
limited')
end
```

```matlab
% Equation from Direct-Detection LADAR Systems, Richmond and Cain
signalIrr=4*Ta^2*Pt*cos(normalAngle*pi/180)*rho_t*dA/(pi*(theta_t*R+exi
tApDiam)^2*R^2*theta_r);
end




 function [BinBScaIrr, TotalBScaIrrFromSeg] =
backscatter(gate,pulseLength,segOne)
%% Finds backscatter from a downlooking LADAR
% only calculates backscatter within the gate
% backscatterEvenSpaced(segnum,gate,segOne) where segnum is the number
of evenly spaced partitions of the beam, gate is the fraction of the
beam length where the LADAR gate is open, and segOne is an added length
to prevent 1/R^2 from 'blowing up' and must be less than a couple of
meters Uses the Aperture diameter as the initial size of the beam and
then the User defined spot size as the diameter of the beam at the
target

global Inputs outputs globalvars
%add path settings for HELEEOS - update to your directory structure
% addpath(genpath('I:\My Documents\CDE'))
clear Extd

c=2.99793e8; %speed of light
platAlt=globalvars.platAlt;
targAlt=globalvars.targAlt;
beamLength=globalvars.beamLength;
gateLength=beamLength*gate;
binLength=pulseLength*c;
segnum=round(gateLength/binLength);
toGateSegnum=1000;

% atmospheric coefficients needed
%      1000x91 matrix with 1000 altitudes and 91 angles (0 to 180 in 2
deg steps)
if strcmp(globalvars.SpotSize,'diffraction')==1;
    spotSize=outputs.avg.irrDiffBQTurbSpotSizeT;
else
    spotSize=globalvars.SpotSize;
end

exitApDiam=Inputs.transmittingOptics.platform.exitApDiam;
aeroPhase=squeeze(outputs.Atmosphere.PhaseFunctions.aerosol);
aeroPhase=aeroPhase(:,end); %91 is the 180 degree (backscatter)
aeroSca=outputs.Atmosphere.aeroSca; %1000 altitudes
molPhase=outputs.Atmosphere.PhaseFunctions.molec;
molSca=outputs.Atmosphere.molecSca;

if platAlt > targAlt
    look='down';
else
```

```matlab
    look='up';
end


totalHt=gate*abs(platAlt-targAlt); %height of gate
segHt=totalHt/segnum; %height of each segment
% Determine the altitudes of the segments
if platAlt > targAlt
    beamAlts=targAlt+segHt/2:segHt:totalHt-segHt/2;
else
    beamAlts=targAlt-totalHt+segHt/2:segHt:targAlt-segHt/2;
end


%       Determine the Phase and Scattering function for the segments
aeroPhaseFcn=interp1(outputs.Atmosphere.altVector,aeroPhase,beamAlts);
aeroScaFcn=interp1(outputs.Atmosphere.altVector,aeroSca,beamAlts)./1000
; %change to per m
molPhaseFcn=molPhase(91); %backscatter 180 degree
molScaFcn=interp1(outputs.Atmosphere.altVector,molSca,beamAlts)./1000;
%change to per m


%       Determine Extinction (m^-1) at the segment centers
Extinction=interp1(outputs.Atmosphere.altVector,outputs.Atmosphere.tota
lExt,beamAlts)./1000; %change to per m
segLength=gate*beamLength/segnum; %Length of segments


% distances from platform to each of the beam segment centers starting
% from beam segments at lowest altitude
if strcmp(look,'down')==1;
    pathLength=beamLength-segLength/2:-segLength:beamLength-
gateLength+segLength/2;
else
    pathLength=beamLength-gateLength+segLength/2:segLength:beamLength-
segLength/2;
end


pathLength=pathLength+segOne;  % add small distance to prevent 1/R^2
'blow up'
Extseg=Extinction.*segLength; % optical depth for each segment in
increasing altitude


% Calculate optical depth for each segment center to gate front
if strcmp(look,'down')==1;
    Extd(segnum)=Extseg(segnum); %first extinction is just the first
optical depth
    for k=segnum-1:-1:1
        Extd(k)=Extd(k+1)+Extseg(k);
    end
else
    Extd(1)=Extseg(1); %first extinction is just the first optical
depth
    for k=2:1:segnum
        Extd(k)=Extd(k-1)+Extseg(k);
    end
end
```

```matlab
pathTrans=exp(-Extd); %Transmission to each segment center to front of
gate

% Transmission to gate front
if gate==1
    toGateTrans=0;
else
    toGateSegHt=(abs(platAlt-targAlt)-totalHt)/toGateSegnum; %height of
each segment
    if platAlt > targAlt
        toGateAlts=totalHt+toGateSegHt/2:toGateSegHt:platAlt-
toGateSegHt/2;
    else
        toGateAlts=toGateSegHt/2:toGateSegHt:targAlt-totalHt-segHt/2;
    end

toGateExtinction=interp1(outputs.Atmosphere.altVector,outputs.Atmospher
e.totalExt,toGateAlts)./1000; %change to per m
    toGateSegLength=(1-gate)*beamLength/toGateSegnum; %Length of
segments
    toGateExtseg=toGateExtinction.*toGateSegLength; % optical depth for
each segment in increasing altitude
    % Calculate optical depth for gate front to platform
    toGateExtd=sum(toGateExtseg);
    toGateTrans=exp(-toGateExtd); %Transmission to gate front
end
pathTrans=pathTrans.*toGateTrans;
incPower=pathTrans.*outputs.Inputs.Laser.power; %incident power at each
segment center

% Create diameters for beam
size1=exitApDiam;
size2=spotSize;
theta_t=(size2-size1)/beamLength; %beam divergence angle
size1=theta_t*(beamLength*(1-gate))+size1; %spot size at gate front
if strcmp(look,'down')==1;
    diameter=linspace(size2,size1,segnum+1); %segnum+1 equally spaced
diameters
else
    diameter=linspace(size1,size2,segnum+1); %segnum+1 equally spaced
diameters
end

diameter=(diameter(1:end-1)+diameter(2:end))./2; %diameters at segment
centers
area=pi.*(diameter./2).^2; % (m^2)
incIrr=incPower./area; % (W*m^-2)
% Calculate the scattering volume elements
dv=segLength.*area;
% Scattered Irradiance (w*m^-2)

% Equation from Fiorino "Field Measurements and Comparisons to
Simulations
% of High Energy Laser Propagation and Off-Axis Scatter" paper
```

```matlab
aeroBScaIrrFromSeg=(aeroPhaseFcn.*aeroScaFcn.*incIrr.*pathTrans.*dv)./(
4.*pi.*pathLength.^2);
molBScaIrrFromSeg=(molPhaseFcn.*molScaFcn.*incIrr.*pathTrans.*dv)./(4.*
pi.*pathLength.^2);
TotalBScaIrrFromSeg=aeroBScaIrrFromSeg+molBScaIrrFromSeg;
BinBScaIrr=max(TotalBScaIrrFromSeg);




function [bbIrr, solarReflIrr] = background(bandWidth, T, rho_t,
theta_r, delta, fl,solarNormalAngle)
global Inputs outputs transoutputs globalvars

% Determine Blackbody and Solar Reflection background, solar reflection
% assumes the suns position is at zenith for max solar irradiance and
is still able to have perpendicular reflection although this is not
true
% unless the platform is looking directly downward

%constants
h=6.62607e-34; % Planck's constant (J*s)
c=2.9979e8; % Speed of Light (m/s)
kb=1.38065e-23; % Boltzmann's constant

Specpts=10; % # of even spaced points in the bandwidth for Solar
Spectrum
R=globalvars.beamLength;
FOV=delta/fl*R; %(m) linear FOV at target (side of square)
Ta=globalvars.transmission;

%Runs Heleeos to find total normal atmospheric transmittance from
infinity
load('C:\Users\Ben\Documents\CDE\GUIs\HELEEOS\mainHeleeos3Library.mat')
;
transInputsStruct =
savedStructures{find(strcmpi(savedStructures(:,1),globalvars.FileName))
,2};
clear savedStructures

%platform altitude (must be going same direction as previous Heleeos
run)
if globalvars.platAlt>globalvars.targAlt
    transInputsStruct.page3.tab1.initialAlt=100000; %plat alt
    transInputsStruct.page3.tab1.initialDist=100001; %path length
    transInputsStruct.page4.tab1.initialAlt=0; %target Alt
else
    transInputsStruct.page3.tab1.initialAlt=0;
    transInputsStruct.page3.tab1.initialDist=100001; %path length
    transInputsStruct.page4.tab1.initialAlt=100000; %target Alt
end
transInputsStruct.page2.tab1.currentLat = globalvars.lat;
transInputsStruct.page2.tab1.currentLon = globalvars.lon;
```

```
% transInputsStruct.page2.tab1.stdMetTypeValue=globalvars.stdAtm;
% transInputsStruct.page2.tab1.stdAeroTypeValue=globalvars.stdAero;

% transInputsStruct.page5.tab1.enableObserverValue=0;
transInputs = GuiStruct2DataStruct(transInputsStruct);
transoutputs = heleeosCalcTotalScenario(transInputs,false);
lambda=Inputs.Laser.wavelength;


IncSolarIrr=
SolarIrr(globalvars.targAlt,globalvars.zenithAngle,lambda,bandWidth);
% black body Wm^-2*Sr^-1*m^-1
% (power per area, solid angle and wavelength)
bbradiance=(2.*h.*c.^2)./(lambda.^5.*(exp(h.*c./(kb.*lambda.*T))-1));
solidAngle=FOV^2/R^2;
bbIrr=bbradiance*solidAngle*bandWidth*Ta;

% Solar Reflected Irradiance
dA=FOV^2; %FOV area
solarReflIrr=IncSolarIrr*cos(solarNormalAngle*pi/180)*rho_t*dA*Ta/(R^2*
theta_r);




function [TotalsolarBScaIrr] =
solarBackscatter(segnum,segOne,delta,fl,bandWidth,zenithAngle,scatterAn
gle)
%% Finds solar backscatter for a downlooking LADAR
% solarBackscatter(segnum,segOne, delta, fl) where segnum is the number
of
% evenly spaced partitions of the field of view, segOne is an added
length to
% prevent 1/R^2 from 'blowing up' and must be less than a couple of
meters
% delta is the side of the detector, and fl is the reciever focal
length
% For molecular scattering Rayleigh scattering is used, assuming that
the
% incident radiation is unpolarized
global Inputs outputs cosTheta globalvars
clear Extd incIrr TotalsolarBScaIrr aeroPhase
% % Inputs
% segnum=100; %number of partitions of the beam
% segOne=1; %length (m) from detector to prevent 1/R^2 from 'blowing
up' cannot be zero
% delta=1e-4; %side of the detector (m)
% fl=.1; %focal length of recieving optics
% zenithAngle=1e-4; %sun zenith angle degrees
% bandWidth=4e-9; %band width of reciever (m)
% scatterAngle=120; %angle sun scatters from original direction to
return to the platform

lambda=outputs.Inputs.Laser.wavelength; %wavelength (m)
```

```matlab
 % atmospheric coefficients needed
%       1000x91 matrix with 1000 altitudes and 91 angles (0 to 180 in 2
deg steps)
aeroPhaseAll=squeeze(outputs.Atmosphere.PhaseFunctions.aerosol)';
aeroSca=outputs.Atmosphere.aeroSca; %1000 altitudes
molPhase=outputs.Atmosphere.PhaseFunctions.molec;
molSca=outputs.Atmosphere.molecSca;

theta=linspace(0,pi,length(molPhase));
cosTheta=cos(theta);
% for j=1:91;
% scatterAngle=90-zenithAngle+0;
scatterCos=cos(scatterAngle*pi/180);
molPhaseFcn=interp1(cosTheta,molPhase,scatterCos);
aeroPhase=interp1(cosTheta,aeroPhaseAll,scatterCos)';

platAlt=globalvars.platAlt;
targAlt=globalvars.targAlt;
beamLength=globalvars.beamLength;

if platAlt > targAlt
    look='down';
else
    look='up';
end

%       lat, lon and altitude of platform
%       Get altitudes of center of segments of the FOV
segHt=abs(platAlt-targAlt)/segnum; %height of each segment (m)
% Determine the altitudes of the segments
if platAlt > targAlt
    beamAlts=targAlt+segHt/2:segHt:platAlt-segHt/2;
else
    beamAlts=platAlt+segHt/2:segHt:targAlt-segHt/2;
end

%       Determine the Phase and Scattering function for the segments
aeroPhaseFcn=interp1(outputs.Atmosphere.altVector,aeroPhase,beamAlts);
aeroScaFcn=interp1(outputs.Atmosphere.altVector,aeroSca,beamAlts)./1000
; %change to per m
molScaFcn=interp1(outputs.Atmosphere.altVector,molSca,beamAlts)./1000;
%change to per m

%       Determine Extinction (m^-1) at the segment centers
Extinction=interp1(outputs.Atmosphere.altVector,outputs.Atmosphere.tota
lExt,beamAlts)./1000; %change to per m
%
segLength=beamLength/segnum; %Length of segments

% distances from platform to each of the beam segment centers
if strcmp(look,'down')==1;
    pathLength=beamLength-segLength/2:-segLength:segLength/2;
else
    pathLength=segLength/2:segLength:beamLength-segLength/2;
```

```matlab
end

% pathLength=beamLength-segLength/2:-segLength:segLength/2;



pathLength=pathLength+segOne;  % add small distance to prevent 1/R^2
'blow up'
Extseg=Extinction.*segLength; % optical depth for each segment in
increasing altitude
% for platform at altitude looking down

% Calculate optical depth for each segment center to platform
if strcmp(look,'down')==1;
    Extd(segnum)=Extseg(segnum); %first extinction is just the first
optical depth
    for k=segnum-1:-1:1
        Extd(k)=Extd(k+1)+Extseg(k);
    end
else
    Extd(1)=Extseg(1); %first extinction is just the first optical
depth
    for k=2:1:segnum
        Extd(k)=Extd(k-1)+Extseg(k);
    end
end
pathTrans=exp(-Extd); %Transmission to each segment center



%Calculate incident Irradiance at each segment center (W/m^2)
for i=1:length(beamAlts)
    incIrr(i)=SolarIrr(beamAlts(i),zenithAngle,lambda,bandWidth);
end

% Create diameters for beam using user defined spot size at target
    size1=0;
    size2=delta/fl*beamLength;
if strcmp(look,'down')==1;
    diameter=linspace(size2,size1,segnum+1); %segnum+1 equally spaced
diameters
else
    diameter=linspace(size1,size2,segnum+1); %segnum+1 equally spaced
diameters
end
    diameter=(diameter(1:end-1)+diameter(2:end))./2; %diameters at
center of segments
    area=diameter.^2; % (m^2)

% % Calculate the scattering volume elements
dv=segLength.*area;
% Scattered Irradiance (w*m^-2)
aeroBScaIrrFromSeg=(aeroPhaseFcn.*aeroScaFcn.*incIrr.*pathTrans.*dv)./(
4.*pi.*pathLength.^2);
molBScaIrrFromSeg=(molPhaseFcn.*molScaFcn.*incIrr.*pathTrans.*dv)./(4.*
pi.*pathLength.^2);
```

```matlab
TotalBScaIrrFromSeg=aeroBScaIrrFromSeg+molBScaIrrFromSeg;
aeroBScaIrr=sum(aeroBScaIrrFromSeg);
molBScaIrr=sum(molBScaIrrFromSeg);
TotalsolarBScaIrr=sum(TotalBScaIrrFromSeg);



function [ IncSolarIrr,atmTrans ] =
SolarIrr(locAlt,zenithAngle,lambda,bandWidth)
%SOLARTRANS Calculates the solar irradiance given the altitude, solar
% zenith angle, wavelength of sensor, and bandwidth of the sensor

global transoutputs
clear segnum R

% Constants
segnum=1000;
sunAlt=100000; %outside 100 km there is no atmospheric attenuation
Re=6378100; %radius of earth in meters
Specpts=10; %spectral bw pts to integrate over

% for i=1:1:90;
% zenithAngle=i;
zenithAngle=zenithAngle.*pi./180;

% Use law of sines to compute distance from sun to observer
theta=pi-zenithAngle;
SE=sunAlt+Re; %center of Earth to sun
OE=locAlt+Re; %center of Earth to observer
C=asin(OE*sin(theta)/SE); %Earth-Sun-Observer Angle
A=pi-C-theta; %Center of Earth Angle
R=sin(A)*SE/sin(theta); %total distance sun to observer

segLength=R./segnum;
%pathlength sun to center of segments in increasing altitude
pathLength=R-segLength/2:-segLength:segLength/2;
% Use law of cosines to find altitudes at center of segments
pathAlts=sqrt(SE.^2+pathLength.^2-2.*SE.*pathLength.*cos(C))-Re;

Extinction=interp1(transoutputs.Atmosphere.altVector,transoutputs.Atmos
phere.totalExt,pathAlts)./1000; %change to per m
OptDepthSeg=Extinction.*segLength;
transSeg=exp(-Extinction.*segLength);
atmTrans=exp(-sum(Extinction.*segLength));

%load the solar spectrum (wavelength,spectral Irradiance)
solarSpec=load('SolarSpectra.txt');
solarSpecLambda=solarSpec(:,1).*1e-6; %wavelength in meters
solarSpecIrr=solarSpec(:,2).*1e6; %change to per m wavelength
% Integrate over the bandwidth to get Irradiance
bandWidthpts=linspace(lambda-bandWidth/2,lambda+bandWidth/2,Specpts);
solarBWIrrpts=interp1(solarSpecLambda,solarSpecIrr,bandWidthpts);
ExtSolarIrr=trapz(bandWidthpts,solarBWIrrpts); %(Wm^-2)
IncSolarIrr=ExtSolarIrr*atmTrans; %Incident SolarIrr (Wm^-2)
end
```

Bibliography

ASTM. 2000. http://rredc.nrel.gov/solar/spectra/am0/. (accessed November 2011).

Beardmore, Keith. *Implementation of Light-Tunneling within WaveTrain.* MZA Associates Corporation, unpublished, 2006.

Brown, Scott D., Daniel D. Blevins, and John R. Schott. "Time-gated topographic LIDAR scene simulation." *SPIE vol. 5791*, 2005.

Fiorino, S.T., et al. "Broad Spectrum Optical Turbulence Assessments form Climatological Temperature, Pressure, Humidity, and Wind"." *Journal of Directed Energy*, 2010: 223-238.

Fiorino, Steven T., et al. "Field and Laboratory Validation of Surface Layer Optical Turbulence and Off-Axis Irradiance." *SPIE*, 2010: Vol. 7685 76850E-1.

Fiorino, Steven T., et al. "Worldwide assessments of laser radar tactical scenario performance variability for diverse low altitude atmospheric conditions at 1.0642 um and 1.557 um." *Journal of Applied Remote Sensing, Vol. 3*, 2009.

Fiorino, Steven T., et al. "Worldwide uncertainty assessments of ladar and radar signal-to-noise ratio performance for diverse low altitude atmospheric environments." *Journal of Applied Remote Sensing, Vol 7685*, 2010.

Fiorino, Steven T., Richard J. Bartell, Matthew J. Krizo, Kenneth P. Moore, and Salvatore J. Cusumano. "Validation of a Worldwide Physics-Based, High Spectral Resolution Atmospheric Characterization and Propagation Package for UV to RF Wavelengths." *SPIE Vol. 7090*, 2008.

Fiorino, Steven T., Robb M. Randall, Richard J. Bartell, John D. Haiducek, Mark F. Spencer, and Salvatore J. Cusumano. "Field Measurements and Comparisons to Simulations of High Energy Laser Propagation and Off-Axis Scatter." *SPIE*, 2010: Vol. 7814 78140P-1.

Fujii, Takashi, and Tetsuo Fukuchi. *Laser Remote Sensing.* Boca Raton: Taylor and Francis Group, 2005.

Grasso, Robert J., George F. Dippel, and Leonard E. Russo. "A Model and Simulation to Predict 3D Imaging LADAR Sensor Systems Performance in "Real World" Type Environments." *SPIE Vol. 6303*, 2006.

"Help for PLEXUS." Air Force Research Laboratory VSBYB, February 2006.

Jelalian, Albert V. *Laser Radar Systems.* Boston: Artech House, 1992.

Kenyon, Henry S. "Ladar Illuminates Optical Sensors." *Signal Magazine*, 2002.

Kneizys, F. X., Shettle, E. P., et al. *Atmospheric Transmittance/Radiance: Computer Code.* Hanscom AFB: Air Force Geophysics Laboratory AFGL-TR-83-0187, 1983.

"LEEDR User Guide Version 3.0 ." Wright Patterson AFB, Ohio: Air Force Institude of Technology, ENP, Center for Directed Energy.

Mazuk, S., and D. K. Lynch. *Comparison of MODTRAN and FASCODE for Selection of a Cirrus Cloud Detection Band Near the 1.38-um Water Absorption Window.* Contract No. F04701-00-C0009, Los Angeles: Space and Missile Systems Center, 2001.

O'Brien, Michael E., and Daniel G. Fouche. "Simulation of 3D Laser Radar Systems." *Lincoln Laboratory Journal, Volume 15*, 2005.

Osche, Gregory R., and Donald S. Young. "Imaging Laser Radar in the Near and Far Infrared." *IEEE Vol. 84*, 1996: 103-125.

Perram, Glen P., Salvatore J. Cusumano, Robert L. Hengehold, and Steven T. Fiorino. *An Introduction to Laser Weapon Systems.* Directed Energy Professional Society, 2010.

Petty, Grant W. *A First Course in Atmospheric Radiation.* Madison: Sundog Publishing, 2006.

Richmond, Richard D., and Stephen C. Cain. *Direct-Detection LADAR System.* Bellingham: Society of Photo-Optical Instrumentation Engineers, 2010.

Ritter, R. J., A. C. Birenboim, and W. A. Andrews. *High-Energy Laser System End-to-End Model User's Manual.* Kirtland AFB: Air Force Research Laboratory Directed Energy Directorate, 2009.

Smith, H.H.P., D.J. Dube, M.E. Gardner, S.A. Clough, F.X. Kneizys, and L.S. Rothman. *FASCODE-Fast Atmospheric Signature Code (Spectral Transmittance and Radiance).* Visidyne, Inc, Hanscom AFB: Air Force Geophysics Laboratory Scientific Report No. 2 AFGL-TR-78-0081, 1978.

Snell, H. E., J.-L. Moncet, G.P. Anderson, J.H. Chetwynd, and J. Wang. "FASCODE for the Environment (FASE)." *Atmospheric Propagation and Remote Sensing IV converence.* Orlando: SPIE 2471, 1995. 88-95.

Snell, H.E., W.O. Gallery, D.B. Hogan, and J.-L. Moncet. "Fast Atmospheric Signature Code for the Environment (FASE)." *Proceedings of the Sixth Atmospheric Radiation Measurement (ARM) Team Meeting.* San Antonio, 1996.

Snell, H.E., W.O., Moncet, J.L. Gallery, and C.P. Sarkisian. *FASCODE For The Environment.* Atmospheric and Environmental Research, Inc., Hanscom Air

Force Base: Air Force Research Laboratory Space Vehicles Directorate Scientific Report No. 3 AFRL-VS-TR-2001-1603, 2000.

Telgarsky, Rastislav, Michael C. Cates, Carolyn Thompson, and John N. Sanders-Reed. "High Fidelity Ladar Simulation." *SPIE Vol. 5412*, 2004.

Wallace, John, M., and Peter V. Hobbs. *Atmospheric Science An Introductory Survey.* Amsterdam: Elsevier Inc., 2006.

<table>
<tr><td colspan="2">REPORT DOCUMENTATION PAGE</td><td colspan="2">Form Approved
OMB No. 074-0188</td></tr>
</table>

REPORT DOCUMENTATION PAGE

1. REPORT DATE *(DD-MM-YYYY)* 22/03/2012	2. REPORT TYPE Master's Thesis	3. DATES COVERED *(From – To)* March 2011 – March 2012

TITLE AND SUBTITLE LADAR Performance Simulations with a High Spectral Resolution Atmospheric Transmittance and Radiance Model- LEEDR	5a. CONTRACT NUMBER
	5b. GRANT NUMBER
	5c. PROGRAM ELEMENT NUMBER
6. AUTHOR(S) Roth, Benjamin D., Captain, USAF	5d. PROJECT NUMBER
	5e. TASK NUMBER
	5f. WORK UNIT NUMBER

7. PERFORMING ORGANIZATION NAMES(S) AND ADDRESS(S)
    Air Force Institute of Technology
    Graduate School of Engineering and Management (AFIT/EN)
    2950 Hobson Way, Building 640
    WPAFB OH 45433-7765
	8. PERFORMING ORGANIZATION REPORT NUMBER
	
	    AFIT/APPLPHY/ENP/12-M09

9. SPONSORING/MONITORING AGENCY NAME(S) AND ADDRESS(ES) Matthew P. Dierking, Technical Advisor 3109 P Street Wright Patterson AFB, OH 45433 DSN: 798-4396	10. SPONSOR/MONITOR'S AFRL/RYMM
	11. SPONSOR/MONITOR'S REPORT NUMBER(S)

12. DISTRIBUTION/AVAILABILITY STATEMENT
   APPROVED FOR PUBLIC RELEASE; DISTRIBUTION UNLIMITED.

13. SUPPLEMENTARY NOTES

14. ABSTRACT
In this study of atmospheric effects on Geiger Mode laser ranging and detection (LADAR), the parameter space is explored primarily using the Air Force Institute of Technology Center for Directed Energy's (AFIT/CDE) Laser Environmental Effects Definition and Reference (LEEDR) code. The LADAR system is assessed at operationally representative wavelengths of 1.064, 1.56 and 2.039 µm with several up and down looking engagement geometries at locations worldwide. Results computed with LEEDR are compared to standard atmosphere and Fast Atmospheric Signature Code (FASCODE) assessments. Results show significant climate dependence, but large variances between climatological and standard atmosphere assessments. An overall average absolute mean difference ratio of 1.03 is found when climatological signal to noise ratios at forty locations are compared to their equivalent standard atmosphere assessment. Atmospheric transmission is shown to not always correlate with signal to noise ratios between different atmosphere profiles. Allowing aerosols to swell with relative humidity proves to be significant especially for up looking geometries reducing the signal to noise ratio several orders of magnitude. Turbulence blurring shows that the up looking LADAR system has little capability at a 50km range yet has little impact at a 3km range.

15. SUBJECT TERMS
LADAR, LIDAR, LEEDR, laser radar simulation, Atmospheric Effects, Atmospheric Propagation

16. SECURITY CLASSIFICATION OF:			17. LIMITATION OF ABSTRACT	18. NUMBER OF PAGES	19a. NAME OF RESPONSIBLE PERSON Steven T. Fiorino, AFIT/ENP
a. REPORT	b. ABSTRACT	c. THIS PAGE	UU	119	19b. TELEPHONE NUMBER *(Include area code)* (937) 255-3636, ext 4506 (Steven.Fiorino@afit.edu)
U	U	U			